INAUGURAL DISSERTATION

zur Erlangung der Doktorwürde

vorgelegt an der Naturwissenschaftlichen
Fakultät für Chemie und
Geowissenschaften

der Ruprecht-Karls-Universität in Heidelberg

von
M.Sc. Can Yildirim
aus Istanbul

Tag der mündlichen Prüfung: 03. Februar 2017

Modification of Aromatic Self-Assembled Monolayers by Electron Irradiation

Gutachter:

Prof. (apl.) Dr. Michael Zharnikov

Prof. (apl.) Dr. Hans-Robert Volpp

To my lovely wife and son

Zusammenfassung

Der Effekt von Elektronenbestrahlung an selbstorganisierende Monolagen (SAMs) von aromatischen Thiolen mit stabförmigen oligophenyl, acene und oligo(phenylen ethinylen) (OPE) Rückgrat, bestehend aus einem bis drei Phenyl Ringen, wurde mit einem besonderen Fokus auf die Entwicklung von strahleninduzierten Prozessen und die Eigenschaften von diesen Filmen als Negativresist in Elektronenlitographie untersucht. Bereits in einem frühen Stadium der Bestrahlung, zeigten alle untersuchten Filme ein ähnliches Verhalten mit einer klaren Dominanz von Quervernetzung. Die Wirkungsquerschnitte für die Modifikation der SAM Matrix und der Beschädigung der SAM-Substrat Grenzfläche wurden mittels einer Primärelektronenenergie von 50 eV bestimmt, welche häufig für die Herstellung von Kohlenstoff-Nanomembranen (KNMs) verwendet wird. Die ermittelten Werte sind ähnlich in innerhalb eines Prozesses und unterscheiden sich nur geringfügig für die verschiedenen Rückgraten. Die zwei-Ring Systeme zeigten mit einer optimalen Dosis von 10-20 mC/cm² bei 0.5-1 keV die beste Eignung als lithographischer Resist. Die Leistung der ein-Ring und drei-Ring Systeme wurde durch die geringere Anzahl an Quervernetzungen und den hohen Widerstand der Ausgangsschichten gegen die Ätzlösungen beeinträchtigt. Ein weiterer Prozess, welcher mit auf die schlechte lithographische Leistung der drei-Ring Systeme zurückgeführt werden kann, aber auch bei den zwei-Ring Systemen bei einer hohen Dosis auftrat, war das spontane Ablösen der quervernetzen SAMs innerhalb der bestrahlten Flächen in Form von KNMs. Aus den lithographischen Daten wurden der Wirkungsquerschnitt und die strahleninduzierte Quervernetzung ermittelt und in Zusammenhang mit Rückstreuung und Sekundärelektronenausbeute diskutiert. Für die drei-Ring Systeme wurde zum ersten Mal die Herstellung von KNMs aus SAMs mit OPE Rückgrat gezeigt.

Zusätzlich zu den oben genannten Experimenten wurden die elektrischen Transporteigenschaften von den hergestellten SAMs nach Elektronenbestrahlung (50 eV) untersucht. Die Two-Terminal Junction Methode wurde dafür verwendet. Die erhaltenen Werte für die Stromdichte korrelieren sehr gut mit der molekularen Länge und bestätigen die generelle Formel $J = J_0 \exp(-\beta d)$, welche die Leitfähigkeit in monomolekularen Schichten beschreibt. Die J_0 Werte nahmen leicht ab und wurden spannungsabhängig nach Bestrahlung, was vermutlich mit der Tunnelbarriere an der

SAM-Substrat Grenzfläche zusammenhängt. Zusätzlich zeigten alle Filme einen exponentiellen Abfall der Leitfähigkeit mit zunehmender Bestrahlungsdosis, was hauptsächlich auf den beobachteten Anstieg des Kontaktwiderstandes zurückzuführen war. Dieses Verhalten ist (i) der Modifikation der elektronischen Struktur, (ii) der Änderung der Austrittsarbeit, (iii) der Adsorption von Sauerstoff oder durch die Luft übertragenen Partikeln nach Bestrahlung und (iv) den teilweisen Brüchen von Au-S Bindungen an der SAM-Substrat Grenzfläche zuzuschreiben. Um Informationen über das Verhalten der relevanten Parameter zu bekommen, wurden Änderungen in der elektronischen Struktur und der Austrittsarbeit der SAMs nach Bestrahlung mit einer Kelvin Sonde untersucht. Der beobachtete Anstieg der Austrittsarbeit (zwischen 0.1 und 0.26 eV) korrelierte gut mit dem Kontaktwiderstand. Die elektronische Struktur wurde indirekt mittels Fowler-Nordheim Graphen ermittelt. Diese Graphen zeigten nicht-resonantes (direktes) Tunneln für alle SAMs und einen Übergang in den Feldemissionsbereich für drei-Ring und OPE2 Monoschichten. Die jeweilige Übergangsspannung (V_{trans}) wurde ermittelt, welche ein Fingerabdruck für die Position der Grenzorbitale darstellt. Die Werte für V_{trans} verringerten sich nach Bestrahlung und zeigten eine fortschreitende Verringerung des HOMO-LUMO Abstands.

Neben den nicht-substituierten aromatischen SAMs, wurden ebenfalls einfache strahleninduzierte Prozesse an Pyridin-substituierten Monoschichten untersucht. Die Reaktion dieser Filme auf Bestrahlung war vergleichbar mit denen der nicht-substituierter SAMs. Am wichtigsten war, dass der Stickstoffgehalt in den Pyridin-substituierten Filmen nach Elektronenbestrahlung nur leicht abnahm, was die Möglichkeit eröffnet Stickstoff dotierte KNMs und vergleichbare Graphenschichten herzustellen.

Abstract

The effect of electron irradiation on aromatic thiolate SAMs with rod-like oligophenyl, acene, and oligo(phenylene ethylene) (OPE) backbones, containing from one to three phenyl rings, was studied, with a particular emphasis on the evolution of the basic irradiation-induced processes and performance of these films as negative resists in electron lithography. All films studied exhibited similar behavior upon the irradiation, with clear dominance of cross-linking, taking hold of the systems at already very early stages of the treatment. The cross-sections for the modification of the SAM matrix and the damage of the SAM-substrate interface were determined for the primary electron energy of 50 eV, frequently used for the fabrication of carbon nanomembranes (CNM). The derived values were found to be similar for a particular process, showing only slight difference for the different backbones. The two-ring systems exhibited the best performance as lithographic resists, with an optimal dose of 10-20 mC/cm^2 at 0.5-1 keV. The performance of the one-ring and three-ring systems was limited by a poor ability to form an extensive cross-linking network and by high resistivity of the pristine films to the etching agents, respectively. Another process, associated with the poor lithographic performance of the three-ring systems but occurring at high doses for the two-ring systems as well, was a spontaneous release of the cross-linked SAMs within the irradiated areas, in the form of CNMs. From the lithographic data, cross-sections of the irradiation-induced cross-linking were derived and discussed in context of backscattering and secondary electron yield. For the three-ring systems, fabrication of CNMs was demonstrated, first time in the OPE case.

In addition to the above experiments, the electric transport properties of the given SAMs upon electron irradiation (50 eV) were studied. Two-terminal junction method was applied. The obtained current density values correlated well with the molecular length, confirming the general formula $J = J_0 \exp(-\beta d)$ used to describe the conductance of monomolecular films. The β values decreased slightly and became voltage-dependent upon irradiation, presumably because of the tunneling barrier at the SAM-substrate interface. In addition, all films studied exhibited an exponential decrease in conductance with increasing irradiation dose, which was mostly related to the observed increase in the contact resistance defining the J_0 value. This behavior was attributed to (i) the modification of the electronic structure (ii) change of WF, (iii)

adsorption of oxygen or airborne species upon exposure of the irradiated films to ambient, and (iv) partial breakage of Au–S bonds at the SAM-substrate interface. To get information on the behavior of the relevant parameters, changes in the electronic structure and WF of the SAMs upon the irradiation were monitored by the Kelvin probe technique. The observed increase in WF (between 0.1 and 0.26 eV) for the most of the systems correlated well with the increase in the contact resistance. The electronic structure was studied indirectly by compiling the Fowler-Nordheim (F-N) plots. These plots exhibited non-resonant (direct) tunneling for all SAMs and transition to the field emission regime for the three-ring and OPE2 monolayers. The respective transition voltage V_{trans} was derived, which is believed to be a fingerprint for the positions of the frontier molecular orbitals. The V_{trans} values became smaller upon the irradiation, indicating a progressive decrease in the HOMO-LUMO gap.

Apart from the non-substituted aromatic SAMs, basic irradiation-induced processes were studied in pyridine-substituted monolayers as well. Their response to irradiation treatment was similar as for the non-substituted SAMs. Most significantly, the nitrogen content in the pyridine-substituted films was found to decrease only slightly under electron irradiation, which opens a way to the fabrication of nitrogen-doped CNMs and related graphene sheets.

Table of Contents

Acknowledgement

I would like to express my special appreciation to my supervisor Prof. (apl.) Dr. Michael Zharnikov who has been a tremendous mentor for me. I would like to thank him for giving me the possibility to conduct the research in this interesting topic and for his support and advice during the last three years.

Thanks also go to Prof. Dr. Hans-Robert Volpp for agreeing to be my second examiner.

I would also like to thank all my co-workers and officemates, namely Mustafa Sayin, Swen Schuster, Tobias Wächter, André Brink, Jean Thusek, Eric Sauter, Yan Rui and Musammir Khan as well as the technical staff of our institute: Günter Meinusch, Peter Jeschka and Reinhold Jehle.

Thanks go to my brother and sisters, for always supporting me in my decisions and helping me to reach my goals.

Lastly, I would like to thank my parents for always supporting and encouraging me. And most of all, a very special thank goes to my warmhearted, supportive, and patient wife Sevgi whose faithful support during this PhD is invaluable.

Abbreviations

AFM	Atomic force microscopy
AT	Alkanethiol
BE	Binding energy
BSE	Backscattered electron
CNM	Carbon nanomembrane
CPD	Contact potential difference
CRT	Cathode ray tube
EBL	Electron beam lithography
EGaIn	Eutectic Gallium-Indium
F-N	Fowler-Nordheim
FWHM	Full width at half-maximum
HDT	Hexadecanethiol
HOMO	Highest occupied molecular orbital
I-V	Current-voltage
KE	Kinetic energy
KP	Kelvin probe
LUMO	Lowest unoccupied molecular orbital
NEXAFS	Near edge X-ray absorption fine structure spectroscopy
OPE	Oligo(phenylene ethynylene)
PPL	Proximity printing lithography
PVD	Physical vapor deposition
SAM	Self-assembled monolayer

SE	Secondary electron
SEM	Scanning electron microscopy
TEM	Transmission electron microscopy
UHV	Ultra-high vacuum
UV	Ultraviolet
WF	Work function
XPS	X-ray photoelectron spectroscopy

Chemicals

AnthT	2-anthracenethiol
BPT	1,1'biphenyl-4-thiol
BP1n	4-(4-pyridyl)phenyl-1-methanethiol
BPn	4-(4-pyridyl)phenyl-1-thiol
DMF	Dimethylformamide
EtOH	Ethanol
NphT	2-naphthalenethiol
OPE2	S-[4-(2-phenylethynyl)phenyl] thioacetate
OPE3	S-[4-[2-[4-(2-phenylethynyl)phenyl]ethynyl]phenyl] thioacetate
PMMA	Poly(methyl methacrylate)
PT	Benzenethiol
TP1	Terphenyl-4-methanethiol
TP1n	4′ (4-pyridyl)biphenyl-4-methanethiol
TPDMT	Terphenyldimethanethiol
TPT	1,1′,4′,1″-terphenyl-4-thiol

Symbols

e	~1.6×10^{-19} C	Elementary charge
eV	~1.602×10^{-19} J	Electronvolt
h	~6.626×10^{-34} J.s	Planck constant
Φ	eV	Work function
ν	s^{-1}	Frequency
E_b	eV	Binding energy
E_F	eV	Fermi level
E_{kin}	eV	Kinetic energy
λ	nm	Attenuation length
θ	°	Take-off angle of the photoelectrons
d	Å	Thickness
J	A/cm^2	Current density
β	$Å^{-1}$	Tunneling decay constant
R_T	Ω.cm	Tunneling resistance
Q	Coulombs	Cumulative charge delivered to the surface
σ	cm^2	Cross-section
S_{irrad}	cm^2	Area irradiated by the electron beam
I	no unit	Film parameter in a course of irradiation

1 Introduction

Self-assembled monolayers (SAMs) represent an indispensable element of modern nanotechnology due to their ability to tune surface properties such as chemical reactivity, wettability and biocompatibility [1, 2]. Their numerous applications, ranging from chemical sensors over nanofabrication and molecular electronics to biological and medical issues [1, 3, 4], rely mostly on flexibility of their design, allowing a combination of different functional groups within the general architecture of the SAM constituents, comprised of a suitable anchoring (head) group, rod-like spacer and a terminal tail group. Along with the flexibility of the chemical design, additional possibilities are provided by modification of SAMs by physical means such as ultraviolet (UV) light [5-8], X-rays [9, 10] and electron irradiation [11-14]. In the case of electron irradiation, which is the modification tool used in this study, both primary and secondary electrons originating from the substrate lead to the changes in the hydrocarbon matrix and at SAM-substrate interface. The most prominent irradiation-induced processes include damage of the tail groups, cleavage of the chemical bonds in the SAM matrix, desorption of hydrogen and molecular fragments from the monolayer, cross-linking of the monolayer, loss of the conformational and orientational order and damage of the SAM-substrate interface [11, 15-18]. The exact evolution of these processes in the course of irradiation was found to be dependent on specific molecular architecture of the SAM constituents as well as on their packing density and the nature of the substrate [13, 14, 19]. Among these parameters, the identity of the molecular backbone has the largest influence on the basic outcome of the irradiation treatment [12, 15]. Depending on this parameter, the character of modification is different: with a dominance of either damage or cross-linking scenario. In the case of aliphatic SAMs, dominant irradiation-induced processes are decomposition of the alkyl chains with subsequent desorption of the released fragments and damage of the SAM-ambience interface, due to the breakage of Au−S bonds [11, 17, 20, 21].

Consequently, aliphatic monolayers become mostly damaged upon electron irradiation. In contrast, the reaction of aromatic SAMs to this treatment is dominated by extensive cross-linking, following the cleavage of C–H bonds in the SAM matrix [12, 19]. This has been investigated in detail by a variety of experimental techniques including energy loss spectroscopy [22-24], near edge X-ray absorption fine structure (NEXAFS) spectroscopy [25-27], UV photoelectron spectroscopy [16], infrared absorption spectroscopy [2, 12] and mass spectrometry [16, 24]. Accordingly, aromatic SAMs can potentially serve as a negative resist for lithography [12] and, after the separation from the substrate, exist as carbon nanomembranes (CNMs) [28-36] which can also be transformed into graphene sheets by subsequent pyrolysis [30, 34, 35].

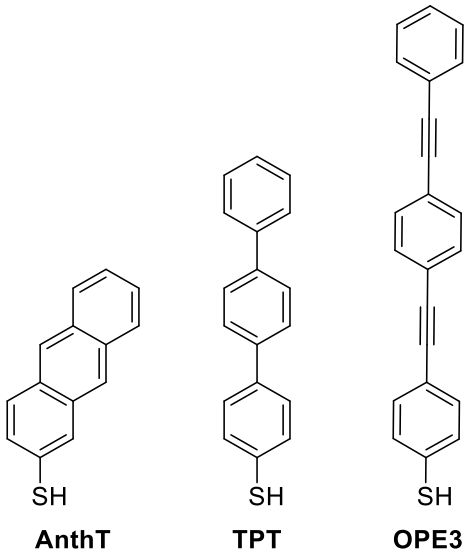

Figure 1.1: A schematic drawing of representative aromatic molecules with acene, oligophenyl and oligo(phenylene ethynylene) backbones, along with their acronyms.

So far, most of the experiments related to lithography and CNM fabrication were performed with biphenyl-based SAMs [37]. However, as was shown recently, CNMs and the derived graphene sheets can also be prepared from different aromatic precursors [35, 36, 38]. This was demonstrated for a variety of molecules, including those with oligophenyl and acene backbones of variable length. The emphasis of these studies was, however, put on the properties of the resulting CNMs, including their structural [35], mechanical [36] and electric transport [38] characteristics, while the exact behavior of the different CNM precursors under electron irradiation was only partly addressed. In this context, in the given PhD work, I performed detailed spectroscopic characterization of the changes occurring in the SAMs with oligophenyl (non-fused) and acene (fused) backbones (see Figure 1.1) under electron irradiation. In addition, to test a broader

variety of rod-like aromatic SAM precursors, I also studied a series of SAMs with oligo(phenylene ethynylene) (OPE) backbone of variable length (see Figure 1.1). Further, in addition to the spectroscopic experiments, which give only indirect information about irradiation-induced cross-linking, dedicated lithographic experiments were performed to monitor the cross-linking behavior and to test the suitability of the SAMs studied as negative resist for lithography. Finally, fabrication of CNMs was tried and demonstrated, which was of particular importance in the case of the OPE-based SAMs that had not been utilized so far for this purpose.

Along with the aforementioned changes at the substrate-SAM interface and in the SAM matrix, a change in electric transport properties of aromatic SAMs is expected to take place upon electron irradiation [38]. Consequently, in addition to the spectroscopic and lithographic experiments, I analyzed the effect of electron irradiation on electric transport properties of the aromatic SAMs, focusing on their static conductance. Note that the charge transport properties of pristine aromatic SAMs have already been extensively studied by using different experimental tools such as molecular junctions based on mercury drop [39-42], eutectic Gallium-Indium (EGaIn) junctions [38, 43], scanning probe methods [44-46], and large area junctions [47]. These experiments provided reliable data about the static conductance of SAMs and revealed specific dependence of the conductance on the molecular length and a parameter β, generally referred to as the attenuation factor. The related formula is given as $J = J_0 \exp(-\beta d)$ and this kind of dependency is characteristic of tunneling or hopping conduction mechanisms, which are typical of insulators and differ distinctly from the Ohmic behavior of conducting materials. The β value, which mostly depends on the character of the molecular backbone, is then a key parameter describing the charge transport efficiency. Low β values indicate high conductance. While the SAMs prepared with saturated molecules (e.g. alkanethiols) have comparably high β values (0.6-1 $Å^{-1}$) [40, 48-50], those of non-saturated molecules have lower β values such as 0.27 $Å^{-1}$ for alkenes [51], 0.27-0.3 $Å^{-1}$ for OPE [42, 51], 0.42-0.7 $Å^{-1}$ for oligophenyl [42, 52-55] and ~0.5 $Å^{-1}$ for acenes [46, 56]. Recently these studies have been extended to address the effect of electron irradiation [38]. Within the respective study, electric transport properties of CNMs prepared from the aromatic SAMs with oligophenyl backbone of variable length were investigated and compared with those of the pristine films. It was shown that electron irradiation leads to a significant (by an order of magnitude) decrease in the electrical conductance of aromatic SAMs which was explained by

decoupling of CNMs from the substrate and partial loss of aromaticity [38]. However, it has not been studied how the electric transport properties change in the course of electron irradiation treatment. In order to monitor this behavior, I analyzed in detail the changes in electrical conductance by exposing a variety of aromatic SAMs to electron irradiation with varying dose and monitoring the relevant parameters. The static conductance of all samples was measured by forming two-terminal EGaIn-SAM-substrate junctions.

Apart from the above studies, I performed dedicated experiments to monitor the changes in the work function (WF) of the aromatic SAMs upon electron irradiation. Generally, SAMs are capable of altering WF of surfaces and interfaces [57-61], however, the respective interface engineering involved only pristine films so far and the effect of electron irradiation on the WF of SAMs has not been investigated. In my case, the respective data appeared to be useful in context of electric transport properties of the SAMs and, in addition, they can be of practical relevance to useful to tune the WF of metal electrodes in organic electronics.

In addition to the pure hydrocarbon aromatic systems, I also studied nitrogen-containing ones, viz. a series of SAMs with the pyridine building block, performing detailed spectroscopic characterization of the changes occurring in these films upon electron irradiation. This behavior has not been studied so far, but can be of importance for the fabrication of nitrogen-containing CNMs that can be potentially converted to nitrogen-doped graphene sheets.

A basic information about the SAMs and their electron-induced modification is provided in the next chapter, along with the background information about the characterization techniques used in this thesis. The details of the sample preparation and characterization procedures used in this work are given in Chapter 3. In Chapter 4, the results of the spectroscopic, lithographic and electric transport experiments are provided and discussed in detail. The conclusions of the PhD work are compiled in Chapter 5, and, finally, supplementary data of lithographic experiments are presented in Appendix.

2 Basics and Theoretical Background

2.1 Self-Assembled Monolayers (SAMs)

SAMs are organized molecular assemblies that form spontaneously by adsorption of molecules from gas or solution phase on suitable surfaces [1] and are comprised of a head group, rod-like spacer, and a terminal tail group as shown in Figure 2.1. The head group mediates the anchoring to the surface and should be suitable for the substrate, in other words, it should have affinity towards the substrate. For example, the most common head groups are thiol and selenol, which can form SAMs on noble metals like gold, silver, copper and platinum. The other constituent, spacer group, is the molecular backbone (mostly aliphatic or aromatic chains) which gives and designates the order, structural stability, packing density and electrical properties of the resulting SAM. The terminal tail group, often represented by common functional groups (amino, carboxyl, oligoethyleneglycol, nitrile, azide and so forth), which is exposed to the ambience, determines the surface properties.

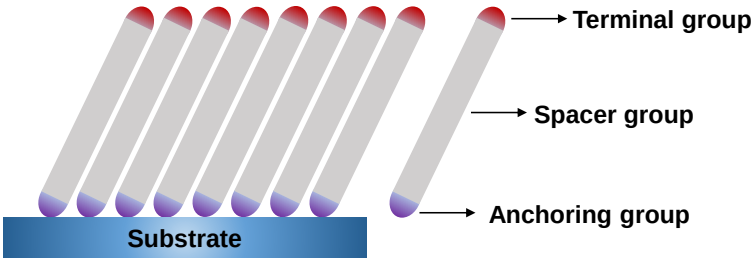

Figure 2.1: Schematic layout of an ordered SAM on a metal substrate. The SAM building blocks are described on the right side.

SAMs can easily be prepared by immersing a clean metal in a dilute solution of suitable molecules. In this context, the most studied SAMs are monolayers of alkanethiols (ATs) on gold substrate binding via thiol head group. They form a c(4x2) superlattice of ($\sqrt{3}$x$\sqrt{3}$) R30° monolayer on Au (111) surfaces [62-64]. ATs are ordered with a distance of 4.97 Å from each other, which corresponds to a packing density of 4.65×10^{14}

molecules per cm^2. The chains are inclined at a tilt angle of ~ 30° with respect to the surface normal [62-65].

For SAM preparation, gold is used as a standard substrate since it can be easily produced by physical vapor deposition (PVD), sputtering and electrodeposition methods [1] and is a quite inert material that does not form an oxide layer in air. Despite the fact that the exact mechanism of the formation of SAMs on gold is not clear, it has been shown by X-ray spectroscopy that the adsorbed sulfur species is a thiolate [66]. One probable mechanism for the chemisorption of alkanethiols on gold forming thiolate (RS-) is given below [67]

$$R - SH + Au_n^0 \rightarrow R - S^- Au^+ + \frac{1}{2} H_2$$

Even though the SAM formation contains a variety of chemical reactions and phases, it can be described in two main steps as follow [1]: In the first step (a few minutes), predominantly the reaction of the substrate with the head group of the molecule (chemisorption) takes place, while in the second step (several hours), formation of an ordered monolayer (crystallization of the surface) takes place because of the van der Waals interactions of the side chains and the mobility of the molecule on the surface.

2.2 Modification of SAMs by Electrons

When SAMs form on a surface, they change the surface properties of the underlying substrate such as wettability, biocompatibility, (non-specific or specific) adsorption (of biomolecules), electronic structure and so forth [1-3]. Along with their ability to modify the properties of the surfaces they are formed on, the SAMs themselves can be modified by irradiating them with electrons [11-14], UV light [5-8] and X-rays [9, 10] as well. Among these modification tools, in electron irradiation both primary and secondary electrons coming from the substrate modify the monolayer by leading to the changes in the hydrocarbon matrix and at the SAM-substrate interface. The character of the modification depends on the identity of the molecules forming the monolayer, most importantly on the molecular backbone. Monolayers consisting aliphatic molecules are damaged under electron irradiation [11, 14, 17, 68]. When aliphatic SAMs are exposed to electron irradiation, their response to the irradiation is degradation of SAM constituents, desorption of aliphatic fragments and weak cross-linking of remaining

aliphatic chains. This damaged film cannot protect the underlying substrate anymore against etchants, therefore, acts as a positive e-beam resist (Figure 2.2).

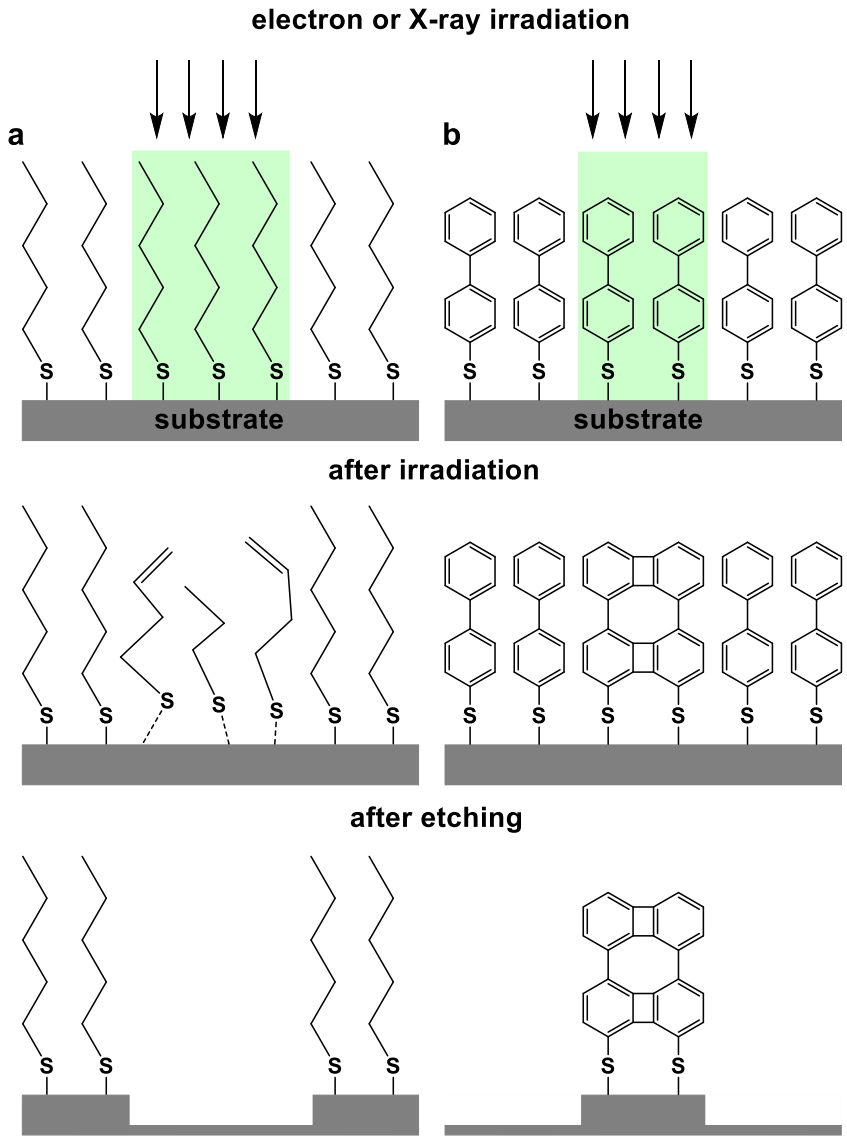

Figure 2.2: Schematic drawing of electron and X-ray lithography with aliphatic (a) and aromatic (b) SAMs as positive and negative resist materials, respectively. Adapted from the ref [69].

In contrast to the aliphatic SAMs, aromatic systems are not damaged but modified by electron irradiation. The adjacent aromatic chains in the SAMs are laterally cross-linked, which reduces the extent of damage to the monolayer such as desorption of the SAM constituents and results in formation of a 2D hydrocarbon film with chemical and mechanical resistance [12, 70]. Note that cross-linking of aromatic SAMs with low-energy electrons (50-100 eV) are generally done by a dose of ~50 mC/cm^2 which roughly equals to 3000 electrons per nm^2 [37]. Accordingly, aromatic SAMs behave as

negative e-beam resist. A representative drawing comparing the behaviors of aliphatic and aromatic SAMs under electron irradiation is shown in Figure 2.2. The simplest and most studied system for lithographic application is based on aromatic SAMs containing biphenyl units [12, 37]. Even though the aromaticity of the monolayer seems to be the only prerequisite for cross-linking, a study [71] based on aliphatic but ring-shaped bicyclohexyl SAM has shown that not the aromaticity, but the ring structure is responsible for cross-linking. In that study, ring-shaped bicyclohexylthiol SAMs have been laterally cross-linked under e-beam irradiation and have acted as a negative resist [71].

In addition, when aromatic SAMs with nitrile [2] or nitro [19, 72] tail groups are treated with electron irradiation, these terminal groups are converted (reduction) to amino group which can be coupled over many chemical reactions, thus, aromatic SAMs can also be used as a template for surface functionalization and related fabrication of nanostructures.

Besides their abilities to be used as negative e-beam resist and to functionalize the surfaces, cross-linked aromatic SAMs form CNMs [28-37] after removing their underlying substrate. The obtained CNMs can further be transformed into graphene-like sheets by annealing the CNMs at elevated temperatures [30, 32, 34, 35].

2.3 Analytical Methods

2.3.1 X-ray photoelectron spectroscopy (XPS)

X-ray photoelectron spectroscopy is a very common technique in surface science to get a quantitative and qualitative understanding of the top most layer (~10 nm) of a surface [73-75]. In this technique, the surface of interest is irradiated with X-rays (photons) with a certain energy which interact with the core electrons of the surface atoms leading to formation of ionized states and emission of photoelectrons [73]. A photoelectron in its simplest form stands for an electron ejected by a photon, which is initially bound to an atom/ion. A representative scheme of the photoelectron emission process is shown in Figure 2.3. The kinetic energy (KE) of the emitted electron is measured by the electron spectrometer (Eq. 2.1), and from the difference between photon energy and the KE of the photoelectron, the binding energy (BE) of the photoelectron can be found [73]. The obtained BEs are the direct indication of the elements on the surface.

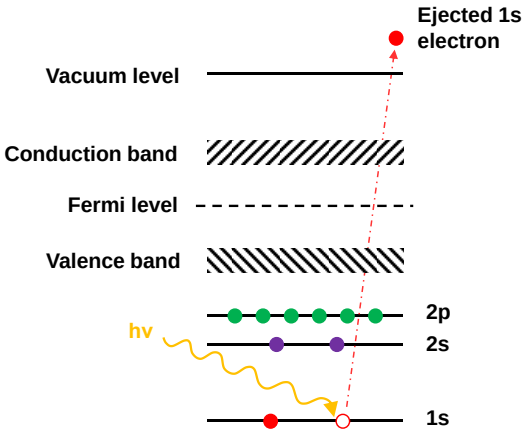

Figure 2.3: Schematic example of the photoelectron emission process and involved energy levels.

A general XPS setup comprises of three major components: an X-ray source, an electron energy analyzer and an ultra-high vacuum (UHV) system. The Figure 2.4 shows a scheme of the experimental setup.

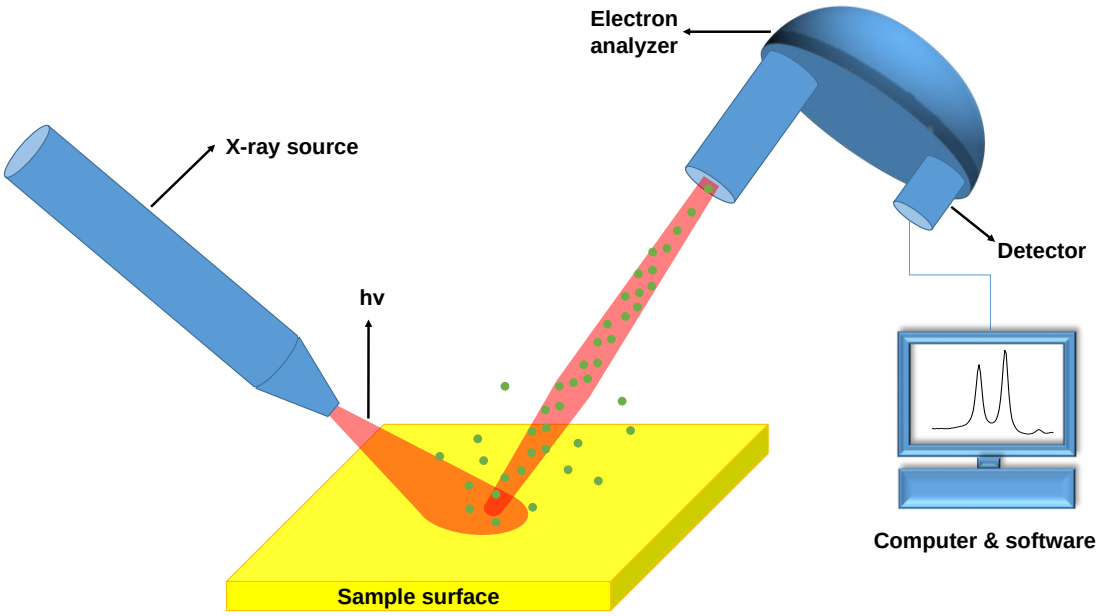

Figure 2.4: Schematic drawing of an XPS setup with basic components. Green filled circles represent photoelectrons. The illustrated process takes place in UHV conditions.

The process for the emission of photoelectrons from sample surface can be explained in three steps [73]: (1) generation of the photoelectrons due to the interaction of X-rays with the electrons in the atomic shell, (2) movement of the photoelectrons through the surface and scattering processes (background formation in the spectrum due to inelastic scattering), and (3) emission of the photoelectrons to the vacuum which overcome the

work function of the sample. Energy of an impinging photon, hv, is transported to a core electron with a binding energy, E_b, leading to the emission of this electron and generation of a vacancy in core electron level (E_b is referenced with the alignment of the Fermi levels of sample and spectrometer). The KE of the emitted photoelectron is independent of the sample work function, Φ_S, but dependent on the analyzer work function, Φ_A (Equation 2.1) and it can be derived from the energy level scheme displayed in Figure 2.5.

$$E_{kin} = h\nu - E_b - \Phi_S - (\Phi_A - \Phi_S) = h\nu - E_b - \Phi_A \tag{2.1}$$

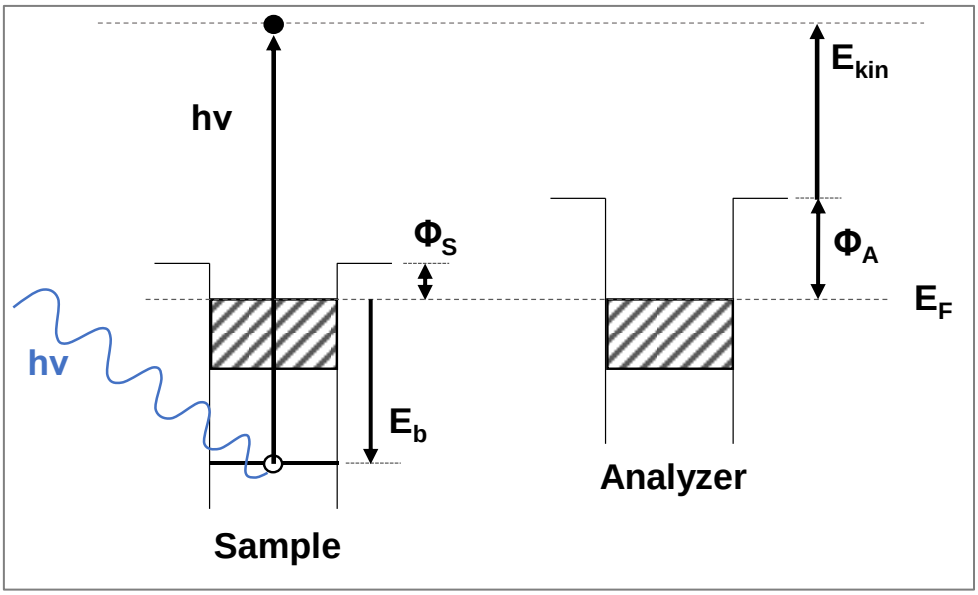

Figure 2.5: Schematic explanation of relevant energy terms in XPS of solid surfaces. An X-ray with energy, hv, generates a vacancy in a core electron level with a binding energy (E_b). The emitted photoelectron has to overcome the work function of the sample, Φ_S, and the energy measured by the analyzer with respect to the Fermi Energy, E_F, is the emitted energy diminished by the difference between the analyzer work function Φ_A and Φ_S. (Adapted from [73]).

Elemental composition: In an obtained XPS spectrum, the signals are formed due to the electrons that come from a few nm depth and have not lost their energy, however, the background formation stems from inelastically scattered electrons. Two types of scans, wide and narrow scans, can be performed in XPS analysis. While wide scans provide a quick qualitative elemental analysis, narrow scans provide more detailed and quantitative information about the specified area.

The quantitative information is directly related to the intensity of the peaks in XPS spectra. For a homogenous sample, the total intensity for an element is the area under the signal and is given by [75]

$$I_{ij} = K \cdot T(KE) \cdot L_{ij}(\gamma) \cdot \sigma_{ij} \cdot n_i \cdot \lambda(KE) \cdot \cos\theta \quad (2.2)$$

I_{ij}: area of peak j from element i

K: instrumental constant

T(KE): transmission function of the analyzer

$L_{ij}(\gamma)$: angular asymmetry factor for orbital j of element i

σ_{ij}: photoionization cross-section of peak j from element i

n_i: concentration of element i

$\lambda(KE)$: attenuation length

θ: take-off angle of the photoelectrons measured with respect to the surface normal

From the equation above (2.2) the element's concentration n_i can be written as

$$n_i = \frac{I_{ij}}{K \cdot T(KE) \cdot L_{ij}(\gamma) \cdot \sigma_{ij} \cdot \lambda(KE) \cdot \cos\theta} = \frac{I_{ij}}{S_i} \quad (2.3)$$

In equation 2.3, S_i is the atomic sensitivity factor. The concentration of an element *a* (c_a) on the surface can be estimated by the following equation

$$c_a = \frac{n_a}{\sum n_i} = \frac{I_a/S_a}{\sum I_i/S_i} \quad (2.4)$$

Attenuation length and film thickness: Attenuation length (λ) is known to be the mean distance of travelled by an electron between two inelastic collisions [75]. The λ of photoelectrons through alkanethiol self-assembled monolayers strongly depends on the KE of electrons [76, 77] which is given by

$$\lambda = (0.3) \cdot KE^{0.64} \quad (2.5)$$

Therefore, the intensity of XPS signals is closely related to the attenuation lengths of electrons. If the top layer, through which electrons coming from underlying substrate pass, is thicker, the electrons will be more attenuated and thus, the intensity of the signal will be lower. This allows to estimate the thickness of the layer on the substrate which could be done in two different ways: (i) attenuation of substrate signal (in our case Au 4f) or (ii) intensity ratio of layer signal to substrate signal (in our case C 1s/Au $4f_{7/2}$).

(i) To obtain the thickness by using the attenuation of substrate signal, either a clean substrate or a sample with a known thickness (e.g. a hexadecanethiol (HDT) SAM on Au) should be used as a reference and the related equation is

$$\frac{I}{I_0} = exp\left(\frac{-d}{\lambda_{sub} \cdot \sin\theta}\right) \tag{2.6}$$

$$d = d_{ref} + \lambda ln\left(\frac{I_{ref}}{I}\right) \tag{2.7}$$

Here d and d_{ref} are the thicknesses of the sample and the reference samples, λ is the attenuation length of the photoelectrons coming from the overlayer, I and I_{ref} are the intensities of the interest and reference samples.

(ii) To calculate the thickness from the intensity ratio of layer signal to substrate signal, a sample with a known thickness should be used as a reference (e.g. a HDT SAM on Au) to determine the spectrometer-specific coefficients and the related equation can be given as

$$\frac{I_{ov}}{I_{sub}} = \frac{1 - exp\frac{-d_{ov}}{\lambda_{ov} \cdot \sin\theta}}{exp\frac{-d_{sub}}{\lambda_{sub} \cdot \sin\theta}} \tag{2.8}$$

where d_{ov} is the overlayer thickness, θ the angle of photoelectron emission and λ_{ov} the attenuation length of the photoelectrons coming from the overlayer and λ_{sub} the attenuation length of the photoelectrons coming from the substrate through the overlayer. For the Eq. 2.8, the thickness of the overlayer is evaluated using a software developed in our research group by Martin Schmid.

2.3.2 Atomic force microscopy (AFM)

Atomic force microscopy is one of the most widely used scanning probe microscopy, which measures the surface properties of the scanned area including topography, friction, magnetic and electric [78-80]. They can be operated at ambient atmosphere, in liquid or under vacuum [78-80], and they are easier to use compared to electron microscopes. In addition, AFM does not require any lens or e-beam irradiation unlike electron microscopes.

The schematic representation of an AFM is like in principle in Figure 2.6. The sample is mounted on a stage which is moved by the piezo elements in x- and y- directions. The maximum scan area of AFM is roughly 100x100 μm^2 with a horizontal resolution of less than 1 nm [80, 81]. The tip is mounted on another piezoelectric element, which

can move only in the z-direction. Generally, x and y piezomaterials are fastened to the sample stage and the AFM tip is fixed to the z piezomaterial, however, there are also some companies, which mount all three piezomaterials (for x,y and z-direction) to the sample stage. This is the case for our AFM setup (NT-MDT Solver NEXT SPM instrument). The deflection of the tip is tracked with a laser, which is reflected at the backside of the tip. The reflected laser is collected by a photodiode, generating a current, and the current values over the scan area is then converted to an image of the respective area.

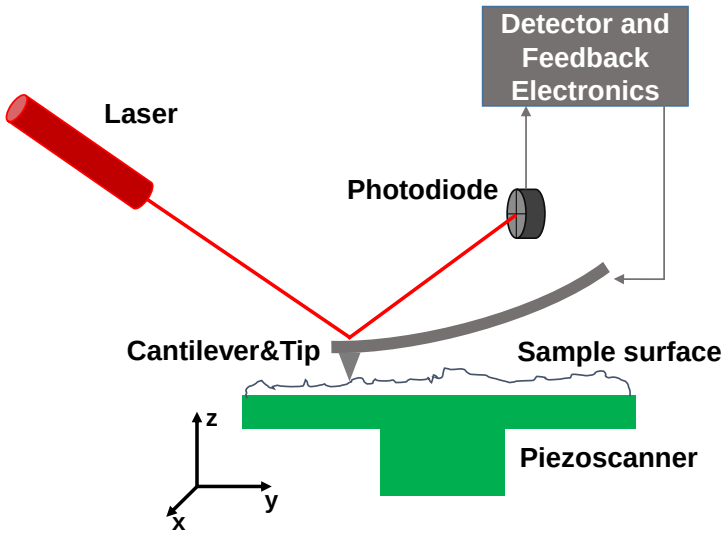

Figure 2.6: Schematic diagram of a general AFM setup: A laser beam is focused on the backside of a cantilever and reflected from it into a four-quadrant photodetector. A sample is mounted on a piezo tube that can move the sample in x, y and z directions.

When the AFM tip approaches to the surface of interest, it behaves as in the force-distance curve given in Figure 2.7. At short distances, because of the overlapping orbitals of the electrons from surface and tip, repulsive forces occur, while at larger distances attractive forces occur because of the van der Waals interaction. The exerted force on the tip can be described by the Lennard-Jones potential (Figure 2.7), thus, leads to cantilever deflection. If the distance is beyond the interaction range, no force acts on the tip and the cantilever is not deflected.

AFM measurements can be operated in static (contact and force spectroscopy) or dynamic (semi-contact and non-contact) mode. In contact mode, the cantilever is swept over the surface of the sample and is deflected because of repulsive forces. In the contact mode, the topography of the sample can be obtained by two ways: constant height mode or constant force mode. While in the constant force mode movement of

the z-piezo gives the topography of the surface under investigation, in the constant height mode deflection of the cantilever is converted to the topography of the surface. This mode is preferably used for hard surfaces and can also be used in liquid environment.

Nevertheless, the contact mode on soft samples like polymers or biomolecules could give damage to the sample. Therefore, a "softer" contact mode was developed, known as semi-contact (tapping mode or intermittent contact), in which the tip is kept at a distance from an attractive regime and the changes in frequency and amplitude are used to measure the force interaction. In tapping mode, the cantilever oscillates up and down near its resonant frequency using a small piezo element in the cantilever holder. Then the tip is approached to the sample until the amplitude has decreased to a predefined value because of the forces (Van der Waals forces, dipole-dipole interactions, electrostatic forces) acting on the cantilever. This amplitude value is sent to the z- piezo element which controls the height of the cantilever above the sample.

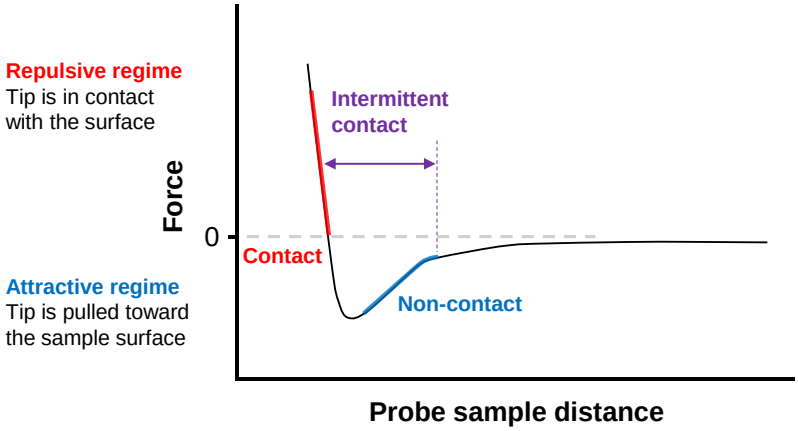

Figure 2.7: Sketch for a force-distance curve of AFM tip and sample. Different operation modes can be used under the effect of described regimes: contact, intermittent contact or non-contact.

The non-contact mode is similar to the tapping-mode, however, the tip is not affected by the sample during oscillation. Instead, the attractive forces of the sample exert a very weak force on the cantilever, resulting in a shift of the resonance frequency and thus amplitude.

2.3.3 Scanning electron microscopy (SEM)

Scanning electron microscopy is an imaging technique in which the surface of interest is analyzed with the electrons emitted from the surface. It can provide an image of the surface with a high magnification up to 300.000 times and a resolution of a few nanometers [81]. A typical SEM consists of an electron gun, magnetic focusing lenses, apertures, a stigmator, deflection coils, a sample stage and detectors [82, 83]. A representative image is shown in Figure 2.8.

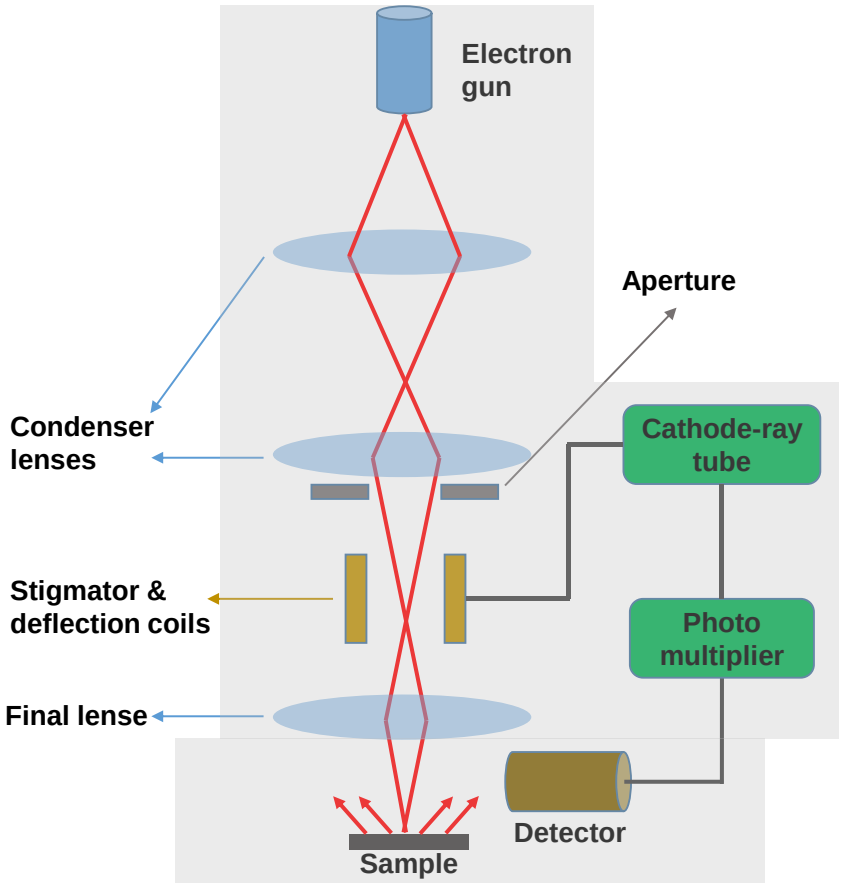

Figure 2.8: Schematic representation of a SEM instrument. The red lines indicate the pathway of electrons emitted by the electron gun.

SEM is a type of electron microscope which scans sample surface with focused e-beam to generate images (under vacuum). Depending on the energy, electrons have a penetration depth from the sample surface towards the interior part where numerous interactions take place due to the transmitted electron and the surface atoms. These interactions mainly lead to formation of secondary electrons as well as forward and backscattered of electrons. Some portion of the emitted electrons can be detected by

appropriate detectors, which are positively biased. The electrons hit the detector and lead to the generation of photons. The photons are sent to photomultiplier and they are converted to a voltage signal. Later, this signal is amplified and projected on the screen of cathode ray tube (CRT). CRT generates intensity profile on a x- and y- direction. This intensity profile is then converted to an image on the screen. Note that the produced images are mainly combination of secondary and backscattered electrons.

The secondary and backscattered electrons differ from each other with their energy and formation mechanism. When a high-energy primary electron is sent to a surface, it interacts with an atom on the surface, and can undergo either inelastic scattering with electrons of the atom or elastic scattering with the atomic nucleus [83]. In an inelastic collision, some of the primary electron energy is transmitted to the atomic electron, leading to emission of a secondary electron. For a secondary electron to reach the surface and exit the solid, it should have enough energy to survive inelastic collisions and overcome the work function of the substrate. Generally, secondary electrons have energies less than 50 eV, and most of the detected secondary electrons are generated in the first few nm of the sample surface [83]. However, backscattered electrons are produced with elastic scattering mechanism. Their energy is comparable to the energy of primary electrons and is considered to be more than 50 eV. As the atomic number increases, the number of backscattered electrons increase because of the bigger atomic radius which increases the elastic scattering of the primary electrons. Therefore, an element with higher atomic number will appear brighter than the element with lower atomic number on a typical SEM image.

SEMs are designed to work with electron energies up to ~ 30 keV, and the electrons are detected with secondary electron (SE), in-lens and backscattered electron (BSE) detectors. Each of them is located at a different position in SEM and therefore, the images of the same sample, depending on the position of the detector, are often quite different. The in-lens detector is vertically above the electromagnetic lens, while the SE detector is positioned at 45° to the sample stage. The secondary electrons experienced one scattering process (SE1: They are coming mostly from upper layer (a few nm) of the surface) are mainly detected with the in-lens detector and give direct information about the surface [82-84]. However, a classical SE detector collects a mixture of SE1, SE and BSEs, which come from deeper layers, therefore, resolution and contrast of an image obtained from SE detector is weaker than in-lens detector.

2.3.4 Electron beam lithography (EBL)

Electron beam lithography (EBL) is one of the most used lithographic techniques for producing high resolution patterns from nm to cm scale, which is derived by a SEM instrument and a special software to draw the desired structures and control the SEM instrument [85]. In this technique, a surface covered with a resist layer (a polymer) is irradiated with an e-beam that leads to either degradation or cross-linking of the resist depending on the nature of the resist. If the resist is *negative,* it will degrade and lead to dissolution of the irradiated area of the resist upon developing (Development of a patterned sample in lithography is to remove the resist either from the patterned area or outside the patterned area, depending on the resist type) (Figure 2.9). However, if it is *positive*, it will cross-link and lead the irradiated area to stay on the surface upon developing while the non-irradiated area will be removed.

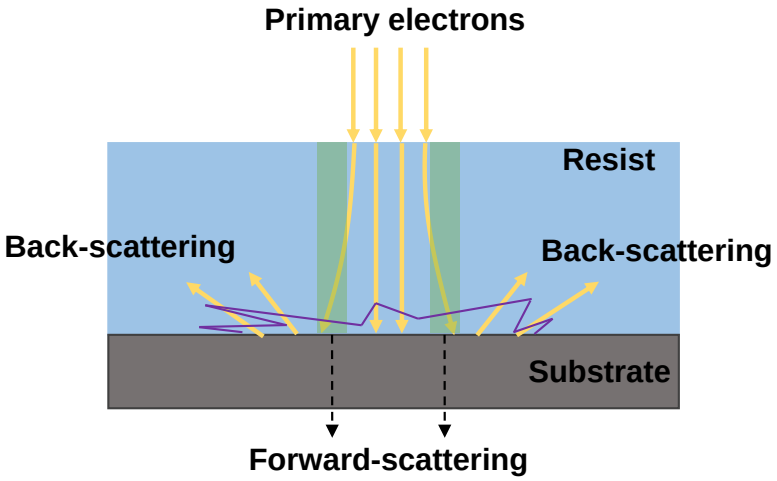

Figure 2.9: Schematic representation of forward-scattering, viz. deflection of the primary electrons in the resist (shown with the green area) and backward-scattering, viz. reflection of some of the primary electrons from the substrate, in EBL. Generated secondary electrons represented by purple solid lines are produced in this process as well.

To obtain a good resolved pattern, electron beam should be optimized by aligning the beam with the smallest possible astigmatism and a small spot size [86]. If the beam is not adjusted well enough, undesired pattern formation is unavoidable. Beside the beam, there are other phenomena like forward and backscattering affecting the pattern shape. In forward scattering, while the electrons travel through the resist, they face some low energy elastic collisions, which deflect the electrons slightly from its path as shown in

the green region (Figure 2.9). Therefore, this process increases the effective beam size, which can be overcome by applying higher electron energy. However, in the backscattering process, as the electrons penetrate the resist and reach the substrate, where some portion of the electrons can experience large angle elastic collisions leading to travel in the resist again. This results in a common phenomenon, *proximity effect*, where both the pattern area (overexposure) and the surrounding environment are also irradiated with the backscattered and secondary electrons. To eliminate this drawback a thinner resist layer can be used.

After adjusting the e-beam and taking such phenomena into consideration, a series of different e-beam doses should be applied to find the optimal dose for the sample to be patterned, because on every substrate the effect of such phenomena (generation of secondary and backscattered electrons) could be different. In addition to this, every resist material could have small chemical differences even if they are called as same polymer, where the necessary dose could be lower or higher for the other resist.

2.3.5 Current-voltage (I-V) measurements with a two-terminal junction

The measurement of current-voltage (I-V) response for SAMs is important to understand their charge transfer properties and it is the most direct and easiest way to probe conduction in SAMs by recording their I-V responses [87]. The I-V characteristics of SAMs are measured by connecting a suitable non-destructive top electrode to the SAMs. The metal substrate on which the SAM is formed serves as the bottom electrode. I-V response of SAMs have been studied by different experimental tools such as molecular junctions based on scanning probe methods [44-46], mercury drop [39-42] and eutectic gallium-indium (EGaIn) tip [38, 43]. With scanning probe methods, very small areas are analyzed, whereas with mercury drop and EGaIn tip bigger areas can be analyzed because of the larger contact area between the top electrode and the SAM.

It has been shown that there are two main conduction mechanisms dominating the electron transfer rates of SAM films: non-resonant (direct) tunneling [38, 44, 45, 88] and hopping [87, 89, 90] (The possible conduction mechanisms [91] for SAMs, adapted from semiconductors, are given in Table 2.1). Non-resonant tunneling is the most common transport mechanism observed in saturated alkyl SAMs [91], which have high energy difference between highest occupied molecular orbital (HOMO) lowest

unoccupied molecular orbital (LUMO) around 8 eV [44] and show an exponential decrease in the tunneling rates with increasing molecular length. This exponential dependence is given by the formula $J = J_0 \exp(-\beta d)$, where β is tunneling decay parameter and d is the molecular length. This parameter is useful to get information about the transport efficiency of SAM films. However, in the case of conjugated species, HOMO-LUMO gaps are smaller, therefore, different transport mechanisms such as resonant tunneling or hopping conduction could take place [44]. Besides, upon increasing bias voltage a transition from direct tunneling to field emission (Fowler-Nordheim tunneling) where the applied bias voltage leads the tunneling barrier to change its shape from rectangular to triangular barrier develops [44, 45]. The transition point, where the conduction mechanism changes, is believed to be fingerprint for the positions of frontier orbitals [92, 93]. While the transition voltage appears at higher voltage range in saturated alkyl SAMs, it appears to be at smaller voltage range in aromatic SAMs [45].

Table 2.1: Possible conduction mechanisms (Adapted from [91]).

Conduction mechanism	**Characteristic behavior**	**Temperature dependence**	**Voltage dependence**
Direct tunneling[1]	$J \sim V exp\left(-\frac{2d}{\hbar}\sqrt{2m\Phi}\right)$	none	$J \sim V$
Fowler-Nordheim tunneling	$J \sim V^2 exp\left(-\frac{4d\sqrt{2m}\Phi^{3/2}}{3q\hbar V}\right)$	none	$\ln\left(\frac{J}{V^2}\right) \sim \frac{1}{V}$
Thermioinic emission	$J \sim T^2 exp\left(-\frac{\Phi - q\sqrt{qV/4\pi\varepsilon d}}{kT}\right)$	$\ln\left(\frac{J}{T^2}\right) \sim \frac{1}{T}$	$\ln(J) \sim V^{1/2}$
Hopping conduction	$J \sim V exp\left(-\frac{\Phi}{kT}\right)$	$\ln\left(\frac{J}{V}\right) \sim \frac{1}{T}$	$J \sim V$

[1] This characteristic of direct tunneling is valid for the low bias regime.

2.3.6 Work function (WF) measurements by Kelvin probe technique

The Kelvin probe (KP) technique is used to measure the work function (WF) of surfaces by bringing probe and the surface in close proximity [94]. The WF is the minimum energy to remove an electron from a solid to the vacuum level (Figure 2.10). It is

derived from the bulk properties of the solid, however, the changes in the surface can considerably alter the WF [95].

In a WF measurement, because the sample and probe are placed in a very close proximity (0.2 to 2 mm) they act as capacitor plates. When the two metal surfaces are connected electrically, electrons flow from the surface with the smaller work function to the surface with the higher work function until the Fermi levels of the capacitor plates are equalized. This results in accumulation of opposite charges on the capacitor plates and a contact potential difference (CPD) [94]. This potential difference generates an electric field between the plates, and can be neutralized by applying an external voltage. The potential difference related to the electric field is equal to the work function difference between the probe and sample [96].

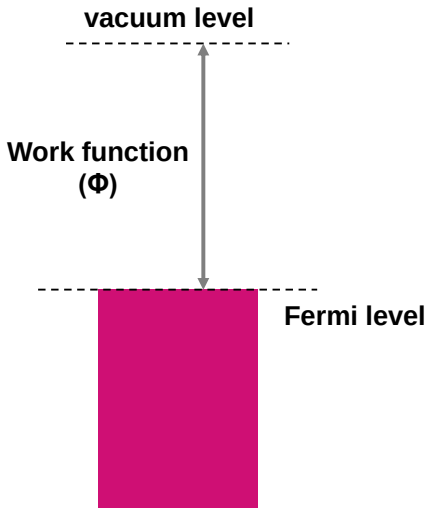

Figure 2.10: Schematic energy diagram of a metal (Adapted from ref [97]).

The basic principles of Kelvin Probe are schematically shown in Figure 2.11. In brief, to measure CPD by using a probe vibrating at a certain frequency, a varying capacitance is produced, and the change in voltage and generated alternative current are recorded (because of varying the distance between the plates) by applying the counter potential and obtaining zero alternative current, the generated electric field is nullified [94, 96]. Since Kelvin Probe technique can measure only CPD values, a calibration is necessary to measure real work function of surfaces. This calibration is generally done with sputtered metals like gold with 5.1-5.3 eV (depending on the crystal structure) work function [98]. This technique is very sensitive to detect the changes in the work function within a few meV resolution [94]. Because the WF is a surface property, small modifications of metal surfaces like doping [99] and SAM formation [58, 61] - even

the direction of the dipole moment in SAMs [100] - can change the work function dramatically.

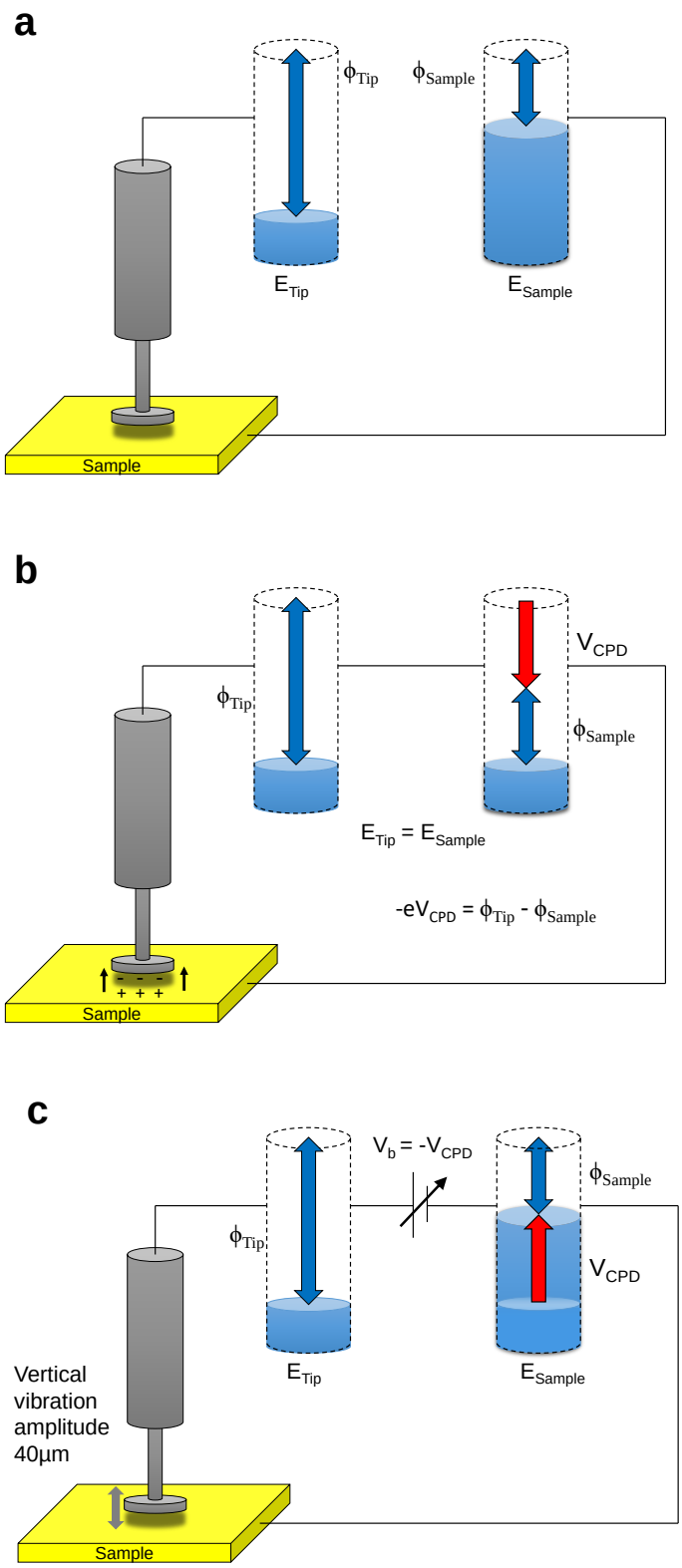

Figure 2.11: Schematic drawing of the basic principles of the WF measurements based on Kelvin Probe (Taken from ref [101]).

3 Experimental

3.1 Materials

All solvents and chemicals were purchased from Sigma-Aldrich. The non-substituted SAM precursors used in this study are shown in Figure 3.1, along with their abbreviations. The precursors benzenethiol (PT); 2-naphthalenethiol (NphT); 1,1'biphenyl-4-thiol (BPT); S-[4-[2-[4-(2-phenylethynyl)phenyl]ethynyl]phenyl] thioacetate (OPE3); and 1,1′,4′,1″-terphenyl-4-thiol (TPT) were commercially obtained from Sigma-Aldrich. The precursors S-[4-(2-phenylethynyl)phenyl] thioacetate (OPE2); and 2-anthracenethiol (AnthT) were custom-synthesized by the group of Prof. Andreas Terfort, Frankfurt University, Germany. The procedure for the synthesis of AnthT can be found in the literature [102]. OPE2 was also synthesized according to a literature protocol [103].

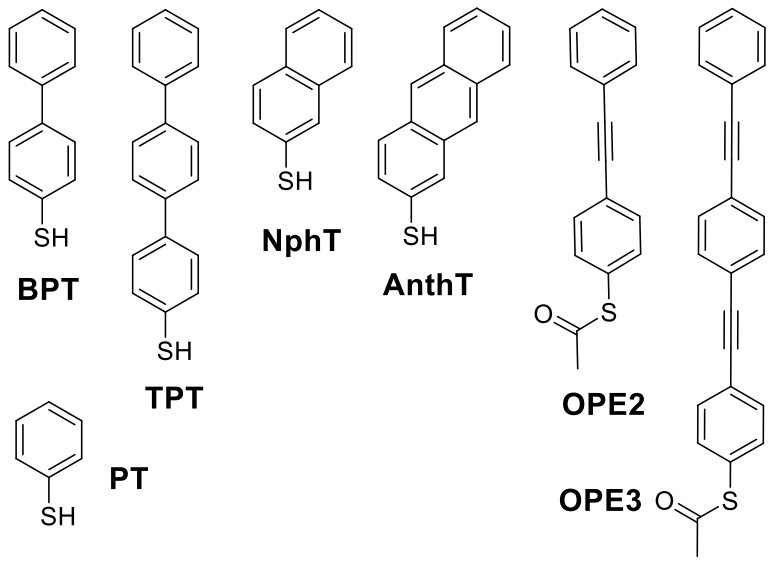

Figure 3.1: The structures of the non-substituted precursors for the SAM studied, along with their abbreviations. The precursors build three different series, with oligophenyl, acene, and OPE backbones, respectively. PT serves as the first member of all three series.

The pyridine-substituted SAM precursors used in this study are shown in Figure 3.2, along with their abbreviations. The precursors 4-(4-pyridyl)phenyl-1-thiol (BPn); 4-(4-

pyridyl)phenyl-1-methanethiol (BP1n); 4′ (4-pyridyl)biphenyl-4-methanethiol (TP1n); and terphenyl-4-methanethiol (TP1) were custom-synthesized by the group of Prof. Andreas Terfort, Frankfurt University, Germany.

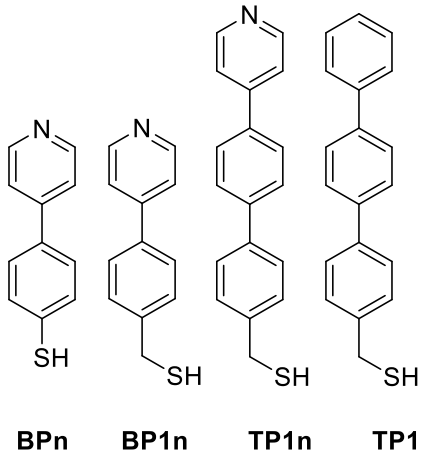

Figure 3.2: The structures of the reference (TP1) and the pyridine-containing precursors (BPn, BP1n and TP1n) for the SAMs studied, along with their abbreviations.

3.2 SAM Preparation

Three types of gold substrates were used (Georg Albert PVD, Germany). For characterization and monitoring of electron irradiation damage, 30 nm polycrystalline gold substrates deposited by physical vapor deposition on polished silicon (100) wafers primed with a 9 nm titanium layer as adhesion promoter were used. Whereas, for lithographic patterns standard Au(111) substrates prepared by evaporation of 75 nm gold onto polished Si(100) wafer (roughness ~10 Å) primed with 5 nm Ti as adhesion layer was used. For the membrane fabrication, Au(111) substrates prepared by evaporation of 75 nm gold directly onto the Si(100) wafer were used. The gold films were polycrystalline, exposing preferably (111) orientated surfaces of individual crystallites.

The substrates having a length of ~1.5 cm and a width of ~1 cm were cleaned by ozonation using a low-pressure Hg lamp for 30 min, rinsed with absolute ethanol (EtOH) and blown dry in a stream of Argon. Gold substrates were immersed in 0.5-1 mM of the respective thiol solutions in absolute EtOH (NphT, AnthT and TP1) or in DMF (PT, BPT, TPT, OPE2, and OPE3) under Argon atmosphere for 24h at room temperature. In the case of acetyl protected thiols, 1-2 drops of aqueous TEA were

added to the thiol solution in order to cleave the acetyl group. Later, the samples were rinsed with the same solvent and EtOH, and dried in an Argon stream.

For the preparation of pyridine-containing SAMs, 50-100 µM ethanolic solutions of the respective molecules were used. After immersing the gold substrates for 24h, they were extensively rinsed with EtOH and dried in an Argon stream. Extensive characterization showed no evidence of impurities or oxidative degradation products for all type of molecules. In addition, reference SAMs of hexadecanethiolate (HDT) were prepared on similar gold substrates using standard procedures [104].

3.3 Electron Irradiation and Patterning

Irradiation of the SAMs was carried out both homogeneously and in a lithographic fashion, depending on the particular purpose. For homogeneous irradiation, a flood gun (FG20, Specs Germany) mounted at a distance of ~11 cm from the sample was used, at a base pressure better than 1×10^{-8} mbar. The electron energy was set to 50 eV, and the dose was calibrated by a Faraday cup and calculated by multiplication of the exposure time by the current density (25 µA/cm^2). For single-dose lithographic patterns, the SAMs were irradiated through a transmission electron microscopy (TEM) grid (Quantifoil, R 1/4, 400 mesh, Copper), which was placed directly onto the SAMs and connected electrically to the sample holder by a metal spring. For multiple-dose irradiation and lithographic patterns, an electron beam writer consisting of a scanning electron microscope (LEO 1530) and a special lithographic unit (Raith Elphy Quantum) was operated. The energy of the electron beam was set to values from 0.5 to 5 keV, and the dose was calibrated by a Faraday cup placed on the same holder as the SAM samples. Within the software, dwell time and area step size of the focused electron beam was set manually to avoid an overexposure at low or an underexposure at high doses, respectively, in order to control irradiation over a large dose scale.

3.4 XPS Characterization

Both pristine and homogeneously irradiated SAMs were characterized by XPS. The XPS characterization was performed out in situ, immediately after irradiation and without exposure of the irradiated films to ambient conditions. The XPS measurements

were carried out under UHV conditions (residual pressure less than 5×10^{-9} mbar) with a MAX200 (Leybold-Heraeus) spectrometer equipped with a Mg Kα X-ray source (200 W) and a hemispherical analyzer. Normal emission geometry was used. The recorded spectra were corrected for the spectrometer transmission and the BE scale was referenced to the Au $4f_{7/2}$ emission at 84.0 eV [105]. A photograph of the used UHV setup including XPS and electron gun is shown in Figure 3.3.

The spectra were fitted by symmetric Voigt functions and a Shirley-type background. To fit the S $2p_{3/2,1/2}$ doublets, two peaks with the same full width at half-maximum (FWHM), the standard [105] spin-orbit splitting of ~1.2 eV (verified by fit), and a branching ratio of 2 (S $2p_{3/2}$/S $2p_{1/2}$) was used. The fits were performed self-consistently: The same fit parameters were used for identical spectral regions.

Figure 3.3: A photograph of the XPS setup (MAX 200) used in this PhD work and its components.

The effective thickness of the monolayers was calculated using a standard procedure [106], based on the C 1s/Au 4f intensity ratio. A standard expression for the attenuation of the photoemission signal was assumed [75]; attenuation lengths reported in ref [76] were used. To determine the spectrometer-specific coefficients, I took molecular films of known thickness as direct reference; the respective samples were measured under the same conditions as the aromatic SAMs. As reference films I used HDT monolayers on Au(111) which have a film thickness of 19.4 Å, which was calculated through the alkyl chain length (1.26 Å per CH_2 unit) [107], length of Au–S bond (2.4 Å) [108], and the molecular inclination (30°-33.5°) [3].

3.5 Fabrication of Gold Patterns

E-beam patterned SAMs (see Section 3.3) on Au/Si substrates were immersed in 20 mL of thiosulfate-based etching solution for 35 min at room temperature [109, 110]. The etching solution contained 1 M KOH, 0.1 M $K_2S_2O_3$, 10 mM $K_3Fe(CN)_6$, and 1 mM $K_4Fe(CN)_6$. Subsequently, the samples were washed with Millipore water and dried with Argon.

3.6 AFM Characterization of Gold Patterns

Fabricated gold patterns were characterized by atomic force microscopy (AFM). The measurements were performed with a Solver NEXT (NTMDT) controller in tapping (semi-contact) mode under ambient conditions.

3.7 Preparation of Carbon Nanomembranes (CNMs)

For the fabrication of SAM-based membranes, well-established protocols of refs [29, 30] were followed. In brief, the SAMs on gold were homogeneously irradiated by electrons (50 eV) with 40 mC/cm^2 dose. Then, a poly(methyl methacrylate) (PMMA) (AR-P 631.04) layer was spincast onto these irradiated SAMs (membrane) on gold for 30 s at 4000 rpm; next, the membrane/PMMA sandwich was baked on a hotplate at 55°C for 5 min and then a second PMMA (AR-P 671.04) layer was spincast and baked. The gold was dissolved in Lugol's solution (aqueous KI/I_2, 2%), and rinsed with water. Finally, the membrane/PMMA sheets were transferred to TEM grids and the PMMA layer was removed by a critical point dryer (Automated Critical Point Dryer, Leica EM CPD300) in order not to damage the CNMs because of surface tension occurring during the drying process. The free-standing membranes were characterized by SEM (Leo 1530, Zeiss) using an in-lens detector. For these purposes, the membranes were transferred to a TEM grid (Plano, 1500 mesh, copper, 11 μm opening width).

3.8 I-V Measurements

A home-built two-terminal junction setup, adapted from the works of Rampi et al. [40, 48] and von Wrochem et al. [111, 112], was modified according to our purpose to work with an EGaIn tip. The measurements were performed in the tunneling junction geometry, using the conductive Au substrate as the bottom electrode and the EGaIn tip as the top electrode. A CMOS camera with a Macro lens (The Imaging Source DMK22AUC03 1/3 in. Micron with MR 8/O) is placed across the sample to monitor the preparation of EGaIn tip and the contact between EGaIn tip and SAM surface. 5 µL of Ga-In eutectic (75.5 wt % Ga and 24.5 wt % In) was taken a Hamilton syringe (Autosampler Syringe 701ASRN) with a conical metallic needle that was electrically connected to Keithley 2635A source meter. Molecular junctions were formed by bringing the soft Ga_2O_3/EGaIn tip into contact with SAMs on Au substrates. The tip formation is shown in Figure 3.4. In brief, a small droplet of EGaIn is formed on the tip of the conical needle and is brought into contact with a sacrificial gold substrate to adhere on it. Afterwards, the needle is withdrawn slowly to get a conical GaIn tip. Once tip was formed, it was left for 5-10 min to form an oxide layer (Ga_2O_3). Measurements were done at ambient atmosphere and room temperature (relative humidity = 35-45%). 5-10 measurements at different places were performed for each sample and the average values were calculated. The contact area was estimated by analyzing the image taken by the camera. The current through the junction was recorded as a function of the applied voltage by using the Keithley source meter. Data points were collected using a voltage ramp with a bias interval of ~45 mV and an interval of at least 5 s between individual steps. The voltage was swept from -0.01 V to -0.5 V and 0.01 V to 0.5 V with a ~45 mV interval.

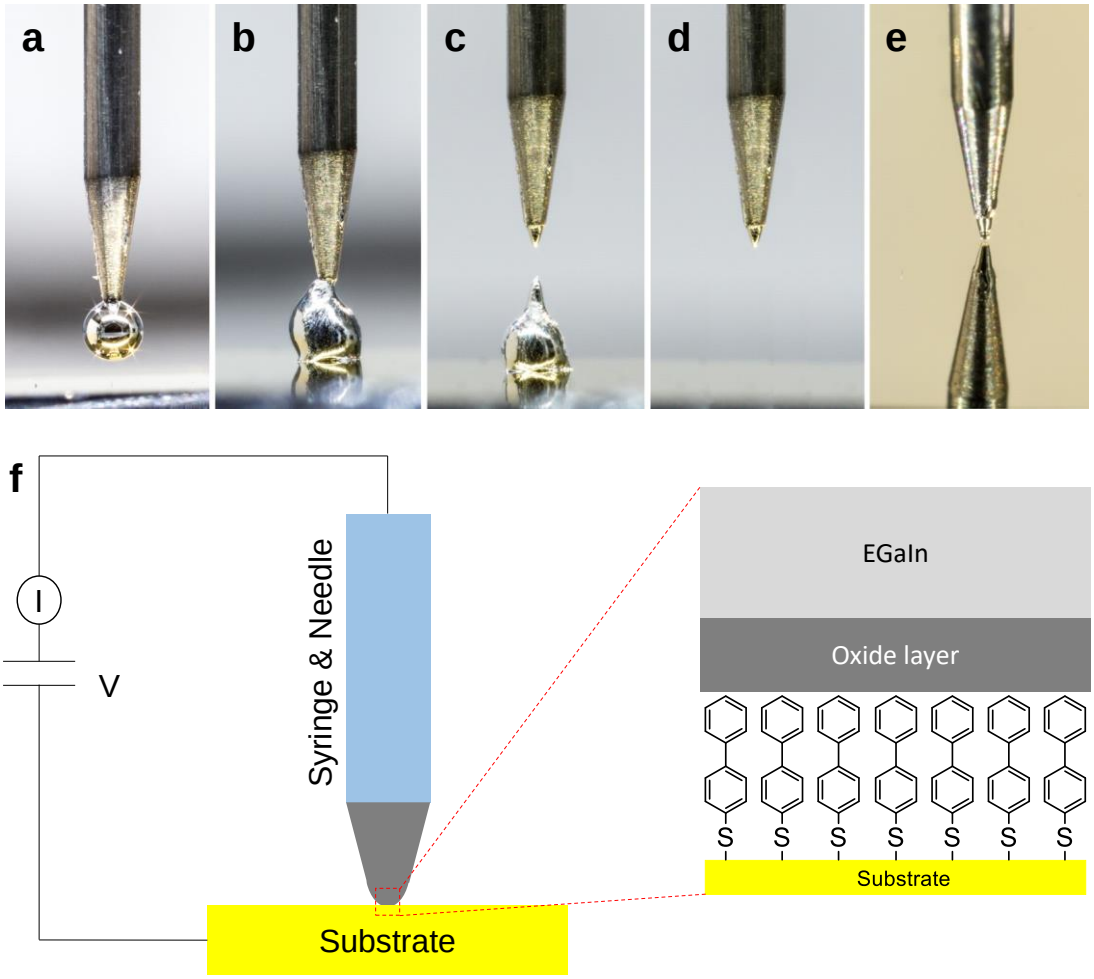

Figure 3.4: Formation of an EGaIn tip on a syringe needle is shown: (a) Make a droplet of EGaIn out of the needle; (b) bring the drop in contact with a sacrificial substrate (Au in this case) until it sticks; (c) pull the needle up slowly to form a sharp tip; (d) wait 5-10 minutes to passivate the tip with the oxide layer (Ga_2O_3) and (e) bring the tip into contact with the sample to be measured and form a junction (the tip is reflected in the metallic surface). (f) Schematic illustration of home-build junction setup used to make measurements of tunneling currents across SAMs. The diameter the contact between EGaIn and SAM shown in panel (f) was between 30 and 75 µm. The photographs shown here were taken in cooperation with Tobias Wächter (PhD student, APC Heidelberg) and Peter Jeschka (technical staff, APC Heidelberg).

3.9 WF Measurements

Work function (WF) measurements were carried out using a UHV Kelvin Probe 2001 system (KP Technology Ltd., UK). The pressure in the chamber was ~5×10^{-8} mbar. The calibration of the setup was done with sputtered gold, referenced to 5.2 eV. The in situ electron irradiation and WF measurements were done in the same analysis chamber by

using a HDT SAM on gold (WF=4.3 eV) as a reference after each irradiation. The measurements were carried out at room temperature.

4 Results and Discussion

In this chapter, the results of X-ray photoelectron spectroscopy, electron lithography, CNM fabrication, electric transport and work function experiments based on SAMs of acene, oligophenyl and OPE backbones are presented and the effect of electron irradiation on these SAMs is discussed. In addition, the effect of electron irradiation on pyridine-containing aromatic SAMs is also discussed through spectroscopic analysis. Note that, the terms "fused" and "non-fused" will be interchangeably used with the terms of "acene" and "oligophenyl", respectively.

4.1 Spectroscopic Experiments

The changes occurring in aromatic SAMs upon electron irradiation were monitored by XPS, taking AnthT, TPT and OPE3 SAMs as representative systems for the acene, oligophenyl and OPE series, respectively (see the figure below). The fabricated AnthT, TPT and OPE3 films on gold were irradiated by electrons with a kinetic energy of 50 eV. The irradiation was performed with fixed doses of 5/10/20/40/60 mC/cm^2. Sample preparation and analysis conditions are explained in *Experimental Part* (Chapter 3).

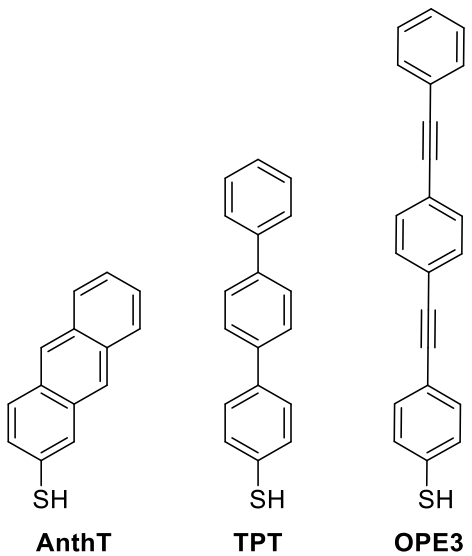

This is the same figure as shown in Chapter 1 (Figure 1.1).

The Au 4f spectra in Figure 4.1 exhibit the Au $4f_{7/2,5/2}$ doublet from the gold substrate. The intensity of the Au $4f_{7/2,5/2}$ components does not change noticeably with increasing dose, suggesting a very low extent (if any at all) of irradiation-induced desorption.

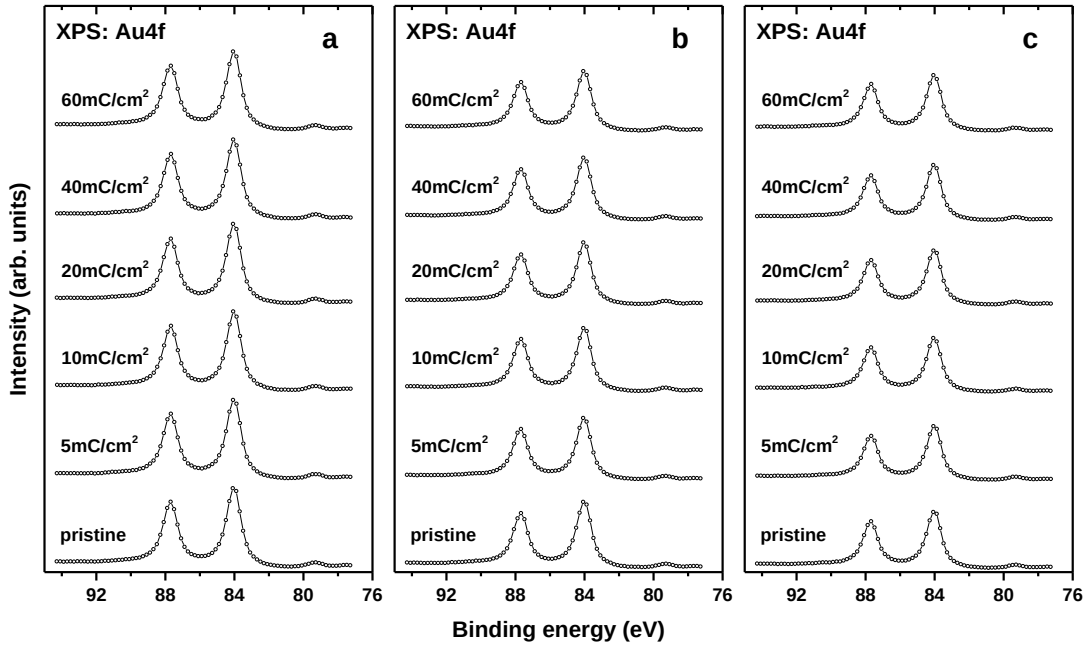

Figure 4.1: Au 4f XPS spectra of the pristine and irradiated AnthT (a), TPT (b), and OPE3 (c) SAMs. The doses are marked at the respective spectra. The energy of the electrons was 50 eV.

The characteristic C 1s XPS spectra of pristine AnthT, TPT and OPE3 SAMs in Figure 4.2 are dominated by an intense emission at BE positions of 283.94, 284.05 and 284.2 eV, respectively. These strong peaks correspond to their backbone originating from C−C bond in the aromatic structure [12, 113], followed by a weak shoulder at a ~1.8 eV higher BE, assigned to the carbon atom bound to the sulfur headgroup or to shake-up processes in the aromatic matrix (see discussion in ref [114]). The intensity of the C 1s peaks as well as the character and shape of the C 1s spectra of the SAMs do not exhibit any perceptible changes upon irradiation. This suggests, in agreement with the Au 4f data, a very low extent (if any at all) of irradiation-induced desorption, which is also supported by the behavior of the effective thickness. After an exposure of 60 mC/cm^2 dose, the BE values shift 0.22, 0.11 and 0.08 eV to higher energy level for AnthT, TPT and OPE3, respectively. In addition, C 1s signal broadening, depicted here as an increase in the FWHM values, (Figure 4.3) was observed indicating the loss of orientational and conformational order in the monolayer [13, 115]. The relation between carbon content and relative thickness is given in Figure 4.4 and they are

correlating to each other: An increase in carbon content corresponds to increase in thickness. Interestingly, after an exposure of 60 mC/cm^2 dose C 1s signal did not decrease (4 mC/cm^2 is sufficient to decrease the C 1s signal to 65% for HDT SAM) and an increase in thickness of the cross-linked SAMs was observed. The thickness of SAMs (calculated on the basis of the Au 4f signal; see *Experimental Part*) increased slightly upon electron irradiation, viz., from 11.2 to 11.3 Å for AnthT films, from 15.3 to 16.4 Å for TPT films and from 16.9 to 18.6 Å for OPE3 films (Figure 4.4). Such an increase is presumably related to adsorption of residual gas molecules on the irradiated SAMs [116, 117]. The doses applied (1 mC/cm^2 corresponds to ~13 electrons per SAM constituent) were obviously sufficiently high to induce such an adsorption even under UHV conditions in the electron irradiation chamber.

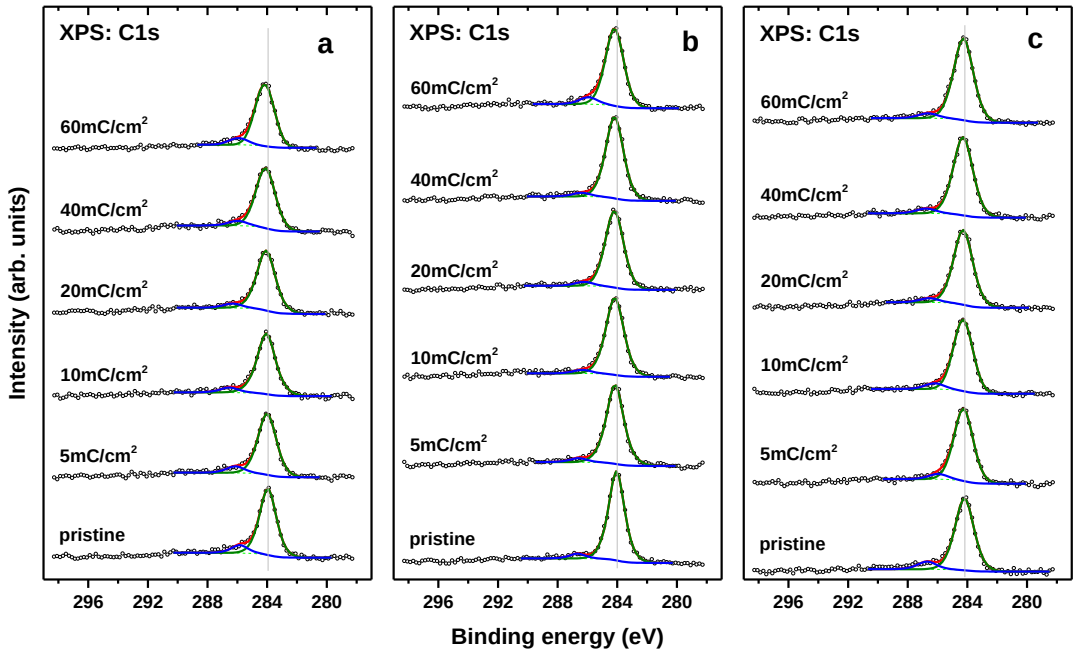

Figure 4.2: C 1s XPS spectra of the pristine and irradiated AnthT (a), TPT (b), and OPE3 (c) SAMs. The doses are marked at the respective spectra. The energy of the electrons was 50 eV. The C 1s spectra are decomposed into the component peaks, viz. the main peak (green lines) and a minor shoulder (blue lines); see text for details. Vertical solid lines highlight the BE positions of the peaks.

At first sight, XPS monitoring of C 1s signals (Figure 4.2) seems unaffected by electrons for all type of molecules. However, when it is analyzed from the perspective of BE shift and FWHM change (Figure 4.3), there is a continuous change in both FWHM and BE shift curves belonging to AnthT which could be attributed to the continuous orientational and conformational change in the monolayer [13, 115] (The

change in conformational order was previously explained in detail with near edge X-ray absorption fine structure spectroscopy (NEXAFS) in our groups' studies [13, 26, 27]).

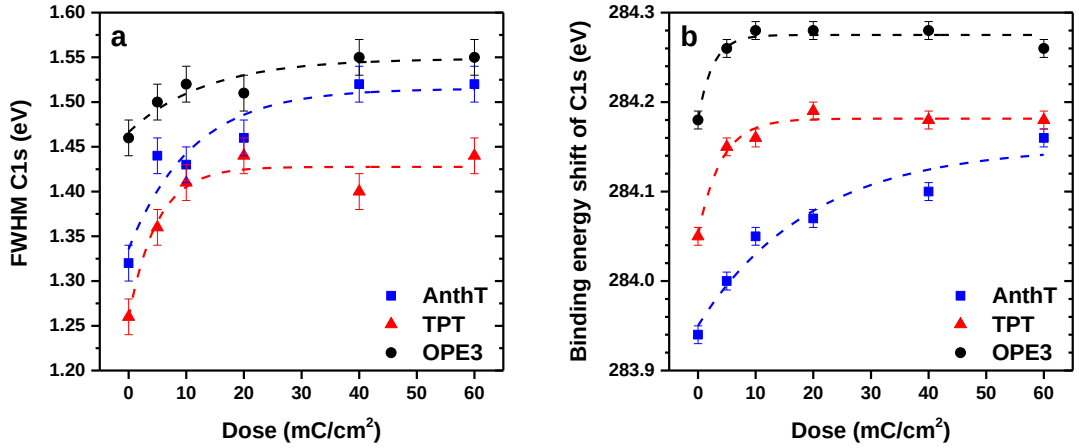

Figure 4.3: Dependence of the FWHM of the main C 1s peak (a), and BE position of this peak (b) for the TPT (red triangles), AnthT (blue squares), and OPE3 (black circles) SAMs on irradiation dose. The energy of the electrons was 50 eV. The parameters in panels (a) and (b) are fitted by exponential functions according to Eq. 4.1 (color-coded dashed curves).

Whereas, TPT and OPE3 films show such change till the exposure to 10 mC/cm^2 dose, and the maximum BE shift is getting smaller with increasing molecular length. These changes can be associated with progressive cross-linking of the SAM constituents, following the extensive cleavage of C−H bonds in the SAM matrix. The threshold for such processes lies at ~7 eV [11, 17], far below the electron energies in the experiments of this study.

Both BE positions and FWHMs of the main C 1s peak for the SAMs studied exhibit an exponential-like variation at low doses and a leveling off behavior at high doses. Such a behavior is typical for SAMs [14, 15] and can be described by a function

$$I = I_{sat} + (I_{pris} - I_{sat}) \times exp(-\sigma Q/eS_{irrad}) \quad (4.1)$$

where I is the value of a characteristic film parameter in a course of irradiation, I_{pris} and I_{sat} are the parameter values for the pristine and strongly irradiated films (a leveling off behavior), respectively, Q is the cumulative charge delivered to the surface in Coulombs, e is the electron charge, S_{irrad} is the area irradiated by the electron beam, and the cross-section σ is a measure of a rate at which the saturation behavior is achieved. The respective fitting curves are shown in Figures 4.3a and 4.3b, and the derived cross-

sections, averaged over the FWHM and C 1s behavior, are compiled in Table 4.1. The values for the TPT and OPE3 SAMs are similar while that for the AnthT monolayer is noticeably lower. The latter is probably related to the conjugated character of the AnthT backbone, so that the effect of the cross-linking, resulting in the formation of conjugated structures as well [16, 22, 118], is less pronounced in the C 1s XPS spectrum than in the TPT and OPE3 case. Significantly, the cross-sections in Table 4.1 correlate well with the literature values. The effective hydrogen content loss cross-section in the TPT SAMs on Au was estimated at $(2.7\text{-}4.7)\times10^{-17}$ cm^2 for electron processing at 50 eV by high-resolution electron energy loss spectroscopy and electron-stimulated desorption experiments [24], in an excellent agreement with our SAM matrix value of $(3.65\pm0.9)\times10^{-17}$ cm^2 for the same system. Significantly, this correlation suggests indirectly that our cross-section values for the modification of the SAM matrix, obtained on the basis of the C 1s XPS spectra, reflect predominantly the hydrogen content loss in the matrix.

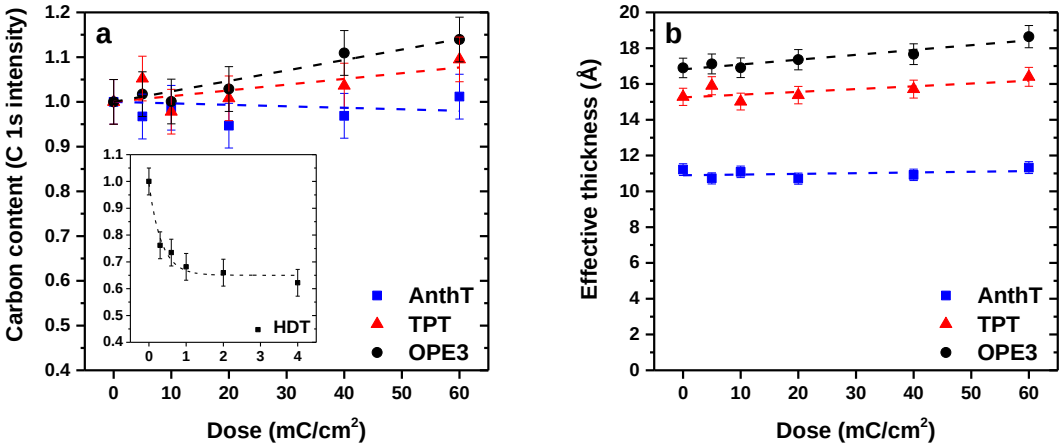

Figure 4.4: Dependence of the carbon content (a), and the effective thickness (b) for the TPT (red triangles), AnthT (blue squares), and OPE3 (black circles) SAMs on irradiation dose. The energy of the electrons was 50 eV. The straight, color-coded dashed lines in panels (a) and (b) are guides for the eyes. The inset in panel (a) shows the decrease in the carbon content of the HDT SAM till an irradiation dose of 4 mC/cm^2.

Along with the SAM matrix, the SAM-substrate interface was modified upon the electron irradiation as follows from the S 2p XPS spectra of the SAMs shown in Figure 4.5. For pristine samples the characteristic S 2p doublet has a S $2p_{3/2}$ BE of 162 eV which is typical for a thiolate species bonded to the gold surface [16, 113, 119] (Figure 4.5) with no traces of atomic sulfur, disulfide, unbound sulfur or oxidized species. The intensity of the thiolate related doublet in the pristine SAMs decreases with increasing molecular length, manifesting a stronger attenuation of the S 2p photoelectrons by the

thicker TPT and OPE3 films. During irradiation thiolate bond intensity decreases exponentially and a second sulfur species simultaneously appears to be at ~163.1-163.4 eV which corresponds to the irradiation-induced cleavage of the Au−S bonds and has been previously associated with the formation of disulfide species [2, 10] but most likely have C–S–C character [10] trapped in the monolayer matrix.

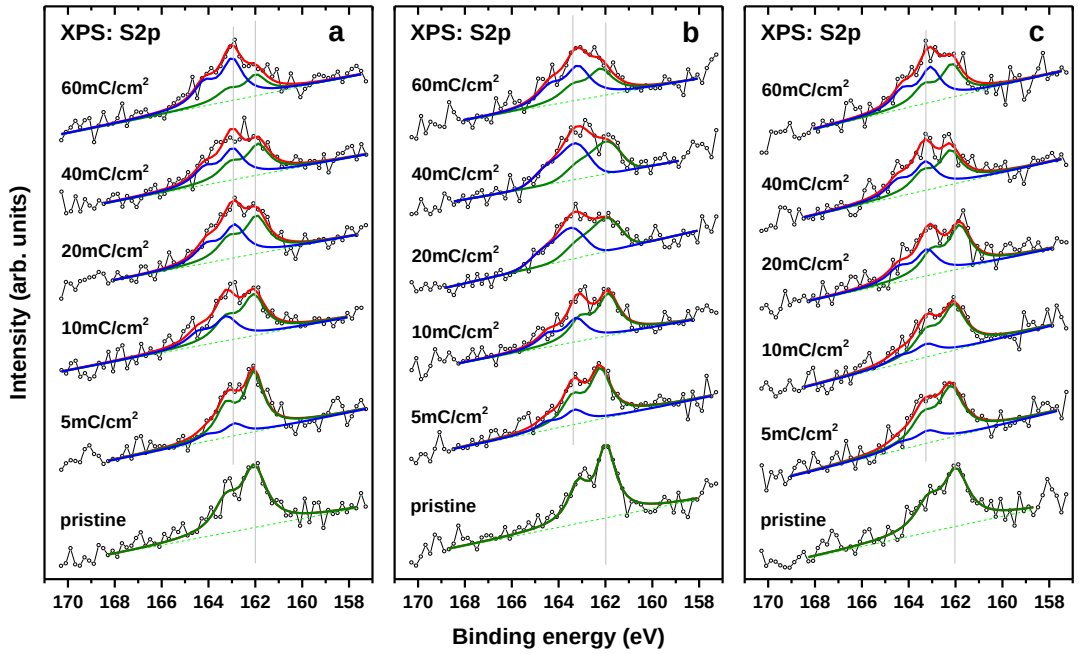

Figure 4.5: S 2p XPS spectra of the pristine and irradiated AnthT (a), TPT (b), and OPE3 (c) SAMs. The doses are marked at the respective spectra. The energy of the electrons was 50 eV. The S 2p spectra are decomposed into the component doublets corresponding to the pristine thiolate species (green lines) and irradiation-induced sulfur species (blue lines); the sum of these components is drawn by the red lines. Vertical solid lines highlight the BE positions of the doublets.

As seen from Figure 4.6 the total intensity of S 2p signals of the aromatic SAMs studied did not decrease upon irradiation which, along with the Au 4f and C 1s XPS data, suggests a very low extent of the irradiation-induced desorption in the studied SAM (apart from the H desorption, following the cleavage of C−H bonds). Similar behavior was also observed for a two-ring molecule, nitrile terminated biphenylthiol [2]. It was attributed partly to the thickness reduction and partly to the breakage of the Au−S bonds, which leads to formation of an additional doublet at ~163.2 eV in the S 2p XPS spectra. The thickness increase in the monolayers leads to a higher attenuation of the S 2p signal for all sulfur-containing species [2], while progressive propagation and capture of the released sulfur species in the aromatic matrix results in a closer placement of such species with respect to the SAM-ambience interface, giving a more intense S

2p signal. As described above, while thickness increase (higher attenuation of S 2p) reduces the total sulfur intensity, radiation induced released sulfur species located in the aromatic matrix increases it, therefore, almost no change in the total sulfur intensity is observed in our case. In comparison to alkanethiol SAMs, both cleavage of the Au−S bonds and the degradation of the released species are noticeably slowed by the cross-linking in the aromatic network as shown by the curves in Figure 4.6. In contrast, 70% of all Au−S bonds are broken at a dose of only 1 mC/cm^2 in the case of alkanethiol SAM (e.g. HDT, Figure 4.6d) in which molecular defragmentation is superior to cross-linking [11, 14, 17, 20, 21].

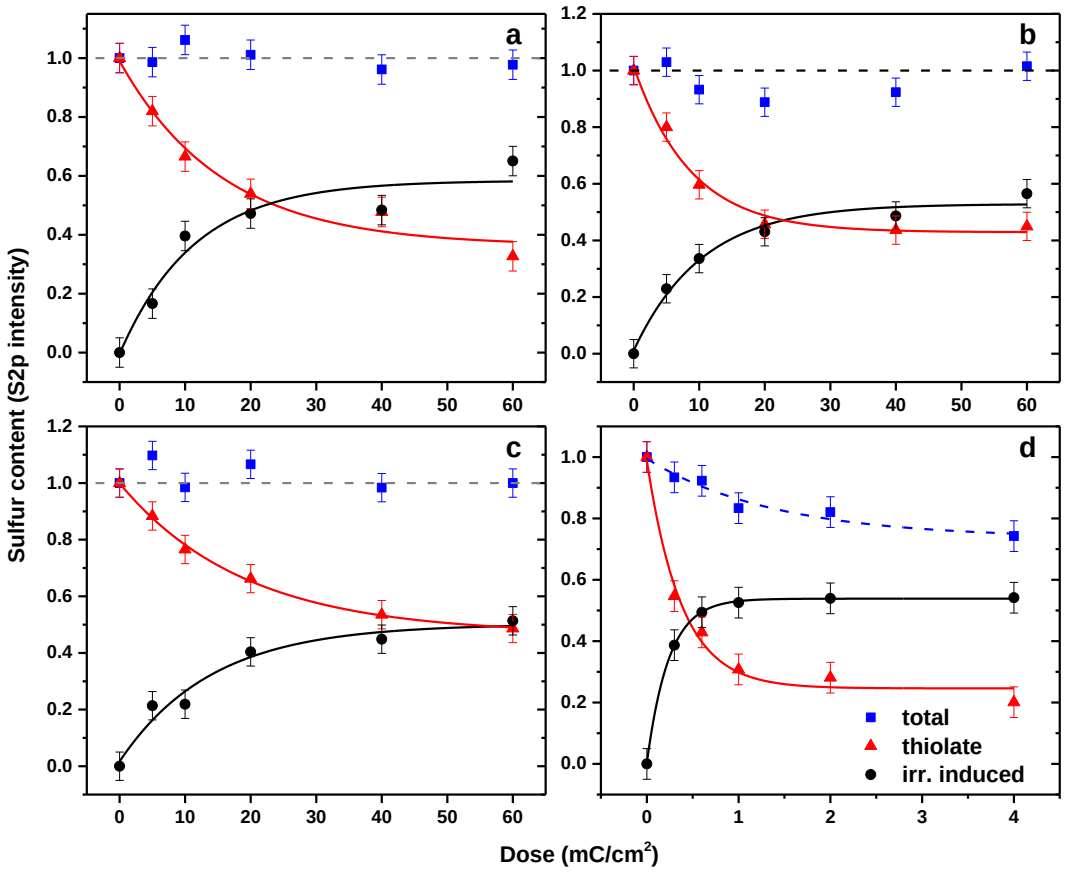

Figure 4.6: Dependence of the total intensity of the S 2p signal (blue squares), intensity of the S 2p component corresponding to the pristine thiolate species (red triangles), and intensity of the S 2p component corresponding to irradiation-induced species (black circles) for the TPT (a), AnthT (b), OPE3 (c), and HDT (reference) (d) SAMs on irradiation dose. The intensities of the above components are fitted by exponential functions according to Eq. 4.1 (red and black solid lines, respectively). The gray dashed lines correspond to 1 and are meant as guides for the eyes. The energy of the electrons was 50 eV.

Table 4.1: Cross-sections of the irradiation-induced processes involving the SAM matrix and the SAM/substrate interface; see text for details. The values were determined from the spectroscopic experiments. For the AnthT SAMs, effective cross-section of the cross-linking, determined from the lithographic experiments (see Section 4.2), is given. The units are 10^{-17} cm^2.

Monolayer	TPT	AnthT	OPE3
SAM matrix	3.65±0.9	1.15±0.5	3.8±1.5
SAM/Au interface	1.7±0.3	1.2±0.4	1.0±0.2
cross-linking		10±3	

At the same time, the intensities of the doublets corresponding to the thiolate and irradiation-induced species exhibit an exponential-like variation at low doses and a leveling off behavior at high doses. Using similar approach as in the case of the C 1s spectra, fitting according to Eq**.** 4.1 could be performed. The respective fitting curves are shown in Figure 4.6, and the derived cross-sections are compiled in Table 4.1, averaged over the curves describing the intensities of S 2p component doublets corresponding to the thiolate and irradiation-induced species. These cross-sections are quite similar for the SAMs studied, with the highest value for the TPT monolayer and the lowest value for the OPE3 monolayer, which are in accordance with literature values. For example, the cross-section for the electron beam (50 eV) damage of the SAM-substrate interface in the BPT SAMs on Au was estimated at 1.75×10^{-17} cm^2 (average value for the damage of the pristine headgroups and formation of new, sulfur-derived species) in a series of independent experiments [120], which is very close to the value of $(1.70\pm3)\times10^{-17}$ cm^2 obtained for the TPT monolayers in the present work. At the same time, these parameters are by almost two orders of magnitude lower than the analogous value for the reference HDT SAM ($5.5\pm0.4\times10^{-16}$ cm^2) where the irradiation-induced damage dominates over cross-linking. Note that, for HDT the thiolate cross-section is obtained only after 4 mC/cm^2 dose. In contrast, in the aromatic SAMs, including those of the present study, extensive cross-linking, occurring quite fast in the course of irradiation, prevents and quenches any displacement of the SAM constituents, necessary for the cleavage of the Au−S bonds, hindering the respective processes. Even if a bond can be broken, it can recombine if the respective "fragments" stay in place [121]. This is certainly true for such "fragment" as the substrate, but is also

the case for the assembled molecules as far as they do not only interact weakly with each other but are covalently linked to the matrix.

4.2 Lithographic Experiments

Cross-linking behavior in the aromatic matrix can only be monitored indirectly by spectroscopic experiments because of the lack of characteristic features for this process, even though the desorption of H, following the cleavage of C–H bonds and representing a prerequisite for the cross-linking, can be directly monitored based on the characteristic vibration modes [12, 13, 22, 24] or by mass-spectrometry [17, 24]. Therefore, complementary lithographic experiments were performed. The idea of these experiments was to monitor the resist performance of the SAMs studied as function of the irradiation dose and electron energy, providing also a direct proof of the suitability of these films for electron lithography. Two sets of the experiments were performed. Within the first set, a pattern of square-like features was "written" by EBL using a scanning electron microscope with a pattern generator system (see Chapter 3 for details). The irradiation dose was varied from one square-like feature to another at a fixed electron energy, which, in its turn, was varied from pattern to pattern (0.5, 1, 3 and 5 keV). Within the second set, a pattern of circle-like features was "written" by PPL using the same electron source (a flood gun) and the same electron energy (50 eV) as for the spectroscopy experiments (see Chapter 3 for details). This allowed to correlate the results of the spectroscopic and lithographic experiments. All patterns were etched using the same procedure and imaged by SEM (not shown) and AFM afterwards (see Chapter 3 for details).

4.2.1 Electron beam lithography experiments

The fabricated PT, NphT, BPT, OPE2, AnthT, TPT and OPE3 films on gold (75nm) were patterned by EBL. The irradiation was performed with fixed doses of 1/2/5/10/20/40/80/100/150 mC/cm^2 with kinetic energies of 0.5, 1, 3 and 5 keV. Later, all samples were etched in same thiosulfate based etching solution for 35 min at room temperature. Figure 4.7 shows the representative drawing of e-beam patterning of the SAMs and related pattern formation upon etching.

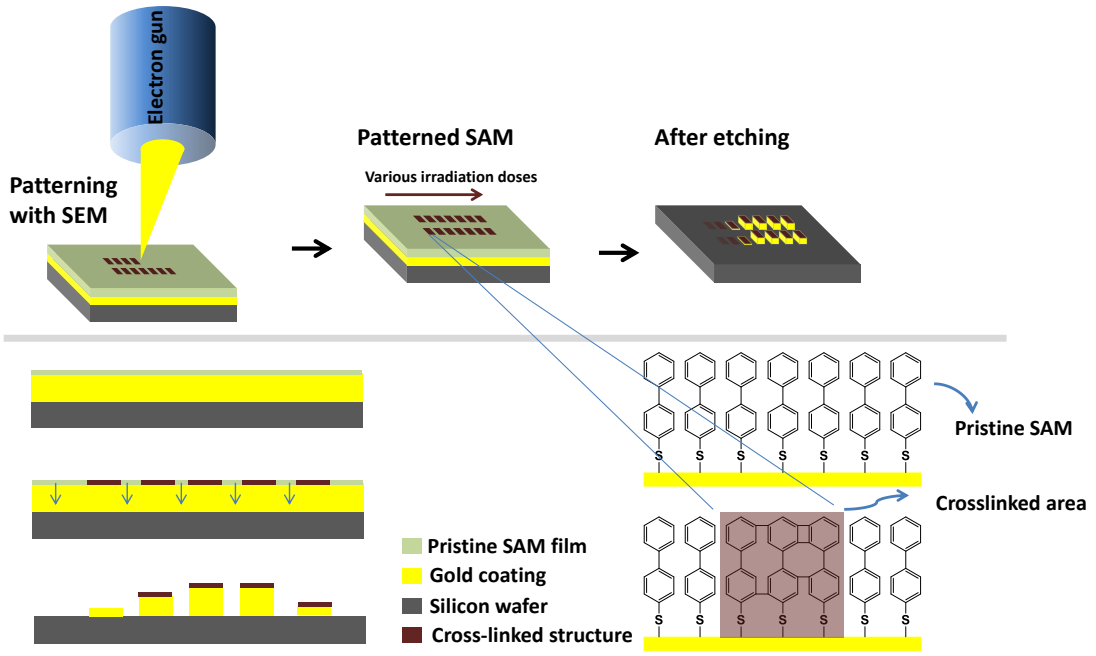

Figure 4.7: Representative drawing of e-beam patterning of aromatic SAMs, and a side view of the process for the fabrication of gold patterns.

It was mentioned in the previous section that the electron irradiation modifies aromatic SAMs different than aliphatic ones, where the irradiation leads to disorder in conformation and orientation of the monolayer, desorption of monolayer fragments, and dehydrogenation of the molecules with C=C double bond formation [11, 20]. After electron irradiation, because of the aforementioned changes, aliphatic SAMs fall into a

Table 4.2: XPS thickness, area per molecule and packing density of the pristine SAMs used in this section. The values were determined from the XPS spectra of the SAMs.

Molecules	XPS thickness (Å)	Area per molecule (Å^2/molecule)	Packing density (molecules/cm^2)
PT	5.7±0.4	31.6	3.17×10^{14}
NphT	8.4±0.5	24	4.17×10^{14}
BPT	10.4±0.6	25.9	3.86×10^{14}
OPE2	9.5±0.6	27.7	3.61×10^{14}
AnthT	11.2±0.6	26.1	3.83×10^{14}
TPT	15.3±0.8	21.9	4.56×10^{14}
OPE3	16.9±0.8	22.8	4.39×10^{14}
HDT (reference)	19.4±0.1	21.6	4.63×10^{14}

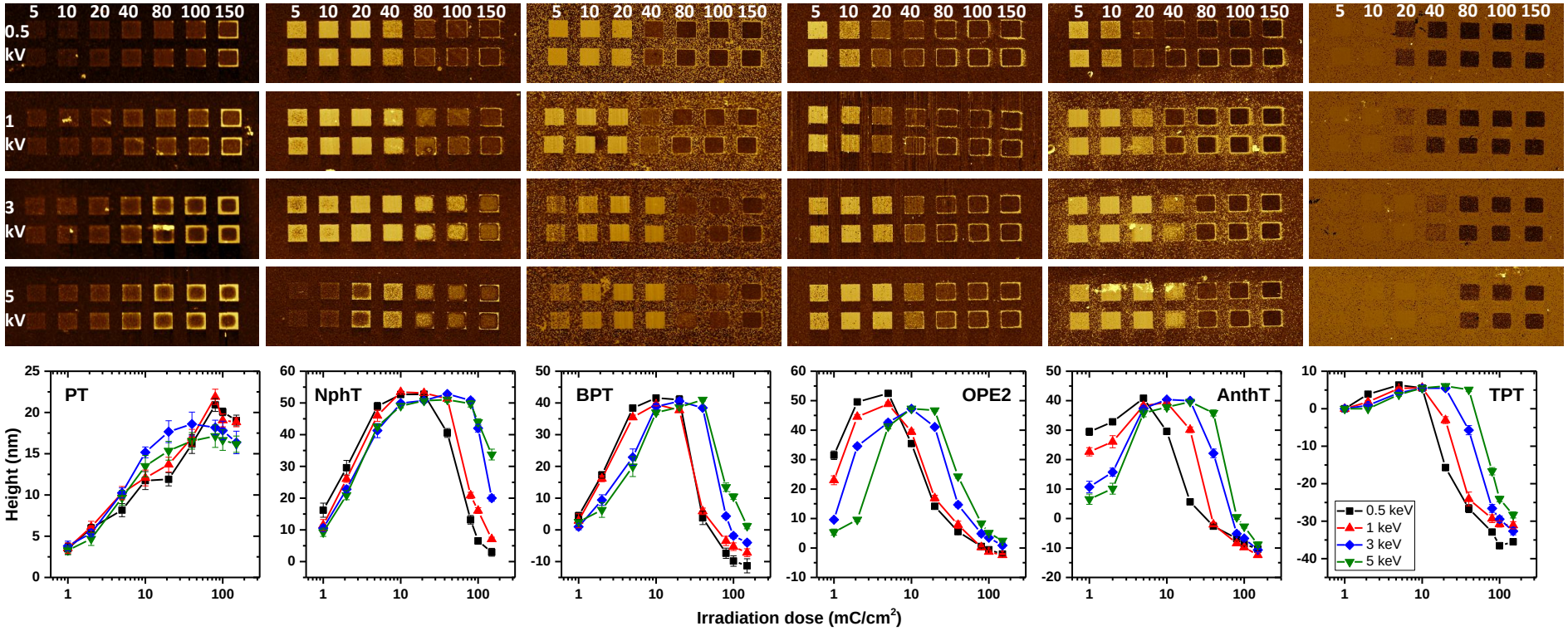

Figure 4.8: AFM images of Au/Si(100) patterns prepared by EBL with the SAM resists and respective dependence of the height of the square-like gold features in the patterns shown below the each set of images on irradiation dose. The patterning was performed at electron energies of 0.5 keV (black squares and black curve), 1 keV (red up triangles and red curve), 3 keV (blue diamonds and blue curve), and 5 keV (green down triangles and green curve) from top to down. The doses corresponding to the individual square-like Au features were 5, 10, 20, 40, 80, 100 and 150 mC/cm^2 (from left to the right).

less stable layer which acts as positive resist. In contrast to aliphatic SAMs, electron irradiation increases the stability of aromatic SAMs by inducing cross-linking between the molecules, therefore, they act as negative resist. After etching, the areas exposed to irradiation show a contrast both in SEM and AFM images when compared to non-exposed surrounding areas [12].

The ability of aromatic SAMs as a negative resist for EBL was first shown by Geyer et. al [12] (our institute). However, so far, most of the experiments related to electron lithography, relying on the aromatic SAMs, was performed with biphenyl-based monolayers [12, 16, 19, 37, 122]. With this regard, to test the suitability of different aromatic SAMs for lithographic purpose, 3 µm square patterns on the SAMs, continuously increasing the dose from square to square, were written and later the samples were etched. Also, 2 µm squares (AFM images of the patterns from NphT SAM is given in Appendix (Figure A.1), representative of the all other SAMs) were written in the same way starting from 1 mC/cm^2 dose. The AFM images of the respective patterns are shown in Figure 4.8. Accordingly, an increase in the pattern height with increasing dose range, (under-dose range), followed by a plateau (optimal dose range), and a decrease (over-dose range) was observed. The initial increase in the pattern height with increasing dose level shows the insufficient dose to cross-link the whole irradiated area and leads to partial cross-linking of the monolayer and partial etching of the underlying gold substrate. At the optimal dose range, cross-linked monolayers are strong enough not to allow etching ions to penetrate the layer, and thus, exhibit negative resist ability. Figure 4.9b shows non-irradiated and irradiated areas with optimal dose after exposing them to etching, and the cross-linked structure (irradiated area) seems to be very efficient to protect the underlying gold. Figure 4.9a shows the pattern heights obtained after immersion of the samples for same etching time (35 min) and it shows that there is a length dependence of pattern heights. In over-dose range, the features prepared at higher doses (see Figures 4.8 and 4.11) mimic the perimeters of the written squares and a decreasing height profile was observed which could be due to the peeling of the membrane (in the form of CNM) occurred upon etching. The only explanation for this behavior is a release of the entire cross-linked SAM within the irradiated area upon the etching, in the form of CNM. Indeed, with increasing doses, cross-linking becomes more extensive but the anchoring to the substrate gets impaired progressively (see Figures 4.5 and 4.6). Accordingly, the cross-linked SAM can be easily released in the etching solution as soon as the irradiation dose

is sufficiently high, leaving the underlying Au substrate unprotected against the etching. The observed perimeter-like Au structures instead of the initially written square-like features can then be only related to the joint effect of the backscattered primary electrons and the secondary electrons from the substrate [123]. These electrons are reflected and emitted not only within the irradiated areas but also along their perimeter, providing a lower irradiation dose then that by the combined effect of the primary, backscattering, and secondary electrons within the irradiated spots. Accordingly, the SAM along the perimeter is still well-anchored to the substrate and somewhat cross-linked, providing a protection against the etching. The formation of perimeters taking place at higher doses indicates the proximity effect which occurs with the peeling (release of the CNMs) independent from molecule type (please see Appendix A.2).

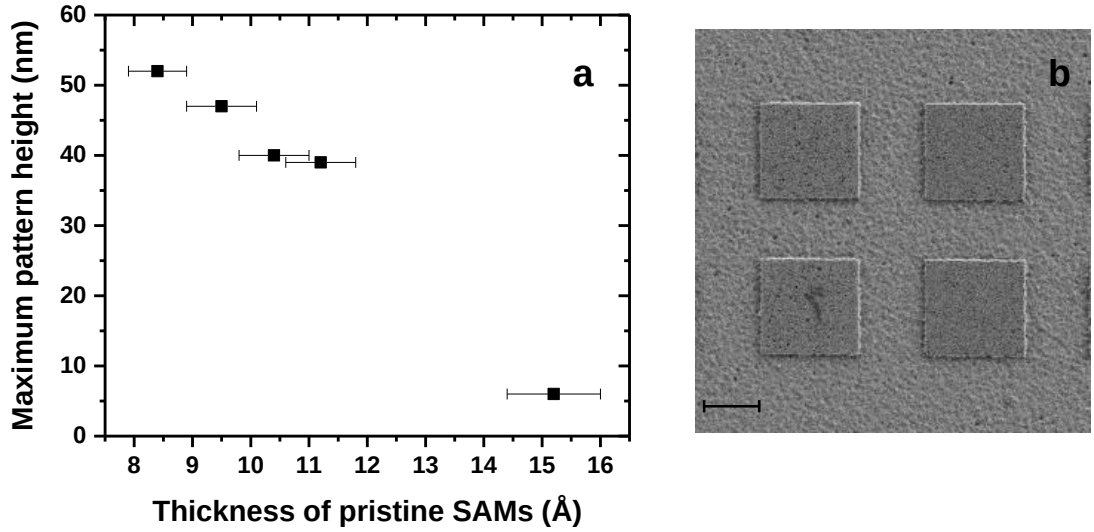

Figure 4.9: The maximum pattern heights obtained from lithographic experiments versus film thickness of the pristine SAMs (a) and an SEM image of an NphT SAM on gold (b) patterned with EBL at 0.5 kV and at optimal dose range. In the given case, the squares at left and right side were formed with 10 mC/cm^2 and 20 mC/cm^2 doses, respectively. The scale bar in panel (b) corresponds to 2 µm. The maximum heights correspond to the average of the maximum heights from all electron energies (at 0.5, 1, 3 and 5 keV energies). The thickness values were obtained from XPS measurements.

Below I will discuss the etching ability of the pristine (non-irradiated) SAMs which is an important parameter to evaluate their resist ability. The most possible way of etching gold substrate over a SAM monolayer is that etchant ions pass through the pristine (non-irradiated) monolayer and reach the gold surface and start to etch by forming gold ions. While SAMs of all molecules can easily be etched, three-ring molecules (TPT and OPE3) SAMs cannot be etched as shown in Figure 4.10 (only performance of TPT

SAM is shown). This is probably related to the densely packed structure of TPT SAM, which does not allow etchant molecules to pass through the pristine monolayer presumably due to steric hindrance and etch the underlying gold substrate. Thus, not the non-irradiated but the irradiated areas become preferably etched, resulting in an inverse (positive) contrast of the lithographic patterns. Nevertheless, such a contrast can be much more easily achieved with the aliphatic SAMs, which by themselves represent a positive resist for lithographic applications [15]. However, SAMs of another three-ring molecule, perfluoroterphenyl-substituted alkanethiols [70], could give lithographic contrast which was most probably because of the flour atoms in the molecules. These flour atoms relatively increase the molecular spacing between the adjacent molecules (forming less densely packed monolayer), thus, allowing etching agents to pass through the monolayer and resulting in etch of the underlying substrate. Therefore, even though a correlation between the pattern height and the molecular length can be seen in Figure 4.9a, the packing density also seems to be important for the etching ability of the monolayers, along with the molecular length.

To prove the effect of this parameter (etching ability), some area (much larger than XPS spot) on the surface of TPT sample was shadowed with a mask and irradiated (50 eV) with 20 mC/cm^2 dose. Surprisingly, XPS spectra (Figure 4.10) from both shadowed and irradiated regions of 45 min etched sample show that both pristine SAM and cross-linked SAM are still on the gold surface. Thiolate bonding belonging to the shadowed area is still intact and only a small percentage (10-15%) of it is oxidized, which can be seen from the peak arising around 168 eV. On one hand, this indicates that these three-ring molecules are forming a very stable monolayer against etchants with their densely-packed structure and molecular length, which prevent etching ions penetrating this layer to a high extent as it was observed both in SEM, AFM and XPS analyses. On the other hand, it could indicate that etching of gold film takes place with the diffusion of ions through the membrane, which is facilitated probably by the loosely connected membrane to the gold surface (because of broken Au−S bonds). Figure 4.9 shows the relation between the effective film thickness and pattern height; every molecule has a different maximum height because of an induction time, a required time to remove the SAM from the gold and/or to overcome the steric hindrance. For instance, while NphT has a maximum height 53 nm, TPT has only 5-6 nm pattern height and OPE3 cannot give any gold pattern height profile, which are in correlation with the length of the molecule. However, as I mentioned above it is evident that not only molecular length

but also packing density of the SAM has a crucial role on the fabrication of gold features, explaining the effect of etching ability factor.

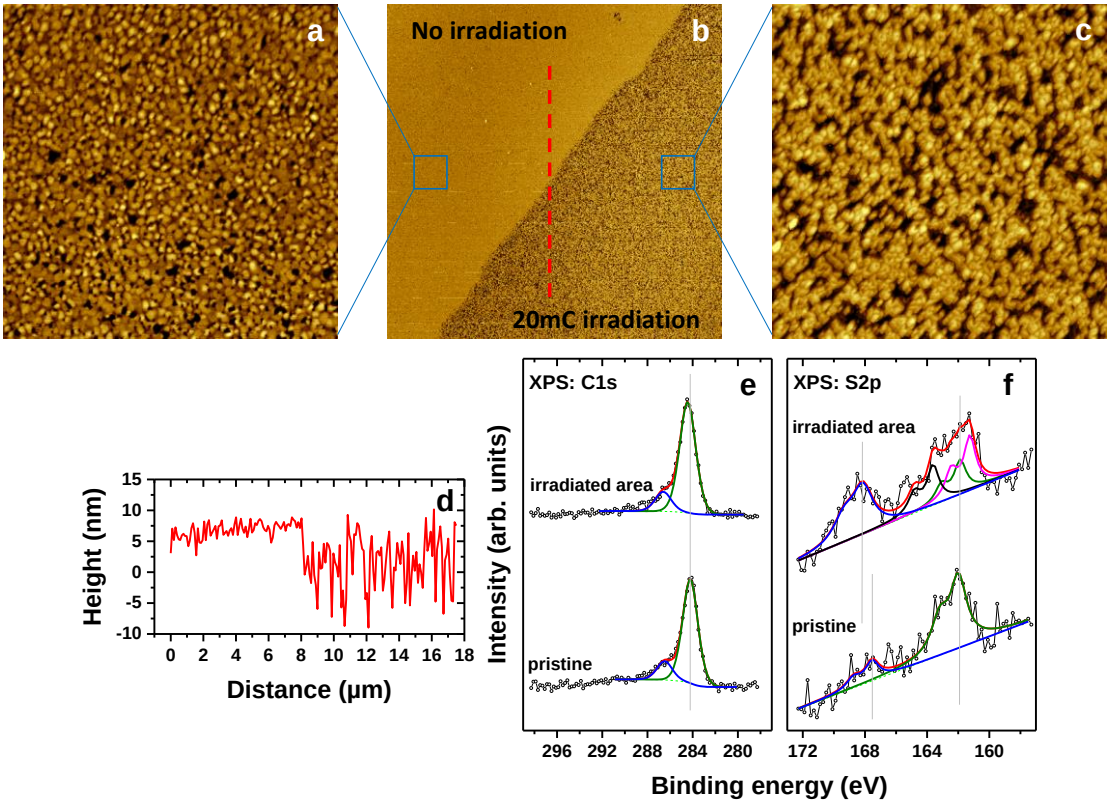

Figure 4.10: AFM images of TPT SAM from the pristine (non-irradiated) (a) and irradiated areas (c) of the same sample (b). The respective images were taken after etching the sample for 45 min. The height profile the red dashed line in panel (b) is given in panel (d). The C 1s (e) and S 2p (f) XPS spectra of both irradiated and non-irradiated areas are shown. The vertical grey solid lines in panel (e) and (f) show the BE position of the main peaks in each spectrum.

Further, the influence of the primary energy of electrons on the dose-dependent height of the patterns were studied. The respective results are presented in Figure 4.8 where the pattern heights are plotted as a function of irradiation dose for different energies of electrons. It can be seen that the maximum height and bell-like curves for all molecules are almost free from the energy while the respective dose shifts to higher values with increasing energy of the primary electrons, and this behavior can be explained by a joint impact of the primary, backscattered and secondary electrons that are responsible for all the irradiation-induced processes in the SAMs. In the applied energy range (0.5-5 keV), both the backscattering factor [124] and the secondary electron yield (with the maximum yield at ~500 eV) [125] decrease with increasing electron energy. These decreases are in agreement with the curves presented in Figure 4.8, thus, lead to the

shift of the optimal dose to higher doses with increasing electron energy. It should be noted that the secondary electrons presumably provide the major effect for cross-linking of the monolayers, and the energy provided by these electrons are fully sufficient for the mediation of the major irradiation processes as long as certain threshold value (~7 eV) is reached [11, 17].

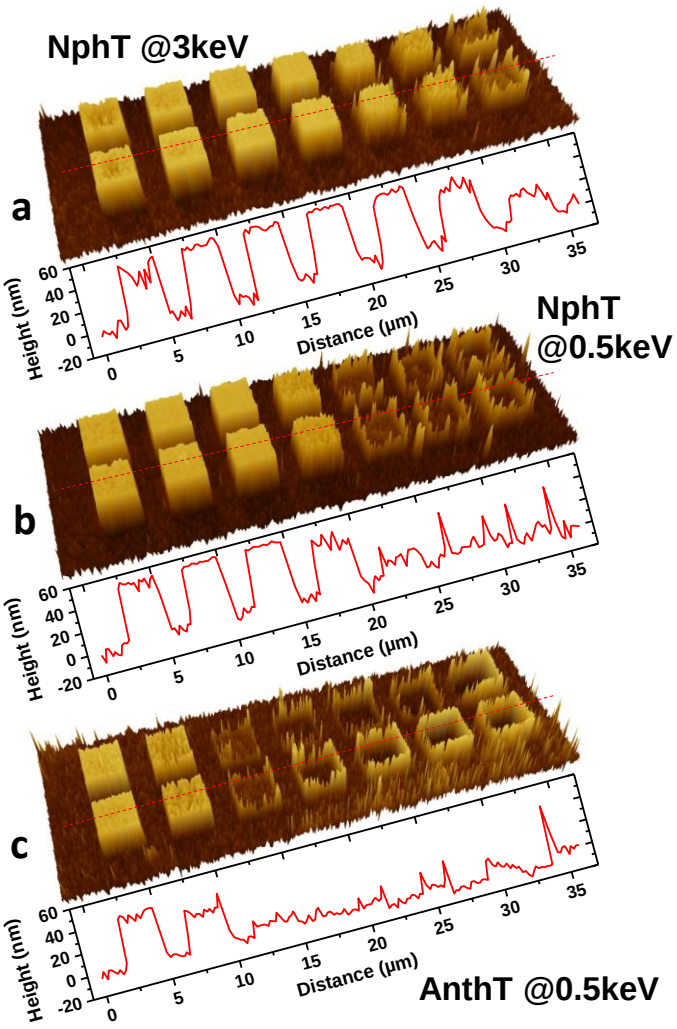

Figure 4.11: AFM images (3D representation) of Au/Si(100) patterns prepared by EBL with the SAM resists as well as the height profiles along the lines shown in the images. The patterning was performed with the NphT (a, b) and AnthT (c) SAM resists at energies of 3 keV (a) and 0.5 keV (b, c). The doses corresponding to the individual square-like Au features were 5, 10, 20, 40, 80, 100 and 150 mC/cm^2 (from left to the right).

Interestingly, there are clear effects of the SAM thickness and the electron energy, as was especially obvious in the EBL experiments. The transfer from the well-defined

pattern to the etching-mediated CNM release occurs at lower doses for the thicker SAMs (compare Figures 4.11b and 4.11c) and at a lower electron energy for the same SAM (compare Figures 4.11a and 4.11b). This means that the cross-linking is more efficient for a thicker monolayer, which is understandable considering that the irradiation-induced cleavage of C−H (and C−C) bonds, which is a prerequisite for the cross-linking, can be quenched by the interaction with the substrate [11, 17]. The efficiency of such a quenching decreases with increasing distance to the substrate and is, accordingly, less efficient, for longer molecules, resulting in a higher extent of cross-linking. An additional effect in this context is a stronger cross-linking in the vicinity of the SAM-ambient interface as compared to the SAM-substrate one for any particular film [26].

The effects of the SAM thickness and electron energy were observed for all three-series studied (oligophenyls, acenes, and OPEs). Note that the first member of all three series, PT/Au, exhibited a negative resist behavior as well, even though with inferior performance (lower contrast of the lithographic patterns) as compared to the monolayers comprised of the longer molecules. This is understandable since most of the molecular models of cross-linking involve simultaneous cross-linking of several rings of a particular molecular backbone, which is necessary for the formation of an extended, 2D polymer-like network [16, 22, 118]. One ring is obviously not enough to form such a network of comparable quality. In contrast, all two-ring systems performed quite well as negative lithographic resists, until the onset of the spontaneous CNM release at high irradiation doses. The AnthT film performed similar as well (but only at low doses), in contrast to the TPT and OPE3 monolayers which did not provide reasonable lithographic patterns under the conditions of the experiments in this study. To quantify the results of the lithographic experiments the height of the square-like gold features in the patterns prepared with the SAM resists were plotted as function of irradiation dose. The observed dependencies in Figure 4.8 could be fitted by a first order exponential function, following the formula used for e-beam induced changes in C 1s spectra (Eq. 4.1):

$$h = h_{pattern} + \left(h_{prist} - h_{pattern}\right) \cdot exp\left(-\frac{\sigma Q}{e.S_{irrad}}\right) \tag{4.2}$$

where h is the value of a characteristic film parameter in the course of irradiation, h_{prist} and $h_{pattern}$ are the thickness of the Au film (substrate) and height of the Au features, respectively, Q is the cumulative charge delivered to the surface in Coulombs, e is the

electron charge, S_{irrad} is the area irradiated by the electron beam, and the cross-section σ (expressed in cm^2) is a measure of a rate at which the saturation behavior is achieved.

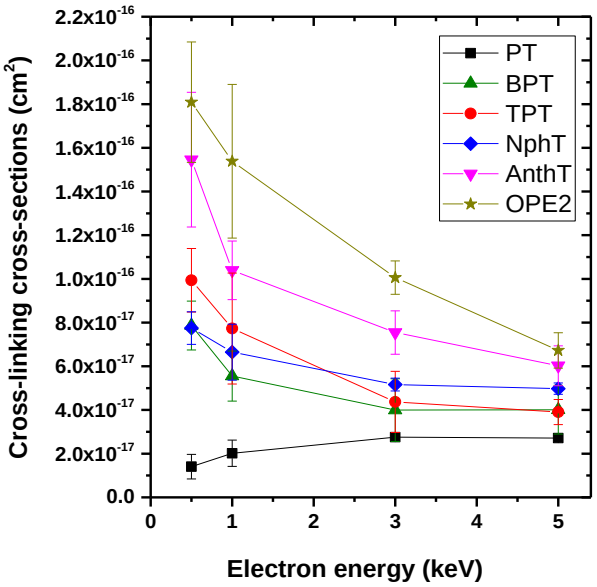

Figure 4.12: Dependence of the cross-sections for irradiation-induced cross-linking on the electron energy for the SAMs of this study. The values were determined from the lithographic experiments.

The calculated cross-section values for the cross-linking of the aromatic monolayers are presented in Figure 4.12 as a function of electron energy. The observed decrease in cross-section values with respect to energy correlates well with the secondary electron yield of the gold substrate [125], which is also supported by the shifts in dose-dependent height profiles (Figure 4.8) of the gold patterns. These shifts correspond to the data points in Figure 4.12, by calculating thickness variation of patterns from Figure 4.8 as a function of dose. Note that, cross-section values of OPE3 SAM are not possible to calculate from the pattern heights because no pattern formation was available after etching the OPE3 sample. The cross-section value for the cross-linking of AnthT film at 1 keV (it seems that 50 eV corresponds to 1 keV from Figure 4.12) is 1 order of magnitude higher than that of damage on thiolate bond (discussed in the previous section for 50 eV, see Table 4.1). Otherwise, extensive damage of the SAM/substrate interface (breakage of Au−S), occurring at the very low irradiation doses in the films where the cross-linking is a minor process only, could not be prevented, suggesting that the cross-linking of the monolayer takes place earlier than the damage of the SAM-substrate interface.

The final issue of this part is the performance of the SAMs studied as negative resists for electron lithography. According to the experiments, the two-ring systems (BPT, NphT, and OPE2) are most suitable for this purpose, but the dose should be carefully selected to be high enough to initiate sufficient cross-linking but low enough to avoid a spontaneous release of CNM pieces in the case of wet etching procedure. A dose of 10-20 mC/cm^2 appeared to be most suitable at 0.5-1 keV (see Figure 4.11) and is somewhat higher, up to 30-40 mC/cm^2, at higher primary energies. In contrast, the PT SAMs exhibited a poor performance as resist, which is presumably related to a limited extent of 2D cross-linking, associated with one-ring system (see above).

4.2.2 Proximity printing lithography

In the previous subsection, performance of aromatic SAMs was tested in the framework of EBL. To see the same behavior for the proximity printing lithography (PPL), AnthT SAM, representative of all other monolayers of this study, was selected to study the effect of dose at 50 eV electron energy on the resist performance. For this purpose, AnthT films on Au/Si were irradiated through a TEM grid having 1 μm circular holes as a stencil mask by varying the doses and subsequently immersed into gold etching solution. This resulted in well-defined gold patterns as illustrated by the AFM images (Figure 4.13a-i). The height profiles in these figures correspond to the thickness of the gold layer deposited on the silicon substrate by PVD (75 nm). While the big extent of gold film was etched away within the non-irradiated areas and appeared dark, the gold film was efficiently protected by the cross-linked AnthT film in the areas treated by the electron beam and appeared bright.

The PPL performance (Figure 4.13) of AnthT SAMs, representative of all other monolayers of this study, at 50 eV energy is similar to the EBL performance of these films (see Figure 4.8 for AnthT SAM), which is expected due to the same underlying irradiation-induced processes. While the predefined, circle-like features were observed at the low doses (Figures 4.13 d, e, f), perimeter-like patterns were formed at the high doses (Figures 13 h, i), following the release of the cross-linked SAM within the irradiated areas. Accordingly, to obtain the best resist performance, an optimal dose should be chosen according to the energy of the primary electrons. Note that higher irradiation load could lead to a higher extent of cross-linking [16], however, as observed in EBL experiments, proximity effect and release of the CNMs are the restrictive points

for high doses. Therefore, to use aromatic SAMs as a negative resist one should not exceed the optimal dose range.

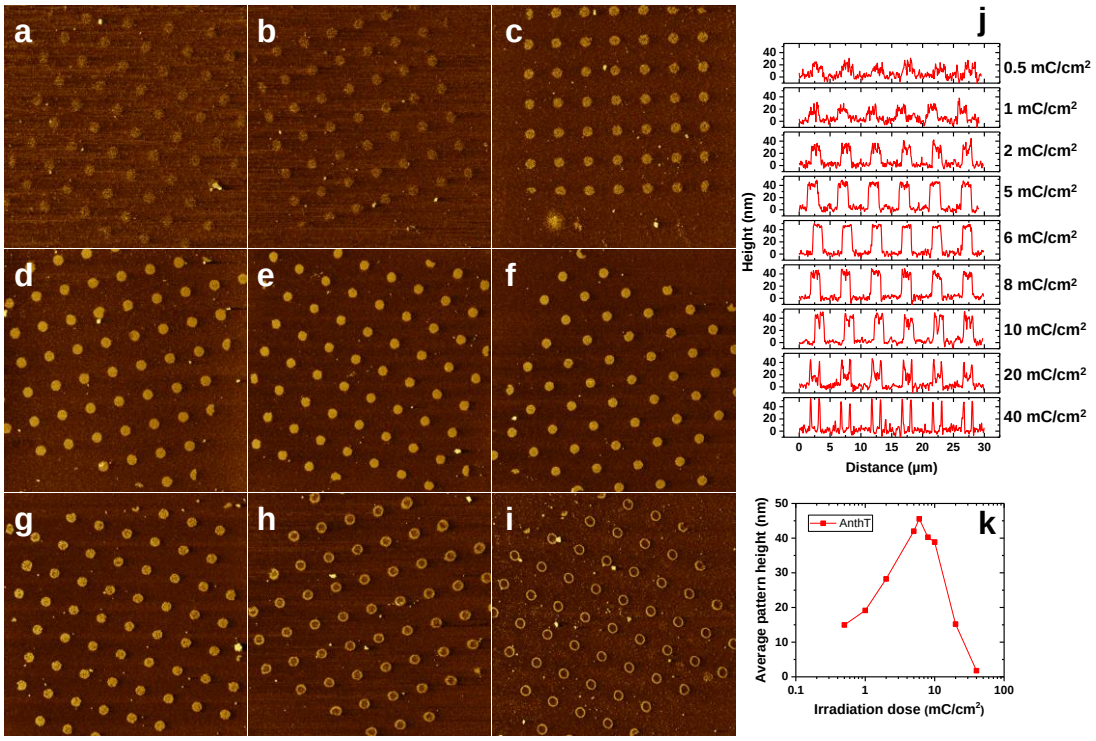

Figure 4.13: AFM images of an e-beam patterned gold on Si(100). The patterning was performed with the AnthT SAM resists in proximity printing geometry (see text for details). The energy of the electrons was set to 50 eV. The doses were 0.5 (a), 1 (b), 2 (c), 4 (d), 6 (e), 8 (f), 10 (g), 20 (h) and 40 mC/cm^2 (i). The panels (a), (b) and (c) show low-dose; (d), (e) and (f) optimal dose, and (g), (h) and (i) over-dose. The panel (j) and (k) are the height profile over 6 circular gold patterns and the corresponding mean pattern thicknesses, respectively.

By studying the kinetics of this process, cross-section value for cross-linking (50 eV) could be calculated from the same formula (Eq. 4.2) described in the previous subsection (for EBL experiments). Combining PPL and EBL cross-sections together (Figure 4.14), it can be said that the observed dependence of the cross-section value mimics the secondary electron yield of the underlying substrate with respect to electron energy [125]. As can be seen in Figure 4.14, from 50 to 500 eV, the cross-linking cross-section increases, and after 500 eV for increasing electron energy, the cross-section value decreases. This dependence clearly explains the effect of secondary electrons which are responsible for the mediation of the cross-linking in aromatic SAMs, together with primary and backscattered electrons.

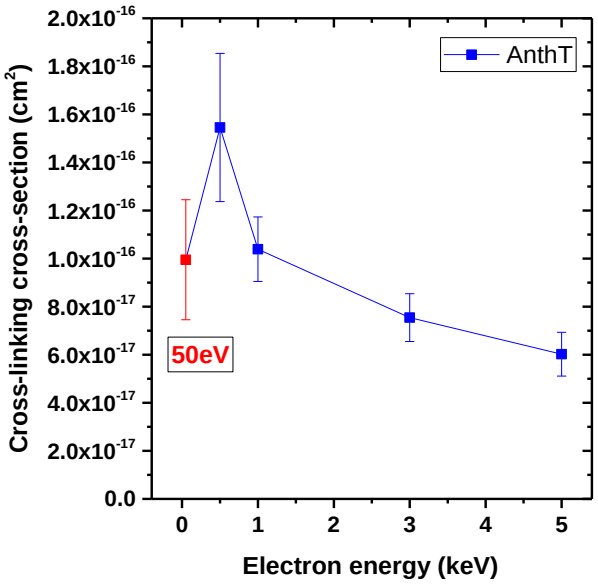

Figure 4.14: Dependence of the cross-sections for irradiation-induced cross-linking on the electron energy for the AnthT SAM. The values were determined from the lithographic experiments. The value corresponding to an electron energy of 50 eV is provided. This value was determined in the separate experiments (see text for details).

In addition, a direct comparison to the spectroscopy-derived values can be done for the AnthT SAM only (see Table 4.1 and Figure 4.14) since the same primary energy (50 eV) was applied in both spectroscopic and dedicated lithographic experiments. The values for the other SAMs, obtained at the higher electron energies only, can be tentatively scaled following the behavior of the curve for the AnthT film (Figures 4.12 and 4.14); accordingly, the cross-sections at 50 eV are similar to those at 1 keV.

The energy dependence of the cross-linking cross-section for the AnthT SAM in Figure 4.14 represents a bell-like curve, mimicked, starting from 500 eV, by the analogous curves for all other SAMs of this study with the exception of PT/Au which seems to be a special case (see above). Significantly, the modification of the SAMs is mediated not only by the primary electron beam but also by the backscattering (elastic) and secondary (true) [123] electrons. The electron backscattering factor depends on the atomic number and energy, being quite large for Au (close to 1.0 at 500 eV) [124]. Significantly, it decreases with increasing electron energy [124], similar to the cross-section curves in Figure 4.14 (starting from 500 eV). The secondary electron yield exhibits a bell-like behavior with increasing electron energy, with a maximum at ~500 eV for gold [125], mimicking the curve for the AnthT SAM in Figure 4.14. Accordingly, a significant effect of the secondary and backscattering electrons within the entire impact of the

electron irradiation can be assumed, at least at high kinetic energies, above 500 eV. In particular, this effect is responsible for the perimeter-like "decoration" of the predefined spots in the lithographic pattern written with a high dose (Figures 4.11 and 4.13). For low kinetic energies, such as e.g. 50 eV, the contribution of the secondary electrons is believed to be small, referring, however, to specific, resonant dissociative electronic attachment processes [24], whereas non-resonant processes, leading also to the loss of H, can be mediated by the secondary electrons as well. Note that the yield of the true secondary electrons is generally higher than that of the backscattering, elastic electrons, except for very low primary energies (less than 30 eV), but they mostly have low kinetic energies, with a maximum of the distribution centered at 6-7 eV [123]. Consequently, some of the secondary electrons are well capable to cleave C−H bonds, since the threshold for the respective process was estimated at ~7 eV [11, 17].

4.3 Fabrication of CNMs

Besides their suitability for lithographic applications, aromatic SAMs can be transformed into ultrathin, free-standing carbon nanomembranes (CNMs) [28-37] with tunable thickness (0.5-3 nm) and porosity [35] where different precursor molecules can be used. These membranes have mechanical strengths with 10-20 GPa (Young's moduli) [30, 36] and aspect ratio of more than 10^6 [37]. Furthermore, they can be converted to graphene sheets by annealing the CNMs at elevated temperatures [30, 34, 35, 37]. Fabrication of this kind of membranes necessitates the use of electron irradiation which cross-links the molecules within the SAM. In this regard, with a fixed irradiation dose of 40 mC/cm^2 (50 eV), all aromatic SAMs were homogenously irradiated, and later, all cross-linked structure removed from their gold substrate following the protocols in literature [29, 30, 32]. Transfer of the membranes on TEM grids was done according to the established procedure [35].

Figure 4.15 shows SEM images of membranes stretched over copper TEM grids with 1500 mesh (Plano, 11 μm opening width). While all molecules formed CNMs on TEM grids, one ring molecule, PT, could not form free-standing membrane most probably because of its mechanically instable structure: In comparison to other molecules, PT has the lowest carbon content and packing density, which are the most restrictive probable reasons not to form a membrane with enough mechanical strength. Also, even

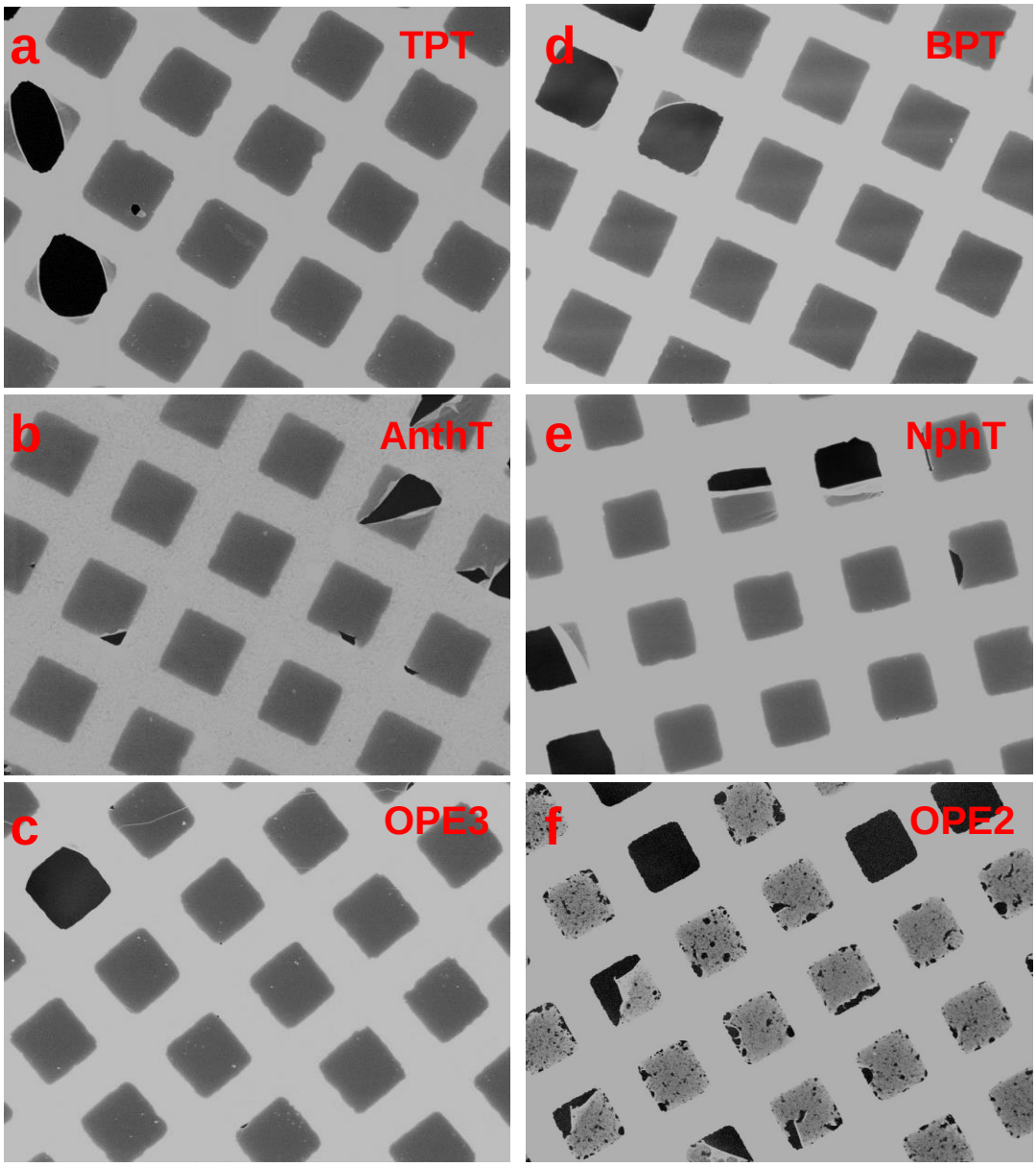

Figure 4.15: SEM images of the CNMs prepared from the TPT (a), AnthT (b), OPE3 (c), BPT (d), NphT (e) and OPE2 (f) SAMs. The CNMs were supported by copper grids (1500 mesh, Plano).

though the CNM of OPE2 could be fabricated, the SEM image of OPE2 membrane (Figure 4.15f) contained a lot of disrupted pieces. It seems to be mechanically not very stable in comparison to other molecules as seen from Figure 4.15f, which is presumably because of its low packing density (see Table 4.2). In SEM images, it is clear to distinguish the areas where the CNMs cover the TEM grid openings (gray-white squares) and non-covered openings or broken membranes (black areas). It should be noted that the most direct way to see the modification of monolayers by electron irradiation is the fabrication of membrane where molecules within the SAM film are

cross-linked, through which a quasi 2D polymeric layer with mechanical stability is formed as observed for the molecules used in this study.

4.4 Electric Transport Experiments

As a follow-up for the spectroscopic and lithographic experiments, the electrical properties, in particular static conductance, of aromatic SAMs were studied by two-terminal junction method using an eutectic Ga-In (EGaIn) as the top electrode and the conductive gold substrate as the bottom electrode. EGaIn was chosen due to its good electrical conductivity [126], nondamaging character to SAMs [126], easiness to use and advantage to characterize larger areas than other methods [38, 127] such as STM and conductive AFM. With the results obtained, it was also possible to derive the effect of backbone type on the electrical properties of aromatic SAMs. In this regard, the fused, non-fused and OPE ring SAMs on gold were irradiated with 10, 20 and 40 mC/cm^2 doses. Later, I-V measurements were carried out by two-terminal junction where the current through the SAM was measured according to the applied voltage which was sweeped from -0.01 V to -0.5 V, and from 0.01 V to 0.5 V at room temperature under ambient atmosphere (humidity: 40-50%). Note that, in this study, no temperature dependent measurements (related to hopping or thermionic emission) were carried out. The possible conduction mechanisms for SAMs are given in Table 2.1 and can be obtained from the mathematical translation of the classical I-V measurements. The mainly observed mechanisms for the SAMs used here are the non-resonant (direct) and the Fowler-Nordheim tunneling regimes.

Current density−bias voltage plots at different irradiation doses of the fused, non-fused and OPE ring series are presented in Figures 4.16a, 4.16b and 4.16c, respectively. The error bars are typical for this type of junction and are the statistical error and the uncertainty in estimating the contact area between the electrodes [40, 41]. The graphs show that there is a similar behavior of all molecules upon electron irradiation: Conductance of all molecules decreases with increasing irradiation dose. The decrease in fused and non-fused systems are roughly two orders of magnitude after 40 mC/cm^2 dose, while that of OPE system is only one order of magnitude. To have a closer look to the effect of e-beam on the conductance of SAMs, logJ values at -0.5 V were plotted

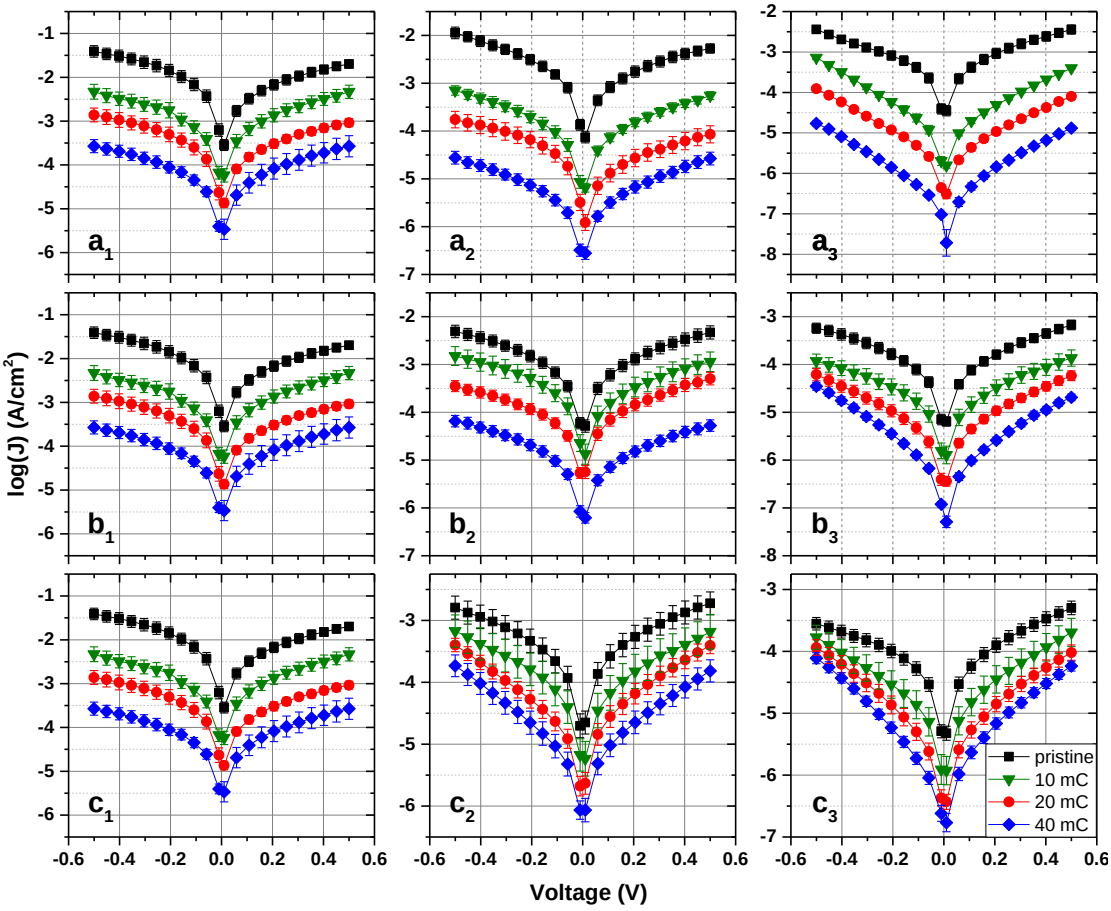

Figure 4.16: Comparison of log(J) versus voltage for molecular junctions of pristine and irradiated SAMs from acene (a_1, a_2, a_3), oligophenyl (b_1, b_2, b_3), and OPE (c_1, c_2, c_3) backbones using PT (a_1, b_1, c_1) as the first member in each series assigned with subscript '1'.

as a function of irradiation dose (Figure 4.17). As can be seen from Figure 4.17, it is clear that the lowest decrease in conductance belongs to the OPE backbone showing the most stable ring structure upon irradiation, which was also verified with XPS analysis of C 1s and S 2p signals (see Section 4.1), while, the most drastic change belongs to the fused rings (acene backbone). The decrease in conductance could be related to the changes both at gold/SAM interface and within the SAM film. The former is the decreased chemical contact between gold substrate and SAM (Au−S bond), and the latter is the disorder in the aromatic monolayer (see Section 4.1). As discussed in Section 4.1 the damage of SAM-substrate interface (remaining amount of Au–S bond) for the acene backbone is slightly more than oligophenyl and OPE backbone. The effect of disorder in the monolayer on conductance can be explained with the following estimation. The change in conformational and orientational order for acene backbone was expected to be larger than other backbone types because of their highly-conjugated

rigid ring structure which leads to a lack in torsion of the backbone. Since the rings in the backbone do not have rotation freedom, during electron irradiation, a larger and continuous loss of order in the monolayer takes place, which can be monitored with the FWHM and BE of C 1s signal (Figure 4.4). Whereas, in the case of oligophenyl backbone, the rings have the torsional freedom, therefore, they can make the cross-linking with the adjacent molecules easier than acene ones, therefore, less decrease in the SAM order and less decrease in the conductance. In addition, the observed decrease in current density upon irradiation was also mentioned in ref [38] and assigned to combined effects coming from enhanced barrier at the gold/cross-linked SAM interface, disorder in the SAM upon irradiation (cross-linking and partial loss of aromaticity) and an alignment of molecular orbitals with respect to the Fermi levels of the electrodes. The irradiation treatment modifies the electronic structure of aromatic SAMs by resulting in reduction in HOMO-LUMO gaps [16, 128, 129]. The increase in barrier height will be explained by the contact resistances in the following paragraphs.

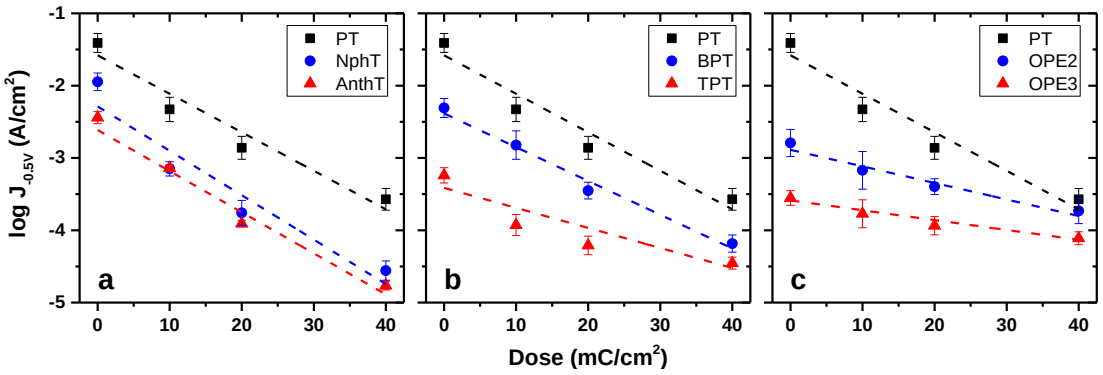

Figure 4.17: Comparison of log(J) values at -0.5 V of acene (a), oligophenyl (b) and OPE (c) backbones as a function of irradiation dose. The dashed lines represent the respective linear fits.

When one looks at the current densities of all pristine molecules in Figure 4.18a, it is obvious that all curves are correlated with the molecular length of the SAM precursors. This means that there is a dependence of current flowing through the SAMs on the length of molecular junction, and Figure 4.18b depicts this dependence clearly. Although the length of the molecule seems to be the main parameter affecting the conductance (Figure 4.18b), the identity of backbone has the major role on the conductance which can be described with another parameter, tunneling decay parameter (β). When the current density values of the same backbone at the same voltage are plotted in a logarithmic fashion (Figure 4.18c), β values can be obtained from the linear

fits of the data points of the same ring structure, and are different than those of others (which will be discussed in the following paragraph).

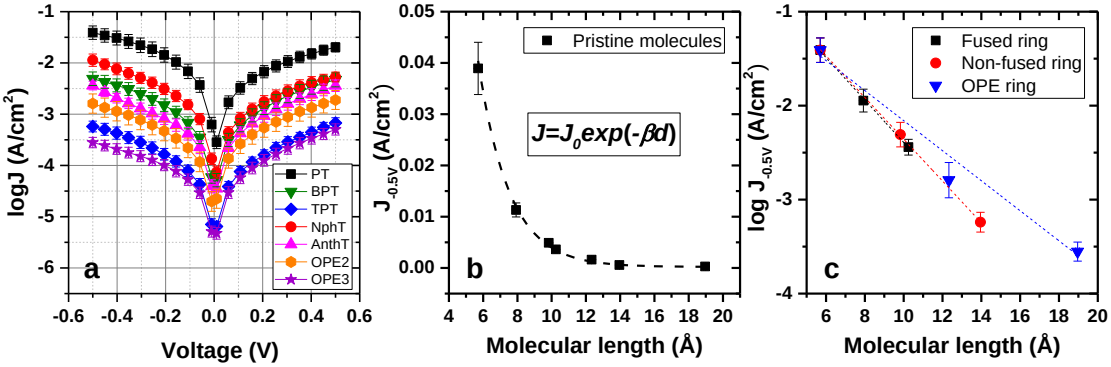

Figure 4.18: Semilog plot of current density of the pristine SAMs as a function of the bias voltage between the EGaIn and gold electrodes for the EGaIn-SAM-Au junctions (a). Current density (at -0.5 V) of the pristine SAMs versus molecular length (b). The dashed black line shows the exponential fit of the data points. Semilog plot of current densities (at -0.5 V) of the pristine SAMs versus molecular length (c). The data points of each backbone are shown with a linear fit (dashed lines).

One important parameter to characterize the charge transport properties of SAMs is the tunneling decay constant (β) which contains information about the height of the tunneling barrier [50]. It can be derived from simplified approximation of the Simmons model as shown in Eq. 4.3 where the charge transport through molecular junction is dominated by a tunneling mechanism, the current decays exponentially with the length of molecule and β is obtained as it is shown in Figure 4.18b [130]:

$$J = J_0 \exp(-\beta d) \tag{4.3}$$

J and J_0 are current and injection densities (A/cm^2) at an applied voltage V, respectively. The effective thickness of the molecular junctions is denoted as d (Å). Note that, in this equation, it is assumed that tunneling barrier is rectangular or close to rectangular [50]. The molecular length of the precursors was estimated by using ChemDraw 3D software, assuming that all molecules are in an extended and in trans conformation. The length of the molecules was calculated from the sulfur headgroup to the topmost hydrogen atom. In calculations, for pristine SAMs sum of the molecular lengths obtained by ChemDraw 3D software and length of Au–S bond (2.4 Å) was used as the effective thickness, while for irradiated SAMs the effective thicknesses obtained by XPS were used. Irradiated SAMs, because they form a 2D carbon network, contain no pristine molecules, which form molecular tunnels for charge transport, as it is the case in

pristine SAMs. It should be taken into account that upon irradiation the effective film thickness of two-ring films decreases 5-10% according to XPS analysis of pristine films, while three-ring films show thickness increase, which was explained in Section 4.1. However, for PT SAM (one-ring), the thickness decrease is even more pronounced at around 30% lower.

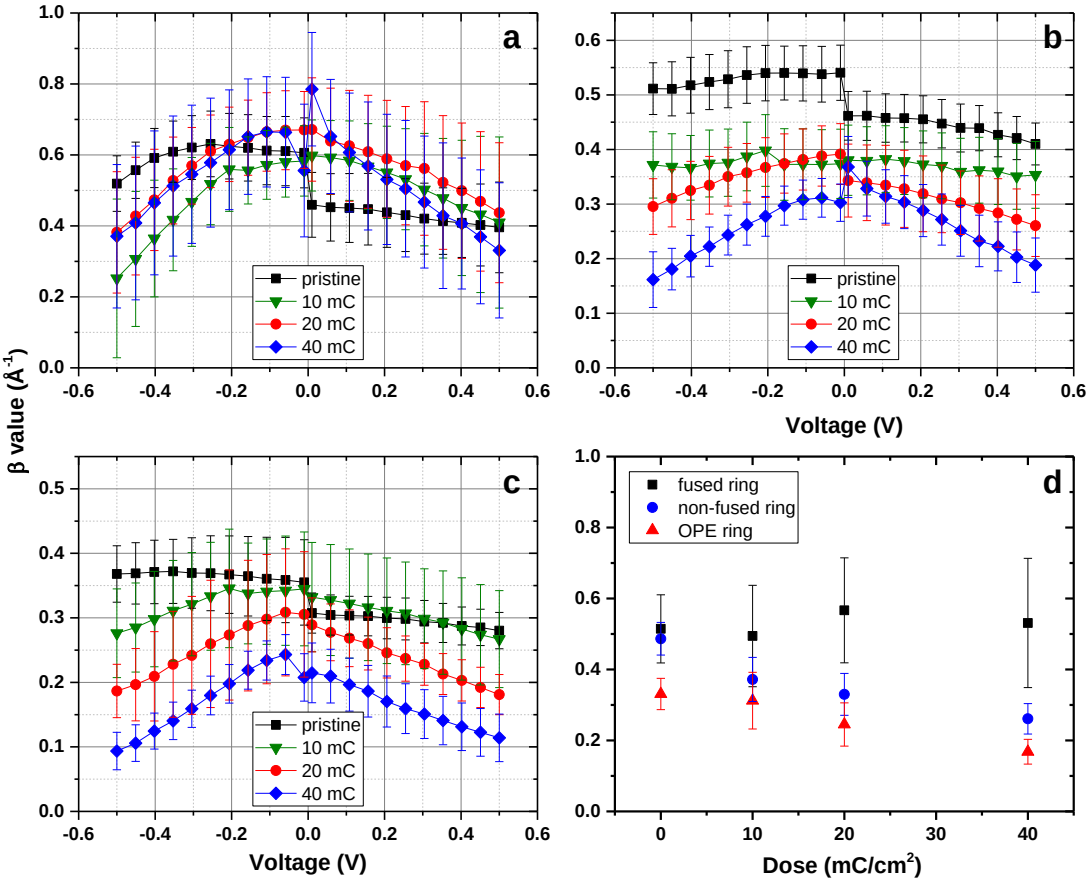

Figure 4.19: Plot of the tunneling decay constant (β) versus bias voltage of the pristine and the irradiated SAMs of acene (a), oligophenyl (b) and OPE (c) backbones. Average values of the β values versus irradiation dose are shown in panel (d).

Figure 4.19 shows the respective β values for each system in the bias range between -0.5 V and 0.5 V. The average of the estimated β values (Figure 4.19d) of the pristine SAMs are 0.52 Å^{-1}, 0.49 Å^{-1} and 0.33 Å^{-1} for fused, non-fused and OPE rings, respectively, which are in agreement with the values in literature. In the given case, for non-fused, fused and OPE rings the β values lay between 0.42-0.7 Å^{-1} [42, 52-55], ~0.5 Å^{-1} [46, 56] and 0.27-0.3 Å^{-1} [42, 51], respectively. The observed difference in β values of pristine SAMs (as shown in Figure 4.19, the β values at negative bias region are slightly bigger than the ones in the positive bias region) could be related to asymmetric tunneling path which was also mentioned for the SAMs of non-fused rings [38]. The

average of estimated β values for each system is plotted as a function of irradiation dose in Figure 4.19d. As can be seen in this figure, while the average β values for non-fused and OPE rings decrease continuously upon irradiation, and for the fused rings do not decrease.

It is obvious that the electric transport properties of the SAM films are changing upon irradiation. While tunneling decay constants of pristine samples seem to be not dependent on bias voltage, a huge impact of irradiation is clearly visible for β, which makes it dependent on bias voltage: The β values decrease with increasing bias voltage. The bias-dependent behavior is probably related to the tunneling barrier at the cross-linked SAM-substrate interface [38, 91]. In addition, the asymmetric behavior of the pristine β values with respect to bias voltage disappears, and a more symmetric behavior is observed upon irradiation.

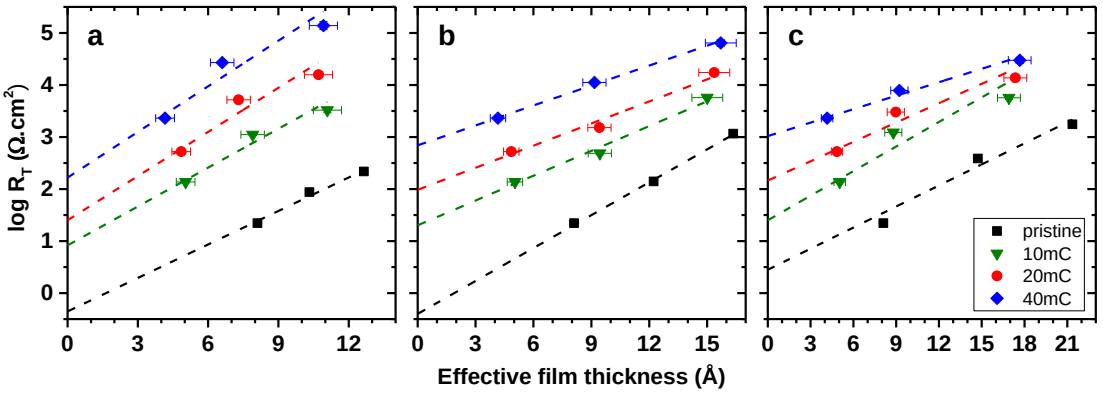

Figure 4.20: Semilog plot of average tunneling resistances versus effective film thickness for the pristine and irradiated SAMs of acene (a), oligophenyl (b) and OPE (c) backbones. Dashed lines represent the linear fits of the data points.

To have a closer look at the decrease in conductance of the SAMs studied, tunneling resistances (R_T) were studied. The R_T of the junctions based on the SAMs of acene, oligophenyl and OPE backbones, which are plotted against the molecular length in a logarithmic fashion at each irradiation dose, are presented in Figure 4.20. The resistance of all SAMs increases continuously upon irradiation which is understandable because it is inversely proportional to the conductance. However, an interesting observation arose from the intersect of each line in the resistance graphs, which corresponds to the contact resistance (R_0): An exponential increase in the contact resistances was observed for all systems, which were plotted as functions of irradiation dose in Figure 4.21. This exponential increase in the contact resistance was attributed to the enhanced tunneling

barrier, which altered the contact resistance of carbon nanotube based composite material from 2 to 10 orders of magnitude for the barrier heights varying from 1 to 5 eV [131]. Possible explanation for the increase in contact resistances could be given by the changes at the interfaces. (i) SAM-ambience interface: When irradiated SAMs are exposed to ambient atmosphere, adsorption of oxygen or airborne species on SAM films takes place [18], which can be observed with XPS analysis. The I-V measurements in this PhD project were carried out at ambient atmosphere, therefore, the adsorption of oxygen or airborne species on the irradiated SAM is possible to occur, and should give an additional resistance to the film. (ii) SAM-substrate interface: Upon irradiation, the thiolate bond (Au−S) intensity decreased continuously, which means the reduced chemical contact between SAM and substrate. Therefore, this change should also influence the resistance of the SAMs. (iii) Within SAM matrix: Each molecule in pristine SAMs forms a molecular tunnel for charge transport. However, as it was previously explained in Section 4.1 that electron irradiation results in lateral cross-linking of the aromatic molecules (forming a quasi-2D material) along with the decrease in the order in the monolayer, which should also modify the electronic structure.

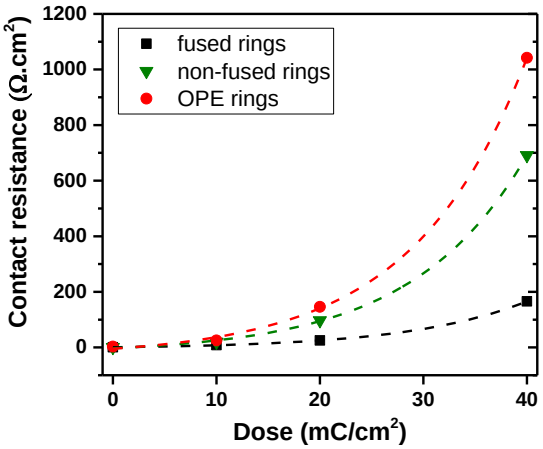

Figure 4.21: Plot of contact resistance as a function of irradiation dose for acene, oligophenyl and OPE backbones. The contact resistances of each backbone are fitted by exponential functions represented by dashed lines.

In addition, the barrier height of a material is known to be interrelated to the work function of the metals and semiconductors [132-134]. Therefore, a change in WF should affect the barrier height and thereby contact resistance. The study of Frisbie and his coworkers could be given as an example to this statement, which suggested that the contact resistance of junctions could be altered by changing the WF of SAMs and type

of chemical contacts [46]. They prepared SAMs on different substrates, and compared their contact resistances with respect to the WF change. They showed that contact resistance is strongly dependent on WF change (difference in WF between WF of pure metal and WF of SAM-covered metal) and increases with decreasing WF change [46]. Actually, they define the WF changes as the sum of three interfacial dipoles: the intrinsic molecular dipole, the intrinsic metal dipole that changes upon monolayer adsorption (i.e., the surface electron push-back effect) and the metal–linker (e.g., metal–S) bond dipole. As discussed in the previous sections, electron irradiation modifies the aromatic SAMs by forming a cross-linked network which should lead to a change in the intrinsic molecular and metal dipoles. Also, the broken Au−S bond and the formation of irradiation-induced sulfur species should contribute to the change in metal–linker bond dipole. According to these considerations there must be a change in WF, so that the contact resistance increases as a consequent to irradiation, and in order to prove this, the WF of pristine and irradiated samples was measured in situ under UHV conditions, which will be explained in the next section. The related WF changes are shown in Figure 4.24. Upon irradiation, all SAMs, except for PT, showed an increase in the WF between 0.1 and 0.26 meV, meaning that the WF of irradiated SAMs on gold came close to that of pure gold metal which was referenced to 5.2 eV. This expected increase could be one explanation for the increase in the contact resistance.

Another important parameter to carry information about the electronic structure of SAMs, viz. the position of the frontier orbitals and the width of the HOMO-LUMO gap, is the transition voltage (V_{trans}) at which point charge transport mechanism is changed from molecular tunneling into field emission [44]. Beebe et al [44] assumed that the electronic structure of metal-molecule-metal junctions has a rectangular tunneling barrier which is equal to the energy offset between Fermi level (E_F) of the metal and the closest molecular orbital (HOMO is accepted as the closest molecular level in aromatic SAMs). The length of the molecule in the junction is assumed to be the width of the tunneling barrier. Although the real barrier of the molecular junctions is much more complicated, it has been shown that this model clearly depicts the change in the current-voltage response, which is a transition from direct tunneling through a barrier (trapezoidal type) to field emission through the top of the barrier (triangular type) [44, 45]. The more detailed explanation of the model and the transition voltage are explained in the refs [44, 45, 92, 135].

According to the studies related to transition voltage of SAMs [44, 45, 56, 92, 135, 136], it could be said that V_{trans} is influenced by molecular length, WF and E_F-E_{HOMO} offset values. In addition, depending on the character of the backbone, the effect of molecular length could be different. While in aromatic SAMs V_{trans} decreases with increasing aromatic unit, for aliphatic SAMs V_{trans} values are independent from the molecular length [45]. This situation is attributed to the similar HOMO-LUMO gap of aliphatic SAMs and change in HOMO-LUMO gap of aromatic SAMs with respect to chain length [45]. The voltage corresponding to the minimum of the plot of ln (I/V^2) against 1/V (Fowler-Nordheim (F-N) plot), the transition voltage, provides direct information on the tunneling barrier height [44].

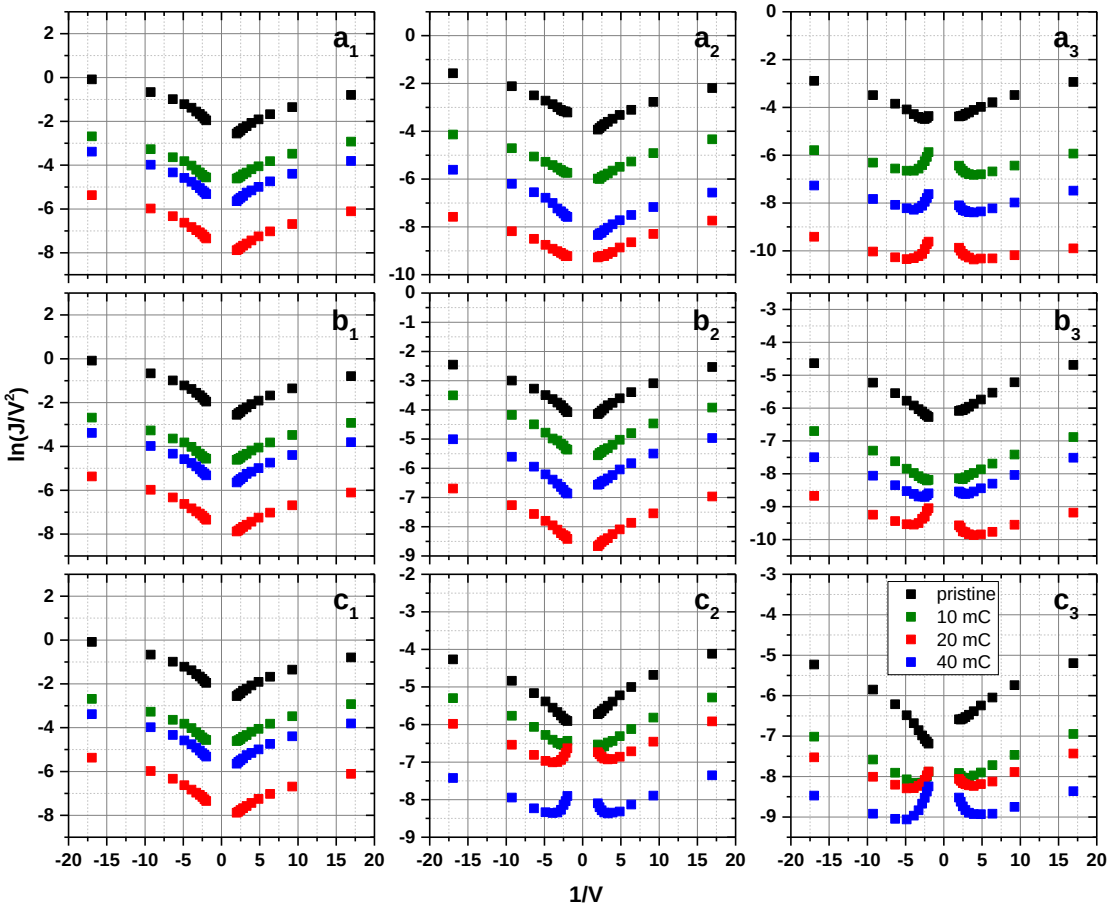

Figure 4.22: Fowler-Nordheim (F-N) plots for molecular junctions of pristine and irradiated SAMs from acene (a_1, a_2, a_3), oligophenyl (b_1, b_2, b_3), and OPE (c_1, c_2, c_3) backbones using PT (a_1, b_1, c_1) as the first member in each series assigned with subscript '1'.

F-N plots of all molecules are given in Figure 4.22. The V_{trans} of pristine SAMs was not possible to observe in the given bias voltage range except for AnthT (Figure 22a_3, in the negative voltage range) and OPE3 SAMs (Figure 22c_3, in the positive voltage

range). Actually, this observation is reasonable because the bias range is between -0.5 V and +0.5 V which is not sufficient to see the transition voltages of all molecules. Also, literature reports the V_{trans} values of these molecules (not observed) in the range of ~0.5–1 V [38, 44, 45], which is higher (or lower for negative bias) than my applied voltage limit. After irradiation, while V_{trans} of longer molecules (OPE2, AnthT, TPT and OPE3) started to appear in the bias range, there was not observed a transition for shorter molecules (PT, NphT and BPT), however, Penner et al observed the V_{trans} of BPT at around 0.25 V after 50 mC/cm^2 irradiation dose [38]. Here it should be stressed that there are discrepancies for the estimation of V_{trans} in literature, at least half of the measured current-voltage curves are discarded to get a reasonable value. In this study, all I-V curves obtained from the measurements were used in the results without discarding. Upon irradiation OPE2, AnthT, TPT and OPE3 SAMs showed a tendency to decrease their V_{trans} values (Figure 4.23). This decrease could be related to the broadening of the molecular orbitals [38] and the reduction in HOMO-LUMO gaps upon irradiation, which was observed for BPT [16] and terphenyldimethanethiol [128, 129] SAMs after irradiating them with e-beam. The estimated values for pristine AnthT and OPE3 SAMs are lower than the literature values measured by conductive AFM [45], which is presumably because of the difference in WF values between EGaIn and Au AFM tip which are $\Phi_{Au} \approx 5.3$ eV and $\Phi_{EGaIn} \approx 4.3$ eV, respectively [38]. Not observing a transition for the SAMs with low film thickness in the applied voltage range could be explained by: Since V_{trans} depends on the thickness of the aromatic SAM, the applied voltage range is not sufficient to see the V_{trans} values for the SAMs comprising of short molecules.

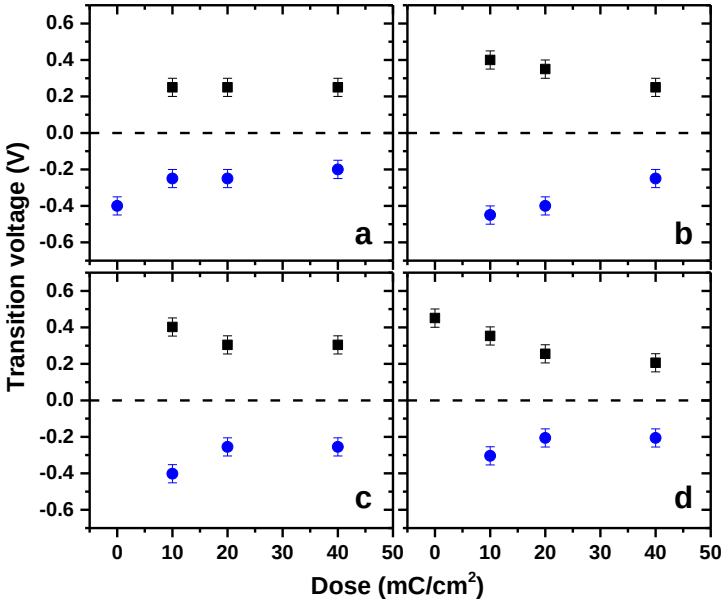

Figure 4.23: Transition voltage (V_{trans}) for both bias polarities versus irradiation dose for AnthT (a), TPT (b), OPE2 (c) and OPE3 (d) SAMs.

4.5 Work Function Experiments

The change in work function (WF) of the aromatic SAMs upon electron irradiation was monitored by the Kelvin Probe technique (see Section 3.9). The WF values for all series (acene, oligophenyl and OPE backbone) with respect to freshly sputtered gold, measured with a Kelvin probe are presented in Figure 4.24 and compiled in Table 4.3. The main purpose of this section is to monitor the variation in WF of aromatic SAMs upon electron irradiation, which is presented for the first time.

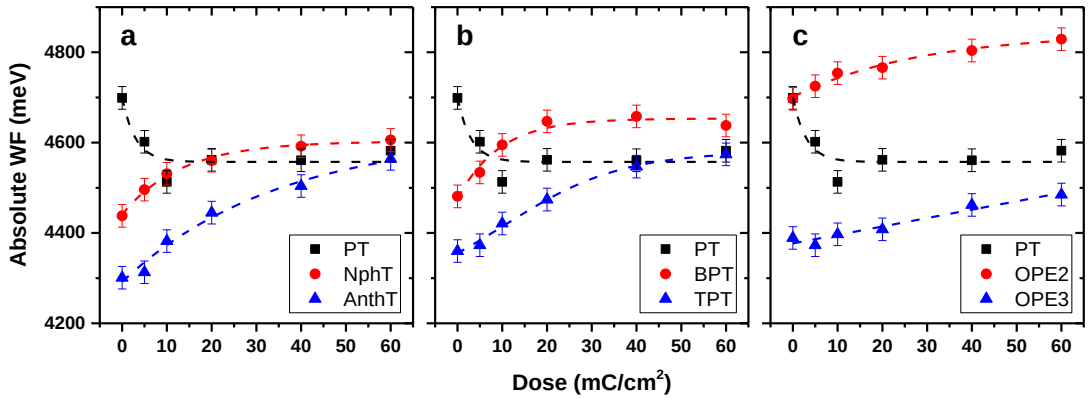

Figure 4.24: Change in the WF of the SAMs from acene (a), oligophenyl (b) and OPE (c) backbones as a function of irradiation dose.

The WF values for the pristine SAMs of acene backbone are in accordance with the literature [56], where the WF values were obtained from ultraviolet photoelectron spectroscopy measurements. As seen from Figure 4.24, there is a clear effect of electron irradiation on the WF of SAMs from all backbone types; WF of all SAMs moved upward while only PT SAM film exhibited a movement to downward. AnthT SAM has the highest variation in WF with the value of ~0.26 eV, and OPE3 SAM has the lowest change with only 0.1 eV. In general, the acene backbone has the highest variation. If it is considered that the effect of electron irradiation at the SAM-ambience and at the SAM-substrate interface (cleavage of Au−S bond) are similar for each backbone type, the change in the SAM matrix (cross-linking of the monolayer and loss of order in the monolayer) should have major role for the differences in the WF change.

Table 4.3: WF values of pristine and irradiated SAMs. The units are eV.

Irradiation dose	PT	NphT	AnthT	BPT	TPT	OPE2	OPE3
Pristine	4.7	4.44	4.3	4.48	4.36	4.7	4.39
5	4.6	4.5	4.31	4.53	4.37	4.73	4.37
10	4.5	4.53	4.38	4.6	4.42	4.75	4.4
20	4.56	4.56	4.45	4.65	4.47	4.77	4.41
40	4.56	4.59	4.5	4.66	4.55	4.8	4.46
60	4.58	4.61	4.56	4.64	4.57	4.83	4.49

When one looks to Figure 4.24, it is clear that the WF values of acene and oligophenyl SAMs are ordered with the molecule length of their constituents, however, OPE2 SAM deforms this order for the OPE backbone. The absolute WF value of pristine OPE2 is somewhat higher than expected, which should be related to its film properties such as low packing density (see Table 4.2) and/or large tilt angle with respect to the surface normal in comparison to other SAM films. The effect of the latter was mentioned for alkanethiol SAMs on gold and silver substrates [137]. According to XPS thickness value of pristine OPE2 SAM, it corresponds to ~70% of the monolayer if it forms an all trans extended upright orientation. Therefore, this could be explained either by the

low packing density and/or by large tilt angle of OPE2 SAMs. However, its general response to the irradiation, increasing with irradiation dose, is same like other SAMs.

The results obtained in this section confirm the importance of the backbone type, which has already been discussed by XPS analysis and electric transport experiments, and show that electron irradiation can be a useful tool tune the WF of surfaces covered with organic layers like SAMs.

4.6 Nitrogen-Containing Aromatic SAMs

As an additional system, I also investigated the effect of electron irradiation on pyridine-containing aromatic SAMs (see the figure below) with XPS. Therefore, I followed the same procedure as described for the non-substituted aromatic molecules in Section 4.1.

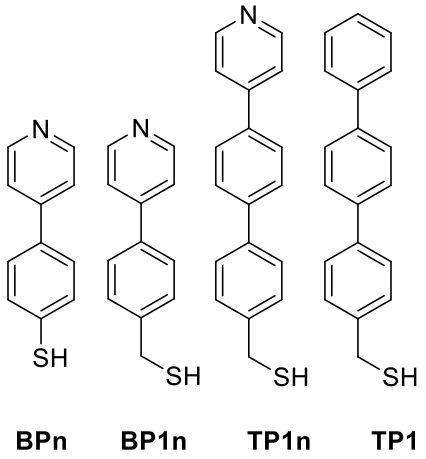

This is the same figure as shown in Chapter 3 (Figure 3.2).

The fabricated BPn, BP1n, TP1n and TP1 SAMs exhibited a similar behavior upon electron irradiation. C 1s, S 2p and N 1s XPS spectra of the pristine and irradiated TP1n SAM are presented in Figure 4.25, representative of the BPn, BP1n and TP1 monolayers as well. The irradiation was performed homogeneously over the sample, the electron energy was set to 50 eV, and the dose was varied.

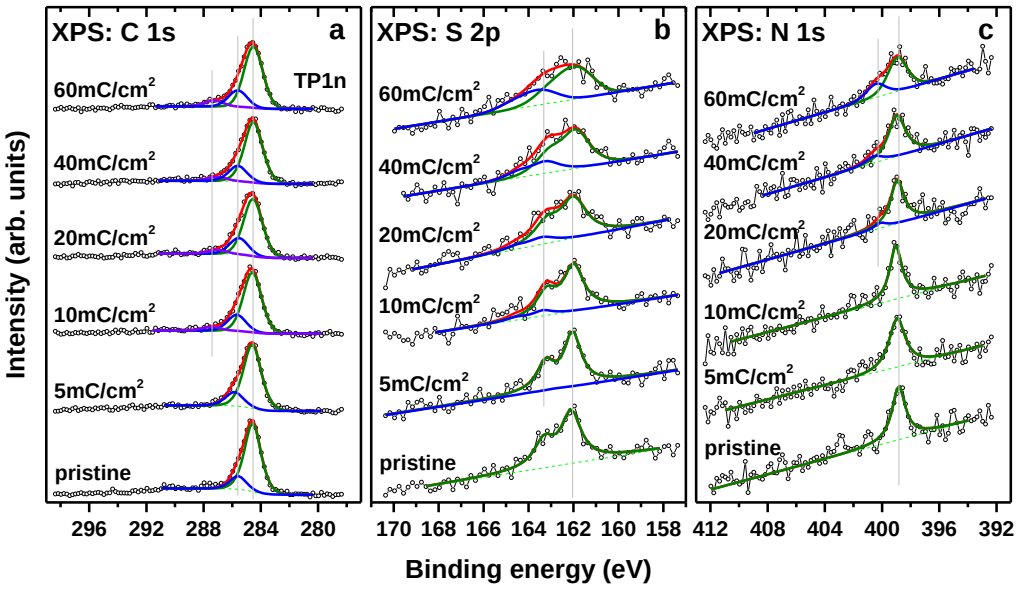

Figure 4.25: C 1s (a), S 2p (b) and N 1s (c) XPS spectra of the pristine and irradiated TP1n SAMs. The doses are marked at the respective spectra. The energy of the electrons was 50 eV. The C 1s spectra are decomposed into the component peaks, viz. the main peak (green lines) and a shoulder (blue lines); see text for details. The S 2p spectra are decomposed into the component doublets corresponding to the pristine thiolate species (green lines) and irradiation-induced sulfur species (blue lines); the sum of these components is drawn by the red lines. Vertical solid lines in panel (b) highlight the BE positions of the doublets.

The C 1s spectra of the pristine TP1n SAM in Figure 4.25a exhibits a strong peak at 284.5 eV corresponding to the oligophenyl backbone [113, 114] and a shoulder around 285.5 eV, assigned to the carbon atom bonded to the nitrogen. The position of C 1s signal is consistent with the XPS spectra of the TP1n SAM used in ref [115]. No features corresponding to possible oxygen contamination are observed, which was also supported by the O 1s spectrum (not shown). The intensity of the C 1s peaks as well as the character and shape of the C 1s spectrum of the TP1n SAM do not exhibit any perceptible changes upon irradiation. This suggests, in agreement with the Au 4f data (not shown here), a very low extent (if any at all) of irradiation-induced desorption, which is also supported by the behavior of the effective thickness. The respective dependence of this parameter for the BPn, BP1n, TP1n and TP1 SAMs on irradiation dose is shown in Figure 4.26a. Accordingly, the effective thickness almost did not change in the course of the irradiation but for TP1n SAM increased slightly. The thickness increase is presumably related to the irradiation-induced adsorption of residual gas molecules on the SAM surface, which was observed in AnthT, TPT and OPE3 SAMs and mentioned in Section 4.1.

Table 4.4: XPS thickness, area per molecule and packing density of the pristine pyridine-containing SAMs and TP1 SAM used in this section. The values were determined from the XPS spectra of the SAMs.

Molecules	XPS thickness (Å)	Area per molecule (Å^2/molecule)	Packing density (molecules/cm^2)
BPn	11.6±0.4	25.5	3.92×10^{14}
BP1n	12.6±0.4	24.7	4.05×10^{14}
TP1n	18±0.6	21.3	4.70×10^{14}
TP1	16.6±0.6	23.1	4.33×10^{14}

The lack of any perceptible changes in the C 1s spectra upon the irradiation can lead to a wrong conclusion that no chemical changes in the SAM matrix occur. This is, however, not the case as follows from a detailed analysis of these spectra. The derived parameter, viz. the FWHM of the main C 1s peak for the BPn, BP1n, TP1n and TP1 SAMs is shown in Figure 4.26b as functions of the irradiation dose. As seen in this figure, the FWHM values exhibited small but well-traceable changes upon the irradiation, with a saturation-like behavior achieved already at ~20 mC/cm^2. These changes can be associated with progressive cross-linking of the SAM constituents, following the extensive cleavage of C–H bonds in the SAM matrix. The threshold for such processes lies at ~7 eV [11, 17], far below the electron energies in this work.

The FWHMs of the main C 1s peak for the SAMs studied exhibit an exponential-like variation at low doses and a leveling off behavior at high doses. Such a behavior is typical for SAMs [15] and can be described by using Eq. 4.1 described for the same processes in Section 4.1. The respective fitting curves are shown in Figure 4.26b, and the derived cross-sections, from the C 1s FWHM behavior, are compiled in Table 4.5. The cross-section value of BPn film is ~1.3 times higher than that of BP1n film, indicating the change in the hydrocarbon matrix is more pronounced than the BP1n one. This is an expected result, because the presence of the methylene unit (-CH_2-) between the sulfur headgroup and aromatic chain provides the formation of a more densely packed and ordered monolayer. Actually, odd numbers (1, 3, 5) of the methylene units provide higher order and packing density to the monolayer than even numbers (0, 2, 4, 6) [138-145]. Moreover, this is also supported with the packing densities of BPn and BP1n SAMs compiled in Table 4.4. A similar behavior was observed for TP1n and TP1 SAMs both of which have the identical structure except for the nitrogen in the top

ring. The TP1n monolayer has a cross-section value of 3.1×10^{-17} cm^2 which one is 1.5 times more than TP1 SAM. Therefore, from the comparison of the cross-sections it can be claimed that the nitrogen in the aromatic ring leads the TP1n SAM to be more impaired under electron irradiation in comparison to the TP1 SAM. Furthermore, the huge effect of methylene spacer is obvious when the cross-sections of the TPT SAM (see Section 4.1), whose backbone is identical to TP1 but without a methylene spacer, and TP1 SAMs are compared to each other. For three-ring system (TPT and TP1 SAMs), the cross-section of the TPT SAM is ~1.8 times more than TP1, indicating the loss of order in the monolayer more noticeable than TP1 monolayer as mentioned above for BPn and BP1n SAMs.

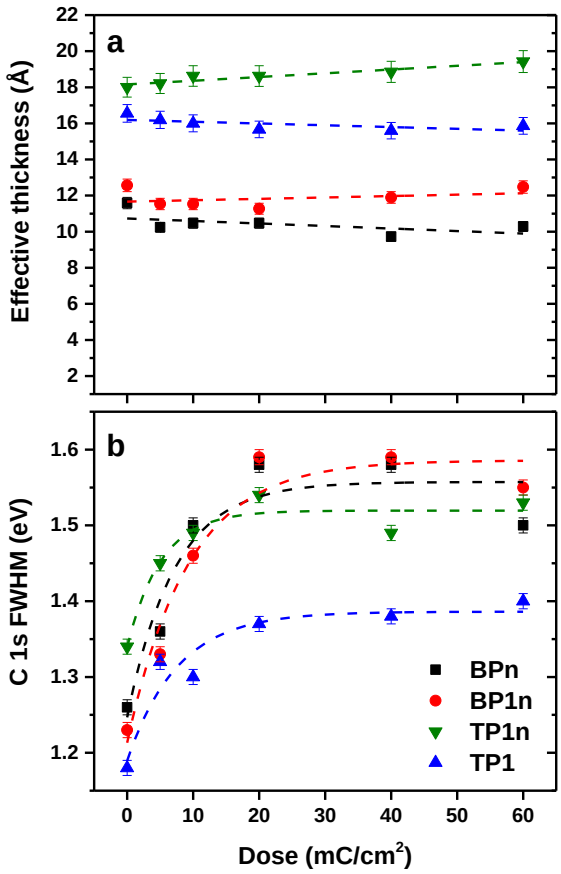

Figure 4.26: Dependence of the effective thickness (a) and FWHM of the main C 1s peak (b), for the BPn (black squares and black dashed curve), BP1n (red cicles and red dashed curve), TP1n (green down triangles and green dashed curve), and TP1 (blue up triangles and blue dashed curve) SAMs on irradiation dose. The straight, color-coded dashed lines in panel (a) are guides for the eyes. The parameters in panel (b) are fitted by exponential functions according to Eq. 4.1 (color-coded dashed curves).

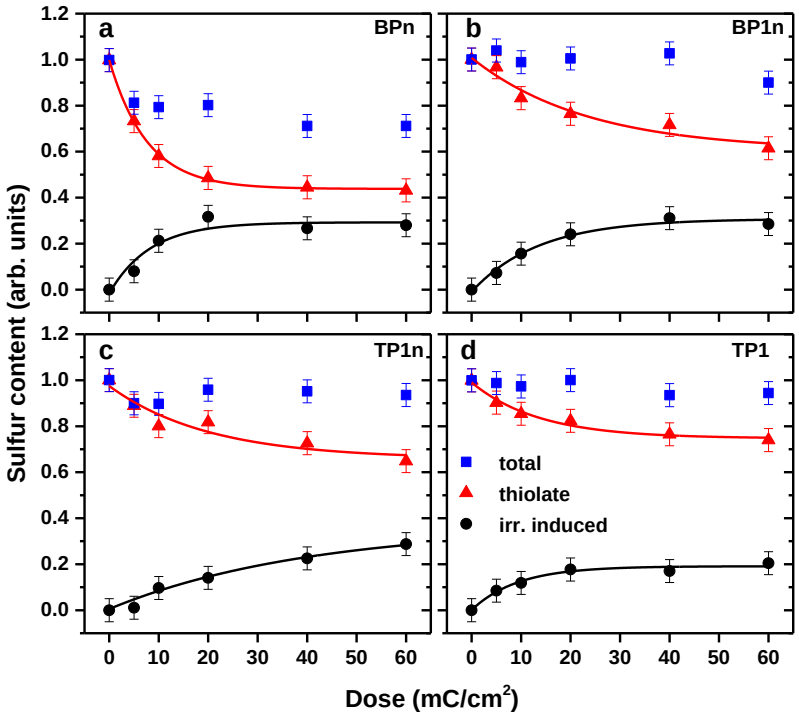

Figure 4.27: Dependence of the total intensity of the S 2p signal (blue squares), intensity of the S 2p component corresponding to the pristine thiolate species (red triangles), and intensity of the S 2p component corresponding to irradiation-induced species (black circles) for the BPn (a), BP1n (b), TP1n (c), and TP1 (d) SAMs on irradiation dose. The intensities of the above components are fitted by exponential functions according to Eq. 4.1 (red and black solid lines, respectively).

Along with the SAM matrix, the SAM-substrate interface was modified upon the electron irradiation as follows from the S 2p XPS spectra of the TP1n SAM shown in Figure 25b, representative of the BPn, BP1n and TP1 monolayers as well (similar behavior). The spectrum of the pristine TP1n SAM exhibits a characteristic S $2p_{3/2,1/2}$ doublet at a BE position of ~162.0 eV (S $2p_{3/2}$) corresponding to the thiolate species bound to noble metal surfaces [113, 146], with no traces of atomic sulfur, disulfide, unbound sulfur or oxidized species. Upon the irradiation, another component doublet at a BE position of ~163.4 eV (S $2p_{3/2}$) appears and progressively increases in intensity with increasing dose on the expense of the thiolate-stemming doublet. This behavior corresponds to the irradiation-induced cleavage of the Au–S bonds and appearance of new species, which can be disulfides but most likely have C–S–C character [10, 16]. The intensities of both S 2p component doublets as well as the total intensity of the S 2p signal for the BPn (a), BP1n (b), TP1n (c) and TP1 (d) SAMs are presented in Figure 4.27 as functions of the irradiation dose. Except for BPn film (see Figure 4.27a), the total S 2p intensity changed hardly in the course of the irradiation which, along with

the Au 4f (not shown) and C 1s XPS data, suggests a very low extent of the irradiation-induced desorption in the SAMs studied. The decrease in the sulfur content of BPn SAM was attributed to the less packing density of the monolayer. At the same time, the intensities of the doublets, corresponding to the thiolate and irradiation-induced species, exhibit an exponential-like variation at low doses and a leveling off behavior at high doses. Using same approach as in the case of the C 1s spectra, fitting according to Eq. 4.1 could be performed. The respective fitting curves are shown in Figure 4.27, and the derived cross-sections are compiled in Table 4.5, averaged over the curves describing the intensities of S 2p component doublets corresponding to the thiolate and irradiation-induced species. These cross-sections are quite similar for the SAMs studied, with the highest value for the BPn SAM and the lowest value for the TP1n monolayer.

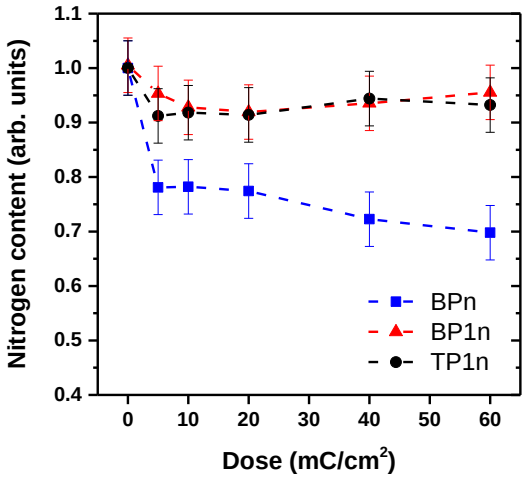

Figure 4.28: N 1s intensity of BPn, BP1n and TP1n SAMs as a function of irradiation dose.

Apart from the changes at the SAM-substrate and within the SAM matrix, a change at the SAM-ambience interface also took place upon electron irradiation. The effect of electron irradiation was monitored by the variation in intensity of nitrogen which is located at the topmost outer position (SAM-ambience interface) of the SAM. The respective N 1s XPS spectra are shown in Figure 4.25c, representative of the BPn and BP1n monolayers as well. The spectrum of the pristine TP1n film shows a peak at a BE position of ~399 eV corresponding to the nitrogen in the pyridine ring [115, 147]. The total intensity of N 1s signal for BPn, BP1n and TP1n is plotted as a function of irradiation dose and is presented in Figure 4.28. Upon the irradiation, the intensity of the N 1s signal decreased slightly by about 5-8%, which suggests a very low extent of desorption in the SAM, along with C 1s and S 2p signals. However, for BPn SAM the

decrease in N 1s intensity is more noticeable as in the case for C 1s and S 2p signals of BPn monolayer, indicating the desorption of molecular fragments from the SAM film, therefore, the BPn SAM was found to be the least stable film. Moreover, after irradiating TP1n SAM with a 20 mC/cm^2 dose, a shoulder at 400.5 eV, attributed to the irradiation-induced nitrogen species, was observed in intensity with increasing dose.

Table 4.5: Cross-sections of the irradiation-induced processes involving the SAM matrix and the SAM/substrate interface; see text for details. The values were determined from the spectroscopic experiments. The units are 10^{-17} cm^2.

Monolayer	BPn	BP1n	TP1n	TP1
SAM matrix	2.2±1	1.7±0.6	3.1±1.1	2.1±0.9
SAM/Au interface	2±0.4	0.94±0.3	0.6±0.3	1.4±0.3

5 Conclusions

In this work, I focused on the effect of electron irradiation on aromatic thiolate SAMs on noble metal substrates. Accordingly, I studied the evolution of the basic irradiation-induced processes in the course of the irradiation treatment as well as performance of these films as negative resists in electron lithography. In addition, the changes in the electric transport properties and work function were monitored. The most basic aromatic systems, with rod-like oligophenyl, acene and OPE backbones, were addressed, with the length of the backbone being varied and with the OPE-based films being investigated for the first time in the given context. All the SAMs studied exhibited similar behavior upon the irradiation treatment, with clear dominance of cross-linking, following the cleavage of C–H bonds in the SAM matrix and slowing down and inhibiting damage of the SAM-substrate interface and desorption of molecular fragments. The cross-sections for the modification of the SAM matrix and the damage of the SAM-substrate interface were determined for the primary electron energy of 50 eV, frequently used for the CNM fabrication. The derived values were found to be similar for a particular process, showing only slight difference for the different backbones.

It was found that the effect of cross-linking takes hold of the systems at already very early stages of the treatment, affecting the other, irradiation-induced processes and ensuring performance of the films as negative lithographic resist. The two-ring systems (BPT, NphT and OPE2) exhibited the best performance as lithographic resists, with an optimal dose of 10-20 mC/cm^2 at 0.5-1 keV. The one-ring system (PT) showed a poor performance, which was explained by its limited ability to form an extensive, 2D cross-linking network. The three-ring systems (TPT, AnthT and OPE3) exhibited a poor lithographic performance, because of the high resistance of the pristine films to the etching agents, resulting in a low etching contrast between the irradiated and non-irradiated areas. Another process associated with the poor lithographic performance of the three-ring films, but occurring at high doses for the two-ring films as well, was a spontaneous release of the cross-linked SAMs within the irradiated areas, in the form

of CNMs. This process resulted either in spot-perimeter-decoration patterns or even in reversal of the lithographic contrast.

From the lithographic data, cross-sections of the irradiation-induced cross-linking were derived for all SAMs studied. These cross-sections decreased with increasing electron energy in the energy range of the lithographic experiments (0.5-5 keV). For the AnthT film, where the data for 50 eV were obtained as well, the dependence of the cross-section on the electron energy exhibited a bell-like curve with a maximum at 500 eV, mimicking the behavior of the secondary electron yield from the gold substrate.

For all types of the SAM precursors except for PT, fabrication of CNMs was demonstrated, reproducing the literature data [35] for the films with the oligophenyl and acene backbones and getting this result for the first time for the monolayers with the OPE backbone.

The changes in the electric transport properties of the aromatic SAMs upon electron irradiation (50 eV) were monitored by two-terminal junction method using an EGaIn tip as the top electrode and the conductive Au substrate as the bottom electrode. The obtained current density values correlated well with the lengths of the pristine SAMs, confirming the general formula $J = J_0 \exp(-\beta d)$ used to describe the conductance of monomolecular films. The estimated tunneling decay constants (β) for the pristine SAMs were in good agreement with the literature values. At the same time, upon irradiation, the β values decreased for all SAMs except for those with the acene backbone, and became somewhat dependent on the bias voltage, which is probably related to the tunneling barrier at the SAM-gold interface [38].

Upon varying the irradiation dose from 10 to 40 mC/cm^2, a decrease in electrical conductance by 1 order and 1-2 orders of magnitude was observed for the OPE and oligophenyl SAM films, respectively. In the case of the acene backbone, this effect was even more pronounced (a decrease by 2-3 orders of magnitude), which was attributed to the destruction of the highly-conjugated ring structure of these films. The decrease in electrical conductance meant an increase in the tunneling resistance of the molecular junctions, which occurred mostly on the expense of the contact resistance. The latter parameter increased exponentially upon irradiation for all monolayers studied. This behavior was attributed to (i) the modification of the electronic structure (positions of the frontier orbitals and the width of the HOMO-LUMO gap), (ii) change of WF, (iii) adsorption of oxygen or airborne species at the SAM-ambience interface upon exposure

of the irradiated films to ambient and (iv) partial breakage of Au–S bonds at the SAM-substrate interface.

To get information on the behavior of the relevant parameters, changes in the electronic structure and WF of the SAMs upon the irradiation were monitored by the Kelvin probe technique. The observed increase in WF (between 0.1 and 0.26 eV) for the most of the systems correlated well with the increase in the contact resistance. The electronic structure was studied indirectly by compiling the Fowler-Nordheim (F-N) plots. These plots exhibited non-resonant (direct) tunneling for all SAMs and transition to the field emission regime for the three-ring and OPE2 monolayers. Not observing such a transition for shorter molecules was attributed to the limited bias voltage range (V_{trans}) so that the F-N tunneling regime could not be achieved. The respective transition voltage V_{trans} was derived, which is believed to be a fingerprint for the positions of the frontier molecular orbitals [92, 93]. The V_{trans} values became smaller upon the irradiation, indicating a progressive decrease in the HOMO-LUMO gap.

The changes in the WF in all systems were monitored by the Kelvin probe technique. All SAMs studied exhibited similar behavior, showing an increase in the WF by 0.1-0.26 eV upon the irradiation treatment, except for the one-ring system (PT) which showed a decrease by ca. 0.15 eV. The increase in WF for the most of the monolayers correlated with the increase in the contact resistances. In particular, the SAMs with the acene backbone exhibited the highest WF change, corresponding to the highest change in the electrical conductance.

Apart from the non-substituted aromatic SAMs, pyridine-substituted monolayers with oligophenyl backbone were also studied. All these SAMs exhibited similar behavior as the nitrogen-free systems. The cross-sections for the modification of the SAM matrix and the damage of the SAM-substrate interface were determined for the primary electron energy of 50 eV. The derived values were found to be similar for the SAMs studied, showing only slight difference for the two-ring (BPn and BP1n) and three-ring (TP1n and TP1) films. In addition, the total nitrogen intensity was found to decrease only slightly under the electron irradiation treatment which can be useful to fabricate nitrogen-doped CNMs and graphene sheets. At high doses (above 40 mC/cm^2 dose), the formation of irradiation-induced nitrogen species was observed.

Appendix

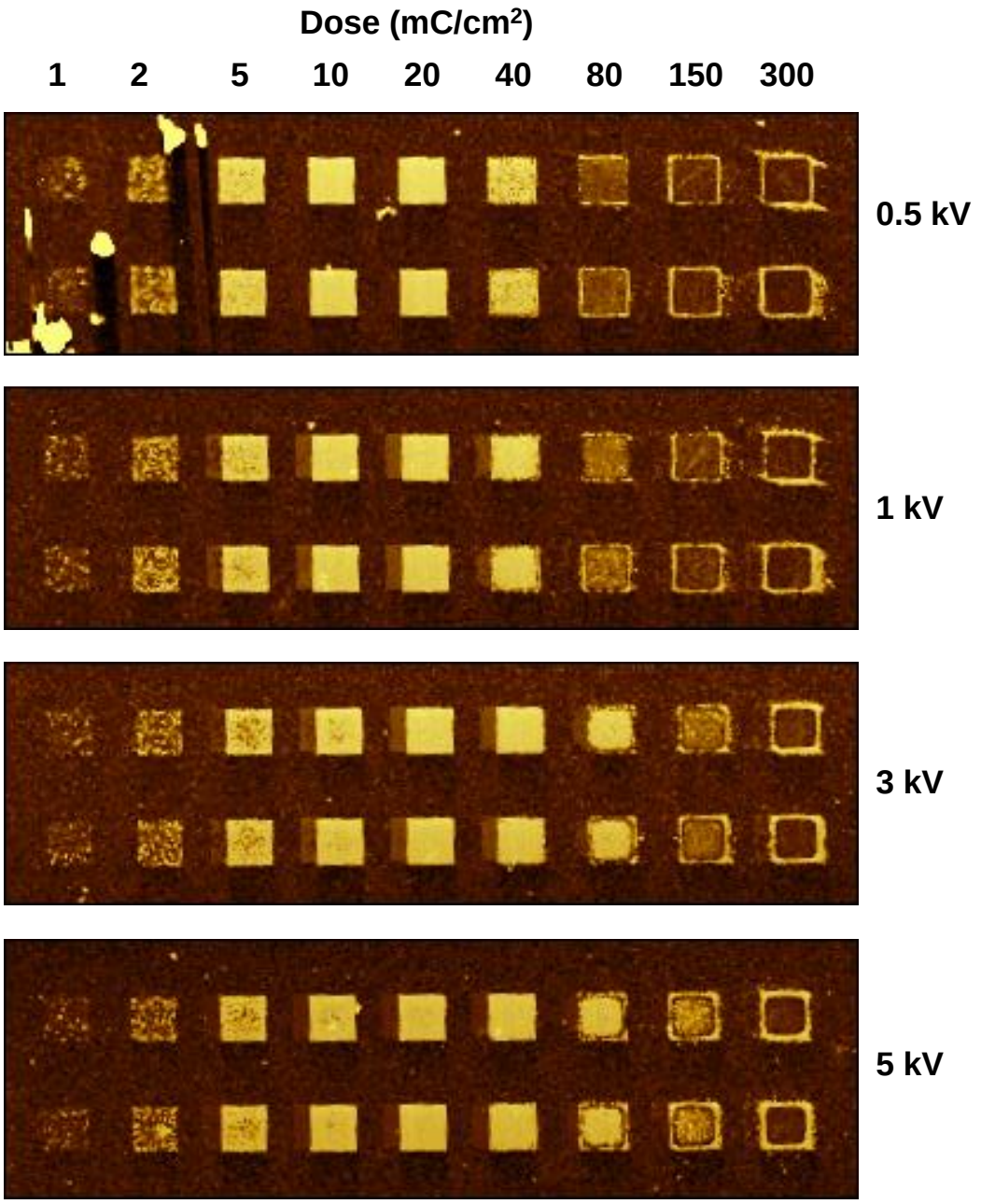

Figure A. 1: AFM images of Au/Si(100) patterns prepared by EBL with the NphT SAM. The patterning was performed at electron energies of 0.5, 1, 3 and 5 keV. The doses corresponding to the individual square-like Au features were 1, 2, 5, 10, 20, 40, 80, 150 and 300 mC/cm^2 (from left to the right).

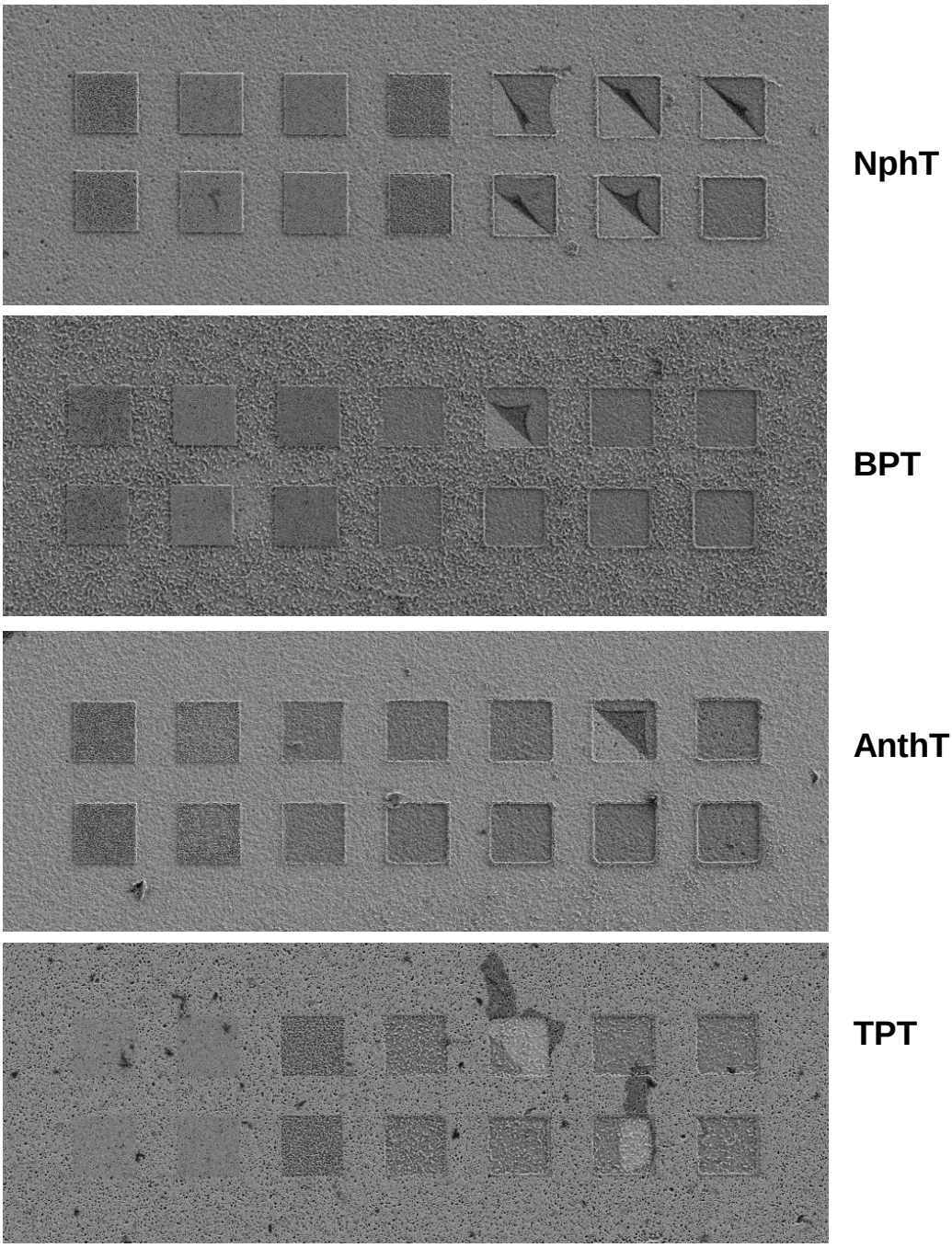

Figure A. 2: Spontaneous release of the cross-linked SAM pieces within the irradiated areas during the wet etching process, in the form of CNMs.

List of Figures

List of Tables

List of Scientific Contributions

Publications

1. Partes, C.; Yildirim, C; Schuster, S; Kind, M.; Zharnikov, M.; Terfort, A., *Self-Assembled Monolayers of Pseudo-C2v-Symmetric, Low-Band-Gap Areneoxazolethiolates on Gold Surfaces.* Langmuir, 2016. **32**(44): p. 11474-11484.
2. Yildirim, C; Kind, M.; Terfort, A; Zharnikov, M., *Modification of Aromatic Self-Assembled Monolayers by Electron Irradiation: Basic Processes and Related Applications.* Submitted to J. Phys. Chem. C.
3. Yildirim, C; Kind, M.; Terfort, A; Zharnikov, M., *Change in static conductance of aromatic self-assembled monolayers upon electron irradiation.* in preparation.
4. Sauter, E.; Yildirim, C; Kind, M.; Terfort, A; Zharnikov, M., *Work function tuning by electron irradiation of aromatic self-assembled monolayers.* in preparation.

Conference contribution

1. Sauter, E., Yildirim, C; Kind, M.; Terfort, A; Zharnikov, M., *Work function tuning by electron irradiation of aromatic self-assembled monolayers*, DPG Spring Meeting, March 2017, Dresden, Germany.

Bibliography

1. Love, J.C., et al., *Self-assembled monolayers of thiolates on metals as a form of nanotechnology.* Chem. Rev., 2005. **105**(4): p. 1103-1169.
2. Meyerbroker, N. and M. Zharnikov, *Modification of Nitrile-Terminated Biphenylthiol Self-Assembled Monolayers by Electron Irradiation and Related Applications.* Langmuir, 2012. **28**(25): p. 9583-9592.
3. Schreiber, F., *Structure and growth of self-assembling monolayers.* Prog. Surf. Sci., 2000. **65**(5-8): p. 151-256.
4. Ulman, A., *Formation and structure of self-assembled monolayers.* Chem. Rev., 1996. **96**(4): p. 1533-1554.
5. Hutt, D.A., E. Cooper, and G.J. Leggett, *Structure and mechanism of photooxidation of self-assembled monolayers of alkylthiols on silver studied by XPS and static SIMS.* J. Phys. Chem. B, 1998. **102**(1): p. 174-184.
6. Rieley, H., et al., *X-ray studies of self-assembled monolayers on coinage metals. 1. Alignment and photooxidation in 1,8-octanedithiol and 1-octanethiol on Au.* Langmuir, 1998. **14**(18): p. 5147-5153.
7. Jeyachandran, Y.L., et al., *Application of Long Wavelength Ultraviolet Radiation for Modification and Patterning of Protein-Repelling Monolayers.* J. Phys. Chem. C, 2013. **117**(11): p. 5824-5830.
8. Turchanin, A., et al., *Fabrication of molecular nanotemplates in self-assembled monolayers by extreme-ultraviolet-induced chemical lithography.* Small, 2007. **3**(12): p. 2114-2119.
9. Laibinis, P.E., et al., *X-Ray-Damage to Cf3co2-Terminated Organic Monolayers on Si/Au - Principal Effect of Electrons.* Science, 1991. **254**(5034): p. 981-983.
10. Heister, K., et al., *Characterization of X-ray induced damage in alkanethiolate monolayers by high-resolution photoelectron spectroscopy.* Langmuir, 2001. **17**(1): p. 8-11.
11. Olsen, C. and P.A. Rowntree, *Bond-selective dissociation of alkanethiol based self-assembled monolayers absorbed on gold substrates, using low-energy electron beams.* J. Chem. Phys., 1998. **108**(9): p. 3750-3764.
12. Geyer, W., et al., *Electron-induced crosslinking of aromatic self-assembled monolayers: Negative resists for nanolithography.* Appl. Phys. Lett., 1999. **75**(16): p. 2401-2403.
13. Frey, S., et al., *Response of biphenyl-substituted alkanethiol self-assembled monolayers to electron irradiation: Damage suppression and odd-even effects.* Langmuir, 2002. **18**(8): p. 3142-3150.

14. Zharnikov, M., et al., *Modification of alkanethiolate monolayers by low energy electron irradiation: Dependence on the substrate material and on the length and isotopic composition of the alkyl chains.* Langmuir, 2000. **16**(6): p. 2697-2705.

15. Zharnikov, M. and M. Grunze, *Modification of thiol-derived self-assembling monolayers by electron and x-ray irradiation: Scientific and lithographic aspects.* J. Vac. Sci. Technol. B, 2002. **20**(5): p. 1793-1807.

16. Turchanin, A., et al., *Molecular Mechanisms of Electron-Induced Cross-Linking in Aromatic SAMs.* Langmuir, 2009. **25**(13): p. 7342-7352.

17. Huels, M.A., P.C. Dugal, and L. Sanche, *Degradation of functionalized alkanethiolate monolayers by 0-18 eV electrons.* J. Chem. Phys., 2003. **118**(24): p. 11168-11178.

18. Chen, C.H., et al., *Exposure of monomolecular lithographic patterns to ambient: An X-ray photoemission spectromicroscopy study.* J. Phys. Chem. B, 2006. **110**(36): p. 17878-17883.

19. Eck, W., et al., *Generation of surface amino groups on aromatic self-assembled monolayers by low energy electron beams - A first step towards chemical lithography.* Adv. Mat., 2000. **12**(11): p. 805-808.

20. Zharnikov, M., et al., *Modification of alkanethiolate monolayers on Au-substrate by low energy electron irradiation: Alkyl chains and the S/Au interface.* Phys. Chem. Chem. Phys., 1999. **1**(13): p. 3163-3171.

21. Hamoudi, H., et al., *Chain-Length-Dependent Branching of Irradiation-Induced Processes in Alkanethiolate Self-Assembled Monolayers.* J. Phys. Chem. C, 2011. **115**(2): p. 534-541.

22. Amiaud, L., et al., *Low-energy electron induced resonant loss of aromaticity: consequences on cross-linking in terphenylthiol SAMs.* Phys. Chem. Chem. Phys., 2014. **16**(3): p. 1050-1059.

23. Houplin, J., et al., *A combined DFT/HREELS study of the vibrational modes of terphenylthiol SAMs.* Eur. Phys. J. D, 2015. **69**(9).

24. Houplin, J., et al., *Electron Processing at 50 eV of Terphenylthiol Self-Assembled Monolayers: Contributions of Primary and Secondary Electrons.* Langmuir, 2015. **31**(50): p. 13528-13534.

25. Zharnikov, M., et al., *X-ray absorption spectromicroscopy studies for the development of lithography with a monomolecular resist.* J. Phys. Chem. B, 2005. **109**(11): p. 5168-5174.

26. Tai, Y., et al., *Depth distribution of irradiation-induced cross-linking in aromatic self-assembled monolayers.* Langmuir, 2004. **20**(17): p. 7166-7170.

27. Tai, Y., et al., *Effect of irradiation dose in making an insulator from a self-assembled monolayer.* J. Phys. Chem. B, 2005. **109**(41): p. 19411-19415.

28. Eck, W., et al., *Freestanding nanosheets from crosslinked biphenyl self-assembled monolayers.* Adv. Mat., 2005. **17**(21): p. 2583-2587.

29. Schnietz, M., et al., *Chemically Functionalized Carbon Nanosieves with 1-nm Thickness.* Small, 2009. **5**(23): p. 2651-2655.

30. Turchanin, A., et al., *One Nanometer Thin Carbon Nanosheets with Tunable Conductivity and Stiffness.* Adv. Mat., 2009. **21**(12): p. 1233-1237.

31. Zheng, Z., et al., *Janus Nanomembranes: A Generic Platform for Chemistry in Two Dimensions.* Angew. Chem. Int. Ed., 2010. **49**(45): p. 8493-8497.

32. Nottbohm, C.T., et al., *Mechanically Stacked 1-nm-Thick Carbon Nanosheets: Ultrathin Layered Materials with Tunable Optical, Chemical, and Electrical Properties.* Small, 2011. **7**(7): p. 874-883.

33. Rhinow, D., et al., *Energy-filtered transmission electron microscopy of biological samples on highly transparent carbon nanomembranes.* Ultramicroscopy, 2011. **111**(5): p. 342-349.

34. Turchanin, A., et al., *Conversion of Self-Assembled Monolayers into Nanocrystalline Graphene: Structure and Electric Transport.* ACS Nano, 2011. **5**(5): p. 3896-3904.

35. Angelova, P., et al., *A Universal Scheme to Convert Aromatic Molecular Monolayers into Functional Carbon Nanomembranes.* ACS Nano, 2013. **7**(8): p. 6489-6497.

36. Zhang, X.H., et al., *Tailoring the Mechanics of Ultrathin Carbon Nanomembranes by Molecular Design.* Langmuir, 2014. **30**(27): p. 8221-8227.

37. Turchanin, A. and A. Golzhauser, *Carbon Nanomembranes.* Adv. Mat., 2016. **28**(29): p. 6075-6103.

38. Penner, P., et al., *Charge Transport through Carbon Nanomembranes.* J. Phys. Chem. C, 2014. **118**(37): p. 21687-21694.

39. Haag, R., et al., *Electrical breakdown of aliphatic and aromatic self-assembled monolayers used as nanometer-thick organic dielectrics.* J. Am. Chem. Soc., 1999. **121**(34): p. 7895-7906.

40. Holmlin, R.E., et al., *Electron transport through thin organic films in metal-insulator-metal junctions based on self-assembled monolayers.* J. Am. Chem. Soc., 2001. **123**(21): p. 5075-5085.

41. Grave, C., et al., *Charge Transport through Oligoarylene Self-assembled Monolayers: Interplay of Molecular Organization, Metal–Molecule Interactions, and Electronic Structure.* Adv. Funct. Mater., 2007. **17**(18): p. 3816-3828.

42. Querebillo, C.J., et al., *Static Conductance of Nitrile-Substituted Oligophenylene and Oligo(phenylene ethynylene) Self-Assembled Mono layers Studied by the Mercury-Drop Method.* J. Phys. Chem. C, 2013. **117**(48): p. 25556-25561.

43. Fracasso, D., et al., *Influence of an Atom in EGaIn/Ga2O3 Tunneling Junctions Comprising Self-Assembled Monolayers.* J. Phys. Chem. C, 2013. **117**(21): p. 11367-11376.

44. Beebe, J.M., et al., *Transition from direct tunneling to field emission in metal-molecule-metal junctions.* Phys. Rev. Lett., 2006. **97**(2): p. 026801.

45. Beebe, J.M., et al., *Measuring relative barrier heights in molecular electronic junctions with transition voltage spectroscopy.* ACS Nano, 2008. **2**(5): p. 827-832.

46. Kim, B., et al., *Correlation between HOMO alignment and contact resistance in molecular junctions: Aromatic thiols versus aromatic isocyanides.* J. Am. Chem. Soc., 2006. **128**(15): p. 4970-4971.

47. Bergren, A.J., et al., *Electronic Characteristics and Charge Transport Mechanisms for Large Area Aromatic Molecular Junctions.* J. Phys. Chem. C, 2010. **114**(37): p. 15806-15815.

48. Weiss, E.A., et al., *Influence of defects on the electrical characteristics of mercury-drop junctions: Self-assembled monolayers of n-alkanethiolates on rough and smooth silver.* J. Am. Chem. Soc., 2007. **129**(14): p. 4336-4349.

49. Thuo, M.M., et al., *Odd-even effects in charge transport across self-assembled monolayers.* J. Am. Chem. Soc., 2011. **133**(9): p. 2962-2975.

50. Yoon, H.J., et al., *The rate of charge tunneling is insensitive to polar terminal groups in self-assembled monolayers in Ag(TS)S(CH2)(n)M(CH2)(m)T//Ga2O3/EGaIn junctions.* J. Am. Chem. Soc., 2014. **136**(1): p. 16-19.

51. Tomfohr, J.K. and O.F. Sankey, *Complex band structure, decay lengths, and Fermi level alignment in simple molecular electronic systems.* Phys. Rev. B, 2002. **65**(24): p. 245105.

52. Rampi, M.A. and G.M. Whitesides, *A versatile experimental approach for understanding electron transport through organic materials.* Chem. Phys., 2002. **281**(2-3): p. 373-391.

53. Tivanski, A.V., et al., *Conjugated thiol linker for enhanced electrical conduction of gold-molecule contacts.* J. Phys. Chem. B, 2005. **109**(12): p. 5398-5402.

54. Wold, D.J., et al., *Distance dependence of electron tunneling through self-assembled monolayers measured by conducting probe atomic force microscopy: Unsaturated versus saturated molecular junctions.* J. Phys. Chem. B, 2002. **106**(11): p. 2813-2816.

55. Holmlin, R.E., et al., *Correlating electron transport and molecular structure in organic thin films.* Angew. Chem. Int. Ed., 2001. **40**(12): p. 2316-2320.

56. Kim, B., et al., *Molecular Tunnel Junctions Based on pi-Conjugated Oligoacene Thiols and Dithiols between Ag, Au, and Pt Contacts: Effect of Surface Linking Group and Metal Work Function.* J. Am. Chem. Soc., 2011. **133**(49): p. 19864-19877.

57. Campbell, I.H., et al., *Controlling Schottky energy barriers in organic electronic devices using self-assembled monolayers.* Phys. Rev. B, 1996. **54**(20): p. 14321-14324.

58. de Boer, B., et al., *Tuning of metal work functions with self-assembled monolayers.* Adv. Mat., 2005. **17**(5): p. 621-625.

59. Evans, S.D. and A. Ulman, *Surface-Potential Studies of Alkyl-Thiol Monolayers Adsorbed on Gold.* Chem. Phys. Lett., 1990. **170**(5-6): p. 462-466.

60. Rusu, P.C. and G. Brocks, *Surface dipoles and work functions of alkylthiolates and fluorinated alkylthiolates on Au(111).* J. Phys. Chem. B, 2006. **110**(45): p. 22628-22634.

61. Rusu, P.C. and G. Brocks, *Work functions of self-assembled monolayers on metal surfaces by first-principles calculations.* Phys. Rev. B, 2006. **74**(7).

62. Fenter, P., A. Eberhardt, and P. Eisenberger, *Self-Assembly of N-Alkyl Thiols as Disulfides on Au(111).* Science, 1994. **266**(5188): p. 1216-1218.

63. Poirier, G.E. and M.J. Tarlov, *The C(4x2) Superlattice of N-Alkanethiol Monolayers Self-Assembled an Au(111).* Langmuir, 1994. **10**(9): p. 2853-2856.

64. Fenter, P., P. Eisenberger, and K.S. Liang, *Chain-Length Dependence of the Structures and Phases of Ch3(Ch2)N-1sh Self-Assembled on Au(111).* Phys. Rev. Lett., 1993. **70**(16): p. 2447-2450.

65. Hahner, G., et al., *Structure of Self-Organizing Organic Films - a near Edge X-Ray Absorption Fine-Structure Investigation of Thiol Layers Adsorbed on Gold.* J. Vac. Sci. Technol. A, 1992. **10**(4): p. 2758-2763.

66. Hahner, G., et al., *Investigation of Intermediate Steps in the Self-Assembly of N-Alkanethiols on Gold Surfaces by Soft-X-Ray Spectroscopy.* Langmuir, 1993. **9**(8): p. 1955-1958.

67. Schlenoff, J.B., M. Li, and H. Ly, *Stability and Self-Exchange in Alkanethiol Monolayers.* J. Am. Chem. Soc., 1995. **117**(50): p. 12528-12536.

68. Muller, H.U., et al., *Low-energy electron-induced damage in hexadecanethiolate monolayers.* J. Phys. Chem. B, 1998. **102**(41): p. 7949-7959.

69. Ballav, N., C.-H. Chen, and M. Zharnikov, *Electron Beam and Soft X-ray Lithography with a Monomolecular Resist.* J. Photopolym. Sci. Tec., 2008. **21**(4): p. 511-517.

70. Chesneau, F., et al., *Modification of Self-Assembled Mono layers of Perfluoroterphenyl-Substituted Alkanethiols by Low-Energy Electrons.* J. Phys. Chem. C, 2011. **115**(11): p. 4773-4782.

71. Waske, P.A., et al., *Self-Assembled Mono layers of Cyclic Aliphatic Thiols and Their Reaction toward Electron Irradiation.* J. Phys. Chem. C, 2012. **116**(25): p. 13559-13568.

72. Beyer, A., et al., *Fully cross-linked and chemically patterned self-assembled monolayers.* Phys. Chem. Chem. Phys., 2008. **10**(48): p. 7233-7238.

73. Hofmann, S., *Auger- and X-ray photoelectron spectroscopy in materials science: a user-oriented guide*. Springer series in surface sciences,. 2013, Heidelberg ; New York: Springer. xix, 528 pages.

74. van der Heide, P., *X-ray Photoelectron Spectroscopy: An introduction to Principles and Practices*. 2011: Wiley.

75. Ratner, B.D. and D.G. Castner, *Electron Spectroscopy for Chemical Analysis*, in *Surface Analysis – The Principal Techniques*. 2009, John Wiley & Sons, Ltd. p. 47-112.

76. Lamont, C.L.A. and J. Wilkes, *Attenuation length of electrons in self-assembled monolayers of n-alkanethiols on gold.* Langmuir, 1999. **15**(6): p. 2037-2042.

77. Bain, C.D. and G.M. Whitesides, *Attenuation Lengths of Photoelectrons in Hydrocarbon Films.* J. Phys. Chem., 1989. **93**(4): p. 1670-1673.

78. Meyer, E., *Atomic Force Microscopy.* Prog. Surf. Sci. Surface Science, 1992. **41**(1): p. 3-49.

79. Eaton, P. and P. West, *Atomic Force Microscopy*. 2010: OUP Oxford. 248.

80. West, P.E., *Introduction to Atomic Force Microscopy: Theory, Practice, Applications*. 2006, 159 pages.

81. Howland, R.S. and M.D. Kirk, *2.3 - STM and SFM: Scanning Tunneling Microscopy and Scanning Force Microscopy*, in *Encyclopedia of Materials Characterization*. 1992, Butterworth-Heinemann: Boston. p. 85-98.

82. Zhou, W. and Z.L. Wang, *Scanning microscopy for nanotechnology: techniques and applications*. 2007, New York: Springer. xiv, 522 p., 12 p. of plates.

83. Bindell, J.B., *2.2 - SEM: Scanning Electron Microscopy*, in *Encyclopedia of Materials Characterization*. 1992, Butterworth-Heinemann: Boston. p. 70-84.

84. Kuo, W.C.H., M. Briceno, and D. Ozkaya, *Characterisation of Catalysts Using Secondary and Backscattered Electron In-lens Detectors.* Platin. Met. Rev., 2014. **58**(2): p. 106-110.

85. Rai-Choudhury, P., *Handbook of microlithography, micromachining, and microfabrication*; SPIE Optical Engineering Press: London, UK, 1997, 768 pages.

86. Mohammad, M.A., et al., *Fundamentals of Electron Beam Exposure and Development*, in *Nanofabrication: Techniques and Principles*, M. Stepanova and S. Dew, Editors. 2012, Springer Vienna: Vienna. p. 11-41.

87. Choi, S.H., et al., *Transition from Tunneling to Hopping Transport in Long, Conjugated Oligo-imine Wires Connected to Metals.* J. Am. Chem. Soc., 2010. **132**(12): p. 4358-4368.

88. Akkerman, H.B., et al., *Towards molecular electronics with large-area molecular junctions.* Nature, 2006. **441**(7089): p. 69-72.

89. Kilgour, M. and D. Segal, *Charge transport in molecular junctions: From tunneling to hopping with the probe technique.* J Chem Phys, 2015. **143**(2): p. 024111.

90. Nijhuis, C.A., et al., *Charge transport and rectification in arrays of SAM-based tunneling junctions.* Nano Lett., 2010. **10**(9): p. 3611-3619.

91. Wang, W.Y., T. Lee, and M.A. Reed, *Mechanism of electron conduction in self-assembled alkanethiol monolayer devices.* Phys. Rev. B, 2003. **68**(3).

92. Mirjani, F., J.M. Thijssen, and S.J. van der Molen, *Advantages and limitations of transition voltage spectroscopy: A theoretical analysis.* Phys. Rev. B, 2011. **84**(11).

93. Tan, A.R., et al., *Length dependence of frontier orbital alignment in aromatic molecular junctions.* Appl. Phys. Lett., 2012. **101**(24).

94. Palermo, V., M. Palma, and P. Samori, *Electronic characterization of organic thin films by Kelvin probe force microscopy.* Adv. Mat., 2006. **18**(2): p. 145-164.

95. Halas, S. and T. Durakiewicz, *Is work function a surface or a bulk property?* Vacuum, 2010. **85**(4): p. 486-488.

96. Schlaf, R. *Tutorial on Kelvin Probe Measurements*. [cited 2016; Available from: http://rsl.eng.usf.edu/Documents/Tutorials/TutorialsKelvinProbe.pdf.

97. Schlaf, R. *Tutorial on Work Function*. [cited 2016; Available from: http://rsl.eng.usf.edu/Documents/Tutorials/TutorialsWorkFunction.pdf.

98. Michaelson, H.B., *The work function of the elements and its periodicity.* J. Appl. Phys., 1977. **48**(11): p. 4729-4733.

99. Ziegler, D., et al., *Variations in the work function of doped single- and few-layer graphene assessed by Kelvin probe force microscopy and density functional theory.* Phys. Rev. B, 2011. **83**(23).

100. Abu-Husein, T., et al., *The Effects of Embedded Dipoles in Aromatic Self-Assembled Monolayers.* Adv. Funct. Mater., 2015. **25**(25): p. 3943-3957.

101. Schuster, S., *Work Function Tuning at Interfaces by Monomolecular Films*, in *Combined Faculty of Natural Sciences and Mathematics*. 2015, Ruprecht Karls University: Heidelberg, Germany.

102. Scharf, J., et al., *Electrochemical and surface analytical studies of self-assembled monolayers of three aromatic thiols on gold electrodes.* J. Solid State Electrochem., 2001. **5**(6): p. 396-401.

103. Liu, K., X.H. Wang, and F.S. Wang, *Probing Charge Transport of Ruthenium-Complex-Based Molecular Wires at the Single-Molecule Level.* ACS Nano, 2008. **2**(11): p. 2315-2323.

104. Chesneau, F., et al., *Adsorption of Long-Chain Alkanethiols on Au(111): A Look from the Substrate by High Resolution X-ray Photoelectron Spectroscopy.* J. Phys. Chem. C, 2010. **114**(15): p. 7112-7119.

105. Moulder, J.F. and J. Chastain, *Handbook of X-ray Photoelectron Spectroscopy: A Reference Book of Standard Spectra for Identification and Interpretation of XPS Data*. 1992: Physical Electronics Division, Perkin-Elmer Corporation.

106. Thome, J., et al., *Increased lateral density in alkanethiolate films on gold by mercury adsorption.* Langmuir, 1998. **14**(26): p. 7435-7449.

107. Walczak, M.M., et al., *Structure and Interfacial Properties of Spontaneously Adsorbed Normal-Alkanethiolate Monolayers on Evaporated Silver Surfaces.* J. Am. Chem. Soc., 1991. **113**(7): p. 2370-2378.

108. Kondoh, H., et al., *Adsorption of thiolates to singly coordinated sites on Au(111) evidenced by photoelectron diffraction.* Phys. Rev. Lett, 2003. **90**(6).

109. Burdinski, D. and M.H. Blees, *Thiosulfate- and thiosulfonate-based etchants for the patterning of gold using microcontact printing.* Chem. Mater., 2007. **19**(16): p. 3933-3944.

110. Xia, Y.N., et al., *A selective etching solution for use with patterned self-assembled monolayers of alkanethiolates on gold.* Chem. Mater., 1995. **7**(12): p. 2332-2337.

111. von Wrochem, F., et al., *Efficient electronic coupling and improved stability with dithiocarbamate-based molecular junctions.* Nat. Nanotechnol., 2010. **5**(8): p. 618-24.

112. Gao, D., et al., *Fabrication of asymmetric molecular junctions by the oriented assembly of dithiocarbamate rectifiers.* J. Am. Chem. Soc., 2011. **133**(15): p. 5921-30.

113. Zharnikov, M., *High-resolution X-ray photoelectron spectroscopy in studies of self-assembled organic monolayers.* J. Electron Spectrosc. Relat. Phenom., 2010. **178**: p. 380-393.

114. Shaporenko, A., et al., *A detailed analysis of the photoemission spectra of basic thioaromatic monolayers on noble metal substrates.* J. Electron Spectrosc. Relat. Phenom., 2006. **151**(1): p. 45-51.

115. Chesneau, F., *Fabrication of Metal-Insulator-Metal Junctions for Spintronic Devices Using Self-Assembled-Monolayers*, in *Combined Faculty of Natural Sciences and Mathematics*. 2011, Ruprecht Karls University: Heidelberg, Germany.

116. Lukasczyk, T., et al., *Electron-beam-induced deposition in ultrahigh vacuum: Lithographic fabrication of clean iron nanostructures.* Small, 2008. **4**(6): p. 841-846.

117. Walz, M.M., et al., *Electrons as "Invisible Ink": Fabrication of Nanostructures by Local Electron Beam Induced Activation of SiOx.* Angew. Chem. Int. Ed., 2010. **49**(27): p. 4669-4673.

118. Cyganik, P., et al., *Modification and stability of aromatic self-assembled monolayers upon irradiation with energetic particles.* J. Phys. Chem. B, 2005. **109**(11): p. 5085-5094.

119. Ballav, N., et al., *Biphenylnitrile-Based Self-Assembled Monolayers on Au(111): Spectroscopic Characterization and Resonant Excitation of the Nitrile Tail Group.* J. Phys. Chem. C, 2010. **114**(29): p. 12719-12727.

120. Weidner, T., et al., *Modification of biphenylselenolate monolayers by low-energy electrons.* Phys. Status Solidi B, 2009. **246**(7): p. 1519-1528.

121. Feulner, P., et al., *Strong temperature dependence of irradiation effects in organic layers.* Phys. Rev. Lett., 2004. **93**(17): p. 178302.

122. Gölzhäuser, A., et al., *Nanoscale patterning of self-assembled monolayers with electrons.* J. Vac. Sci. Technol. B, 2000. **18**(6): p. 3414-3418.

123. Völkel, B., et al., *Influence of secondary electrons in proximal probe lithography.* J. Vac. Sci. Technol. B, 1997. **15**(6): p. 2877-2881.

124. Briggs, D. and M.P. Seah, *Practical Surface Analysis, Auger and X-ray Photoelectron Spectroscopy*. 1990: Wiley, 674 pages.

125. Lin, Y.H. and D.C. Joy, *A new examination of secondary electron yield data.* Surf. Interface Anal., 2005. **37**(11): p. 895-900.

126. Chiechi, R.C., et al., *Eutectic gallium-indium (EGaIn): A moldable liquid metal for electrical characterization of self-assembled monolayers.* Angew. Chem. Int. Ed., 2008. **47**(1): p. 142-144.

127. Fracasso, D., *Charge Transport through Self-Assembled Monolayers with Eutectic Gallium-Indium Top Contacts*, in *Faculty of Mathematics and Natural Sciences*. 2014, University of Groningen. Netherlands.

128. Feng, D.Q., et al., *Electronic structure and polymerization of a self-assembled monolayer with multiple arene rings.* Phys. Rev. B, 2006. **74**(16): p. 165425.

129. Feng, D.Q., et al., *Engineering of the electronic structure in an aromatic dithiol monomolecular organic insulator.* J. Mater. Chem., 2006. **16**(44): p. 4343-4347.

130. Simmons, J.G., *Generalized Formula for Electric Tunnel Effect between Similar Electrodes Separated by a Thin Insulating Film.* J. Appl. Phys., 1963. **34**(6): p. 1793-1803.

131. Bao, W.S., et al., *Tunneling resistance and its effect on the electrical conductivity of carbon nanotube nanocomposites.* J. Appl. Phys., 2012. **111**(9): p. 093726.

132. Champness, C.H. and A. Chan, *Relation between barrier height and work function in contacts to selenium.* J. Appl. Phys., 1985. **57**(10): p. 4823-4825.

133. Taşçıoğlu, İ., et al., *The effect of metal work function on the barrier height of metal/CdS/SnO2/In–Ga structures.* Curr. Appl. Phys., 2013. **13**(7): p. 1306-1310.

134. Cowley, A.M. and S.M. Sze, *Surface States and Barrier Height of Metal-Semiconductor Systems.* J. Appl. Phys., 1965. **36**(10): p. 3212-3220.

135. Huisman, E.H., et al., *Interpretation of Transition Voltage Spectroscopy.* Nano Lett., 2009. **9**(11): p. 3909-3913.

136. Engelkes, V.B., J.M. Beebe, and C.D. Frisbie, *Length-Dependent Transport in Molecular Junctions Based on SAMs of Alkanethiols and Alkanedithiols: Effect of Metal Work Function and Applied Bias on Tunneling Efficiency and Contact Resistance.* J. Am. Chem. Soc., 2004. **126**(43): p. 14287-14296.

137. de Boer, B., et al. *Tuning of metal work functions with self-assembled monolayers*. 2004. Proc. SPIE

138. Azzam, W., et al., *Combined STM and FTIR Characterization of Terphenylalkanethiol Monolayers on Au(111): Effect of Alkyl Chain Length and Deposition Temperature.* Langmuir, 2006. **22**(8): p. 3647-3655.

139. Chesneau, F., et al., *Self-assembled monolayers of perfluoroterphenyl-substituted alkanethiols: specific characteristics and odd-even effects.* Phys. Chem. Chem. Phys., 2010. **12**(38): p. 12123-12137.

140. Cyganik, P., et al., *Competition as a Design Concept: Polymorphism in Self-Assembled Monolayers of Biphenyl-Based Thiols.* J. Am. Chem. Soc., 2006. **128**(42): p. 13868-13878.

141. Cyganik, P., et al., *Influence of Molecular Structure on Phase Transitions: A Study of Self-Assembled Monolayers of 2-(Aryl)-ethane Thiols.* J. Phys. Chem. C, 2007. **111**(45): p. 16909-16919.

142. Dauselt, J., et al., *Compensation of the Odd−Even Effects in Araliphatic Self-Assembled Monolayers by Nonsymmetric Attachment of the Aromatic Part.* J. Phys. Chem. C, 2011. **115**(6): p. 2841-2854.

143. Rong, H.-T., et al., *On the Importance of the Headgroup Substrate Bond in Thiol Monolayers: A Study of Biphenyl-Based Thiols on Gold and Silver.* Langmuir, 2001. **17**(5): p. 1582-1593.

144. Shaporenko, A., et al., *Structural Forces in Self-Assembled Monolayers: Terphenyl-Substituted Alkanethiols on Noble Metal Substrates.* J. Phys. Chem. B, 2004. **108**(38): p. 14462-14469.

145. Zharnikov, M., et al., *The effect of sulfur-metal bonding on the structure of self-assembled monolayers.* Phys. Chem. Chem. Phys., 2000. **2**(15): p. 3359-3362.

146. Zharnikov, M. and M. Grunze, *Spectroscopic characterization of thiol-derived self-assembling monolayers.* J. Phys.: Condens. Matter., 2001. **13**(49): p. 11333-11365.

147. Silien, C., et al., *Self-Assembly of a Pyridine-Terminated Thiol Monolayer on Au(111).* Langmuir, 2009. **25**(2): p. 959-967.